

One-Dimensional Electron Liquid at a Surface: Gold Nanowires on Ge(001)

Dissertation zur Erlangung des
naturwissenschaftlichen Doktorgrades der
Julius-Maximilians-Universität Würzburg

vorgelegt von
Christian Blumenstein
geboren in Bad Wildungen

Würzburg 2012

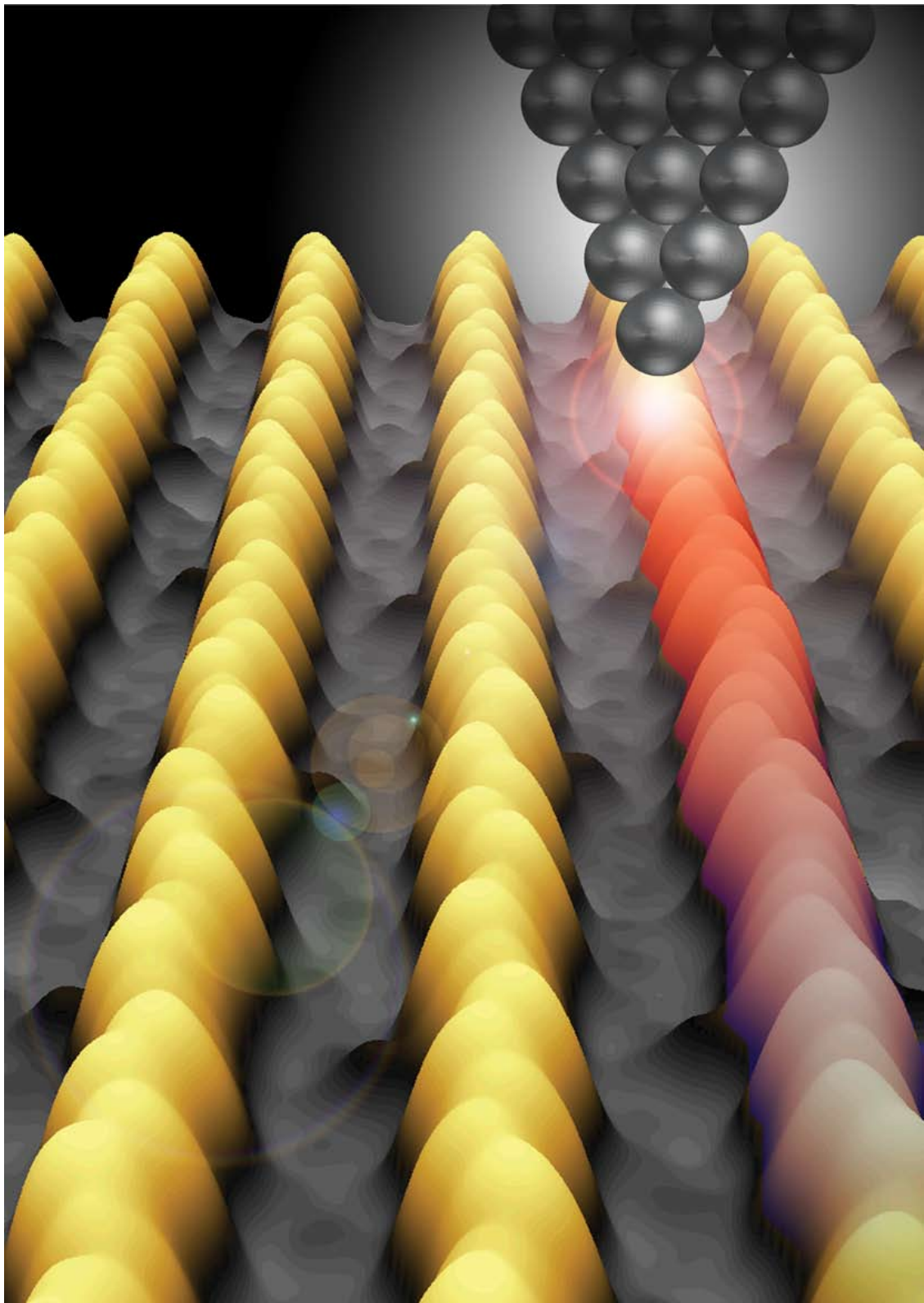


Figure 0.1: Probing the structural and electronic properties of self-organized Au chains on Ge(001) with atomic precision, using scanning tunneling microscopy.

Eingereicht am:

bei der Fakultät für Physik und Astronomie

Gutachter der Dissertation:

1. Gutachter & Betreuer: Priv.-Doz. Dr. Jörg Schäfer
2. Gutachter: Prof. Dr. René Matzdorf
3. Gutachter: Prof. Dr. Wolf Dieter Schneider

Prüfer im Promotionskolloquium:

1. Prüfer: Priv.-Doz. Dr. Jörg Schäfer
2. Prüfer: Prof. Dr. René Matzdorf
3. Prüfer: Prof. Dr. Wolf-Dieter Schneider
4. Prüfer: Prof. Dr. Giorgio Sangiovanni

Tag des Promotionskolloquiums: 11.09.2012

Doktorurkunde ausgehändigt am:

Dedicated in loving memory to Maria Blumenstein.
1937 – 2011

Real Artists Ship.

— Steve Jobs

Abstract

Self-organized nanowires at semiconductor surfaces offer the unique opportunity to study electrons in reduced dimensions. Notably the dimensionality of the system determines its electronic properties, beyond the quasiparticle description. In the quasi-one-dimensional (1D) regime with weak lateral coupling between the chains, a Peierls instability can be realized. A nesting condition in the Fermi surface leads to a back-folding of the 1D electron band and thus to an insulating state. It is accompanied by a charge density wave (CDW) in real space that corresponds to the nesting vector. This effect has been claimed to occur in many surface-defined nanowire systems, such as the In chains on Si(111) or the Au reconstructions on the terraced Si(553) and Si(557) surfaces. Therefore a weak coupling between the nanowires in these systems has to be concluded. However theory proposes another state in the perfect 1D limit, which is completely destroyed upon slight coupling to higher dimensions. In this so-called Tomonaga-Luttinger liquid (TLL) state, the quasiparticle description of the Fermi liquid breaks down. Since the interaction between the electrons is enhanced due to the strong confinement, only collective excitations are allowed. This leads to novel effects like spin charge separation, where spin and charge degrees of freedom are decoupled and allowed to travel independently along the 1D-chain. Such rare state has not been realized at a surface until today.

This thesis uses a novel approach to realize nanowires with improved confinement by studying the Au reconstructed Ge(001) surface. A new cleaning procedure using piranha solution is presented, in order to prepare a clean and long-range ordered substrate. To ensure optimal growth of the Au nanowires the phase diagram is extensively studied by scanning tunneling microscopy (STM) and low energy electron diffraction (LEED). The structural elements of the chains are revealed and described in high detail. Remarkably a structural phase transition of the delicate wire structure is found to occur above room temperature. Due to the lack of energy gaps a Peierls transition can be excluded as its origin. The transition is rather determined as 3D Ising type and therefore includes the substrate as well.

Two hallmark properties of a TLL are found in the Au/Ge(001) wires by spectroscopic studies: Power-law suppression of the density of states (DOS) and universal scaling. This impressively proves the existence of a TLL in these chains and opens up a gateway to an *atomic playground*. Local studies and manipulations of a TLL state become possible for the first time. These comprise (i) doping by alkaline atoms, (ii) studies on chain ends and (iii) tunable coupling between the chains by additional Au atoms. Most importantly these manipulations offer input and test for theoretical models and predictions, and are thereby ultimately advancing the field of correlated electrons.

Zusammenfassung

Selbstorganisierte Nanodrähte auf Halbleiteroberflächen ermöglichen die Untersuchung von Elektronen in niedrigen Dimensionen. Interessanterweise werden die elektronischen Eigenschaften des Systems von dessen Dimensionalität bestimmt, und das noch über das Quasiteilchenbild hinaus. Das quasi-eindimensionale (1D) Regime zeichnet sich durch eine schwache laterale Kopplung zwischen den Ketten aus und ermöglicht die Ausbildung einer Peierls Instabilität. Durch eine Nesting Bedingung in der Fermi Fläche kommt es zu einer Bandrückfaltung und damit zu einem isolierenden Grundzustand. Dies wird begleitet von einer neuen Überstruktur im Realraum, die mit dem Nestingvektor korrespondiert. In früheren Nanodrahtsystemen wurde ein solcher Effekt gezeigt. Dazu gehören Indium Ketten auf Si(111) und die Gold rekonstruierten Substrate Si(553) und Si(557). Die Theorie sagt jedoch einen weiteren Zustand voraus, der nur im perfekten 1D Grenzfall existiert und der bei geringster Kopplung mit höheren Dimensionen zerstört wird. Dieser Zustand wird Tomonaga-Luttinger Flüssigkeit (TLL) genannt und führt zu einem Zusammenbruch des Quasiteilchenbildes der Fermi-Flüssigkeit. Hier sind nur noch kollektive Anregungen der Elektronen erlaubt, da die starke laterale Einschränkung zu einer erhöhten Kopplung zwischen den Teilchen führt. Dadurch treten interessante Effekte wie Spin-Ladungs-Trennung auf, bei dem sich die Ladung und der Spin eines Elektrons entkoppeln und getrennt voneinander durch den Nanodraht bewegen können. Bis heute wurde solch ein seltener Zustand noch nicht an einer Oberfläche beobachtet.

In dieser Arbeit wird ein neuer Ansatz zur Herstellung von besser definierten 1D Ketten gewählt. Dazu wird die Au-rekonstruierte Ge(001) Nanodraht-Oberfläche untersucht. Für die Präparation des Substrates wird ein neues Rezept entwickelt, welches eine langreichweitig geordnete Oberfläche erzeugt. Um das Wachstum der Nanodrähte zu optimieren wird das Wachstums-Phasendiagramm ausgiebig untersucht. Außerdem werden die strukturellen Bausteine der Ketten sehr genau beschrieben. Es ist bemerkenswert, dass ein struktureller Phasenübergang der Ketten oberhalb von Raumtemperatur gefunden wird. Aufgrund von spektroskopischen Untersuchungen kann eine Peierls Instabilität als Ursache ausgeschlossen werden. Es handelt sich um einen 3D-Ising-Typ Übergang an dem das Substrat ebenfalls beteiligt ist. Die Untersuchungen zur elektronischen Struktur der Ketten zeigen zwei deutliche Erkennungsmerkmale einer TLL: Ein potenzgesetzartiger Verlauf der Zustandsdichte und universales Skalenverhalten. Daher wird zum ersten Mal eine TLL an einer Oberfläche nachgewiesen, was nun gezielt lokale Untersuchungen und Manipulationen ermöglicht. Dazu gehören (i) Dotierung mit Alkalimetallen, (ii) die Untersuchung von Kettenenden und (iii) die einstellbare Kopplung zwischen den Ketten durch zusätzliche Goldatome. Damit wird ein wichtiger Beitrag zu theoretischen Vorhersagen und Modellen geliefert und somit das Verständnis korrelierter Elektronen vorangetrieben.

Contents

1	Introduction	3
2	Theoretical concepts of 1D physics	7
2.1	Peierls instability	8
2.1.1	Lindhard response function	9
2.1.2	Electron-phonon interaction	10
2.1.3	Limitations of the Peierls picture	14
2.2	Tomonaga-Luttinger liquid	15
2.2.1	Excitations in one dimension	15
2.2.2	Tomonaga-Luttinger model and bosonization	17
2.2.3	Interaction scenarios and g-ology	21
2.2.4	Spectral function	26
2.2.5	Tomonaga-Luttinger model with boundary	27
2.2.6	Summary	30
2.2.7	Limitations of the Tomonaga-Luttinger model	30
3	Experimental methods for surface analysis	33
3.1	Tunneling microscopy	33
3.1.1	Basic principle	33
3.1.2	Tunneling current	36
3.2	Tunneling spectroscopy	40
3.2.1	$I(V)$ spectra and extraction of the density of states	42
3.2.2	Lock-In spectroscopy	43
3.3	Low energy electron diffraction	44
3.3.1	Surface sensitivity	45
3.3.2	Geometric theory	47
3.3.3	Kinematic theory	49
3.3.4	Debye-Waller factor	51
3.4	Experimental setup	53
4	Choosing the substrate	57
4.1	Previous studies on nanowires at surfaces	57
4.1.1	In chains on Si(111)	57
4.1.2	Au chains on Si(557)	60
4.1.3	Au chains on Si(553)	62
4.2	The Ge(001) surface	65
4.3	Preparation of clean Ge(001) surfaces	66

4.3.1	Piranha etching and thermal passivation	67
4.3.2	Degassing and oxide removal	68
4.3.3	Protective oxide quality	69
4.3.4	Surface quality after oxide removal	71
4.3.5	Comparison with alternate cleaning procedures	74
5	Structural elements of Au/Ge(001) nanowires	77
5.1	Current knowledge about nanowires on Ge(001)	77
5.2	Growth regimes and phase diagram of Au/Ge(001)	80
5.3	Chain architecture description	86
5.3.1	Structural elements	86
5.3.2	Long-range order	87
5.3.3	Bias series	88
5.3.4	Lateral confinement	94
5.4	Dynamics	95
5.5	Fourier transformation	97
5.6	Construction of the diffraction pattern	99
5.7	Phase transition	100
5.7.1	Transition observed in real space	100
5.7.2	Transition observed in reciprocal space	102
5.7.3	Origin of the transition	106
5.8	Structural model from first principles	109
6	Electronic properties of Au/Ge(001) nanowires	113
6.1	Electronic band structure from ARPES	113
6.2	Density of states maps	116
6.3	Tomonaga-Luttinger liquid behavior	120
6.3.1	Power-law suppression of the density of states	120
6.3.2	Universal scaling	123
6.4	Spin-charge separation	125
6.5	Related Tomonga-Luttinger liquid systems	126
6.6	Zero-bias anomalies	129
6.6.1	Charging of islands	130
6.6.2	Dynamical Coulomb blockade	132
6.6.3	Variable range hopping	134
6.7	Atomic-scale manipulation	134
6.7.1	Chain ends	136
6.7.2	Crossover region	139
6.7.3	Doping a Tomonga-Luttinger liquid	140
7	Summary and Outlook	145
	Bibliography	151
	List of own publications	151
	General Literature	154

Acknowledgment	167
Curriculum vitae	171
Erklärung	173

List of figures

0.1	Probing the structural and electronic properties of self-organized Au chains on Ge(001) with atomic precision, using scanning tunneling microscopy.	3
1.1	Schematic phase diagram for Fermi and Luttinger liquid depending on the dimensionality of the system.	4
2.1	Schematic mechanism of the Peierls instability	8
2.2	Mean-field description of the energy gap of the Peierls ground state.	9
2.3	Fermi surfaces and nesting conditions for different dimensions	11
2.4	Phonon frequency renormalization due to electron phonon interaction	13
2.5	Dispersion and excitation spectrum of a 1D electron gas	16
2.6	Linearized dispersion of the 1D electron gas and corresponding excitation spectrum.	17
2.7	Scattering processes in 1D (g-ology)	22
2.8	Theoretical prediction for a Tomonaga-Luttinger liquid spectrum at chain end.	29
3.1	The tunneling effect in a nutshell.	34
3.2	Schematic representation of the image acquisition using STM.	34
3.3	Tersoff and Hamann simplified model for the STM tip.	37
3.4	Tunneling scenario for high bias and tunneling probability for both polarities.	41
3.5	Schematic of a typical low energy electron diffraction optics setup	45
3.6	Universal curve for the electron mean free path in solids depending on their kinetic energy.	46
3.7	Geometrical scattering from a surface	48
3.8	Ewald construction for low energy electron diffraction	49
3.9	Electron scattering schematic for the kinematic theory of diffraction	50
3.10	Experimental setup of the Omicron low-temperature STM	54
4.1	Review of the In/Si(111) surface findings	59
4.2	Review of the Au/Si(557) surface findings	61
4.3	Review of the Au/Si(553) surface findings	63
4.4	Ge(001) dimer binging situation.	66
4.5	Reconstructions of the Ge(001) surface.	67
4.6	XPS investigations on the artificial and native oxide quality of Ge(001)	70
4.7	AFM and XPS studies on the cleanliness of the etching procedure	72
4.8	Long-range and local order of the prepared Ge(001) surface.	73

5.1	Pt nanowires on Ge(001)	78
5.2	Au/Ge(001) studies from Wang <i>et al.</i>	79
5.3	Phase diagram on the Au/Ge(001) system including temperature and Au coverage	80
5.4	Low-Au coverage regime scanning tunneling microscopy image.	81
5.5	High coverage regime with Au cluster visible in scanning tunneling microscopy.	83
5.6	scanning tunneling microscopy image of cluster top with metallic spectra at 4.7 K	84
5.7	Dual domain scanning tunneling microscopy image of the surface at optimum Au coverage	85
5.8	Superstructure comparison for both polarities in scanning tunneling microscopy.	86
5.9	Profile analysis of the superstructure.	87
5.10	Long-range order of the superstructure seen by scanning tunneling microscopy.	88
5.11	High energy bias series of the identical sample surface.	90
5.12	Low energy bias series of the identical sample surface.	91
5.13	Schematic band situation in the Au/Ge(001) nanowires.	93
5.14	Lateral profile comparison of the nanowire width.	94
5.15	Analysis of the VW zig-zag with lateral line profiles.	95
5.16	Noisy areas during scanning tunneling microscopy point at dynamics in the chains	96
5.17	Schematic of the basic unit cell superimposed with the superstructure.	97
5.18	FFT analysis of the long-range order.	98
5.19	LEED pattern with two substrate domains.	98
5.20	Explanation of the LEED pattern including the superstructure.	99
5.21	STM images of the nanowires above and below the phase transition for both polarities.	101
5.22	Autocorrelated STM images below and above T_C	102
5.23	Temperature series of LEED patterns across the phase transition.	103
5.24	Temperature calibration of the sample.	104
5.25	LEED intensity vs. temperature for the superstructure and basic unit cell reflexes.	105
5.26	DFT model for the basic Au/Ge(001) reconstruction	110
5.27	Comparison of simulated STM images by DFT with experimental tunneling images	111
6.1	ARPES mapping of the band structure of Au/Ge(001) chains.	114
6.2	Schematic of the band situation in the Au/Ge(001) chains.	115
6.3	Comparison of DOS and topography STM measurements for a variety of setpoints.	117
6.4	DOS at higher binding energies showing perpendicular filaments	119

6.5	Tunneling conductivity close to the Fermi energy, with power-law suppression and temperature dependent DOS at zero bias.	121
6.6	Angle-integrated line shape of 1D band from ARPES	122
6.7	Universal scaling plots of the temperature dependent DOS from STS. . .	124
6.8	Weight of spinon and holon in the spectral function depending on the correlation strength of the system.	126
6.9	Scanning tunneling spectroscopy on the purple bronze	128
6.10	Comparison of the DOS with Coulomb blockade model.	130
6.11	Schematic of the tunneling setup with charging of islands	131
6.12	Schematic representation of the dynamical Coulomb blockade	132
6.13	Schematic representation of atomic modification possibilities of the TLL chains.	135
6.14	Study of chain end spectra with corresponding modeling of the obtained signal.	137
6.15	Crossover Tomonaga-Luttinger liquid spectra near a chain end, comparing experiment and theory	140
6.16	K adsorption sites on the nanowires scrutinized with STM	142
6.17	Spectroscopy of a doped Au/Ge(001) surface.	143

List of acronyms

1D	one-dimensional
2D	two-dimensional
3D	three-dimensional
AC	analysis chamber
AD	Au-Au homodimer
AFM	atomic force microscopy
ARPES	angle resolved photoemission spectroscopy
CDW	charge density wave
DFT	density functional theory
DCB	dynamical Coulomb blockade
DOS	density of states
EDC	energy distribution curve
FFT	fast-Fourier transformation
FWHM	full-width (at) half maximum
GGA	generalized gradient approximation
HD	Au-Ge-heterodimer
IBA	ion bombardment and annealing
I(V)-LEED	intensity vs. voltage LEED
LDOS	local density of states
LEED	low energy electron diffraction
LHe	liquid helium

LN₂	liquid nitrogen
low-D	low-dimensional
LT	low-temperature
LT-STM	low-temperature STM
MIT	metal-insulator transition
ML	monolayer
PC	preparation chamber
PLD	periodic lattice distortion
RT	room temperature
SBZ	surface Brillouin zone
STM	scanning tunneling microscopy
STS	scanning tunneling spectroscopy
SXRD	surface X-ray diffraction
TL	Tomonaga-Luttinger
TLL	Tomonaga-Luttinger liquid
UHV	ultra-high vacuum
XPS	X-ray photoelectron spectroscopy
VRH	variable range hopping
WKB	Wenzel-Kramers-Brillouin-approximation
ZBA	zero-bias anomalies

1 Introduction

“In this age of Nanotechnology, where the promise is to shape the world atom by atom, leading to the next industrial revolution, surface physics should be at the very forefront. ” Ward Plummer [18]

Strongly correlated electron systems offer a unique insight in electronic interactions and resulting phenomena beyond the simple quasiparticle description. Yet, the fabrication of such experimental realizations was limited for a long time to anisotropic bulk crystals, with very little control over the growth parameters. Novel preparation techniques on the other hand may now produce films with atomic precision or harvest self-organization effects to achieve low-dimensional system growth. In using the tools of surface science analysis, local studies of strongly correlated systems come into reach. Even the tuning of the interactions in these new class of materials becomes possible.

The spatial confinement at surface reconstructions enhances the correlations between the particles, since screening becomes less effective. Expected phenomena comprise Mott-Hubbard insulators [19] or superconductivity [20]. Moreover due to symmetry breaking at the surface a Rashba effect may occur [21], leading to a spin-orbit splitting, when using heavy adsorbate atoms. For one-dimensional (1D) nanowires at surfaces the coupling t_{\perp} between the chains controls their electronic properties, refer to schematic phase diagram in fig. 1.1:

When reducing the dimensionality of a system at low temperatures a Peierls instability can be observed [22], see fig. 1.1. In this state a nesting condition in the Fermi surface drives a metal insulator transition, resulting in a charge density wave (CDW) along the chain. This state is stabilized by a periodic lattice distortion (PLD) due to electron-phonon coupling. However long-range order is only reached upon finite coupling between nanowires. Fluctuations will inhibit the ordered state

above $T = 0$ K. Consequently a Peierls ground state will only occur in the quasi-1D regime.

Reducing the dimensionality even further one may reach the strict-1D regime of the so called Tomonaga-Luttinger liquid (TLL) [23], see fig. 1.1. Due to the strong confinement of this state the electrons are not allowed to act independently. The quasiparticle picture of the Fermi liquid breaks down. Instead the low-energy excitations are better described by bosons and lead to a suppression of the density of states (DOS) towards the chemical potential. A remarkable effect, which may be observed in such state is the spin-charge separation. An electron injected in a TLL dissolves into two excitations, a spinon (carrying the spin) and a holon (carrying the charge), that may move independently along the nanowire. Such state is very fragile and is easily destroyed for slight coupling to higher dimensions. So far a TLL was observed only in very few systems such as 1D crystals [24–26], carbon nanotubes [27, 28] and gated GaAs channels [29, 30].

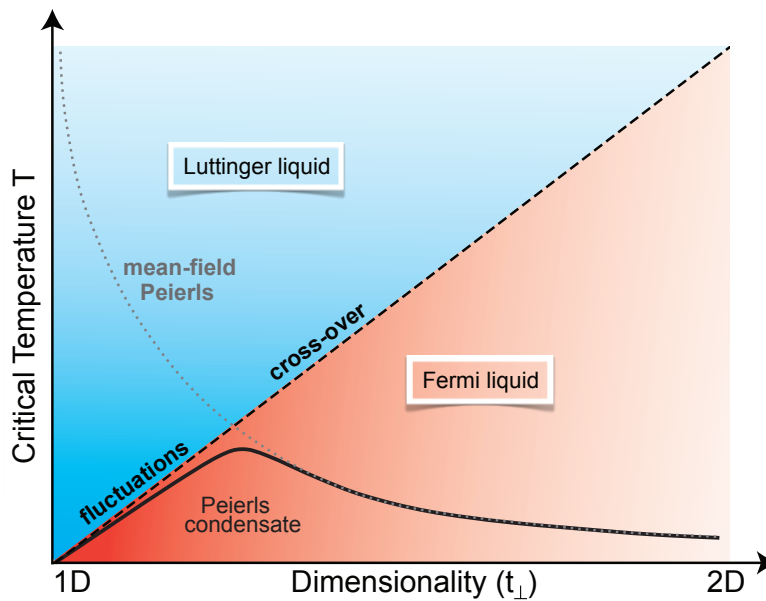


Figure 1.1: Schematic phase diagram for the relation of TLL and Fermi liquid, after [19]. Decreasing the dimensionality at low temperatures leads to a stabilization of the Peierls ground state. However this is only stable upon finite coupling between wires, i.e. in the quasi-1D regime. As such in the perfect 1D limit TLL behavior may be observed in a well confined system. This regime could not be reached with previous nanowires at surfaces.

In this context self-organized nanowires at surfaces offer the possibility to study atomic structure and the electronic properties using the spatial resolution power of scanning tunneling microscopy (STM). Furthermore the spectral function may be accessed via angle resolved photoemission spectroscopy (ARPES). Previous chains at surfaces were for example prepared by In atoms on Si(111) [31]. The four atom wide chains undergo a phase transition upon cooling and a CDW was observed in STM. A corresponding nesting condition could be identified using ARPES, thus rendering this system the paradigmatic example of a Peierls instability at a surface. Likewise the Au reconstructions on the stepped silicon surfaces of Si(557) [32] or Si(553) [33] showed indications for a Peierls transition with a CDW upon cooling and energy gaps in the band structure. Consequently these systems have to be identified as quasi-1D with a lateral coupling between the wires at the surface. Most importantly no indications for a TLL could be found in any surface defined nanowires system up to now.

However the realization of a TLL at a surface would be highly intriguing, since this would open the gateway towards an *atomic playground*. Local studies at chain ends, at defects or terrace edges may serve as a test for theoretical predictions on semi-infinite TLL models [34–36]. Doping and introduction of impurity atoms is easily performed at a surface. This could alter the band fillings or induce additional scattering sites in the chains. Additionally this holds the potential to lead to a crossover into the Fermi liquid regime and to a Peierls instability.

Hence the quest for better confined structures at surfaces was ongoing. This was the motivation for the present thesis. In turning to a different combination of metal adsorbants and substrate the choice fell on Au nanowires on the Ge(001) surface. This scarcely studied system [37, 38] turned out to be exceptionally well confined and having conduction electrons at the chemical potential. But challenges remained in the defect free preparation for long-range ordered chains as well as the detailed analysis of structure and electronic properties.

This thesis is organized as follows: Chapter 2 describes the relevant theoretical models of the Tomonaga Luttinger Liquid and the Peierls Instability, occurring in 1D systems. The experimental setup and background on the techniques used is presented in chapter 3. A comparison of previous nanowire systems and the novel approach using the Ge(001) surface along with its preparation are shown in chapter 4. Chapter 5 deals with the growth analysis of the self-organized Au/Ge(001) nanowires as well as the detailed structural analysis with STM and low energy electron diffraction (LEED). The study on the electronic properties, i.e. the density of states seen by scanning tunneling spectroscopy (STS), and analysis on the TLL behavior is described in chapter 6. The thesis closes with a summary and an outlook for future studies.

2 Theoretical concepts of 1D physics

“We used to think if we knew one, we knew two, because one and one are two. We are finding that we must learn a great deal more about ‘and’.” Sir Arthur Eddington [39]

Generally the reduction of the dimensionality of a problem leads to a simplification and an easier solution may be obtained. Yet, when examining a macroscopic number of strongly interacting electrons in a solid, the reduction of the dimension is no longer straight-forward. In three-dimensional (3D) Landau’s theory of the Fermi liquid has been very successful in describing the system [40]. The introduction of quasiparticles for the low-energy excitations allows to treat the quasiparticles as non-interacting.

However electrons in one dimension do not behave this way. In the non-interacting limit a Peierls instability may occur, creating an insulating ground state. Many surface defined nanowires systems have been claimed to exhibit such effect. These include the In chains on Si(111) and the Au chains on Si(553) and Si(557). Notably this state is only stable in the quasi-one-dimensional (1D) case with slight coupling between neighboring nanowires.

The other scenario with interacting electrons in strict 1D will lead to a breakdown of the Fermi liquid picture and result in Tomonaga-Luttinger liquid (TLL) behavior. Here the excitations of the system are no longer quasiparticles, but rather collective excitations of spin and charge.

Both scenarios, the Peierls instability and the TLL will be presented, as they are crucial for the interpretation of the experimental data obtained in this thesis.

2.1 Peierls instability

Starting with a free electron gas in one dimension without any electron-electron interactions, consider a linear chain of atoms, each occupied with one electron, fig. 2.1 top. This will result in a half-filled band and thus a metallic chain. Peierls proposed such a chain as being unstable against a charge density wave (CDW) at low temperature [22], which arises from a corresponding nesting condition in the Fermi surface. A metal-insulator transition with band gaps at the superstructure zone boundaries is spurred. In addition this is accompanied by a $\times 2$ periodic lattice distortion (PLD) due to phonon frequency renormalization, fig. 2.1 bottom. The ground state may be identified by the new superstructure in real space, or by energy gaps in the electronic structure, see fig. 2.2

In order to describe this phenomenon in more detail one has to start with a 1D electron gas and it's reaction to an external perturbation.

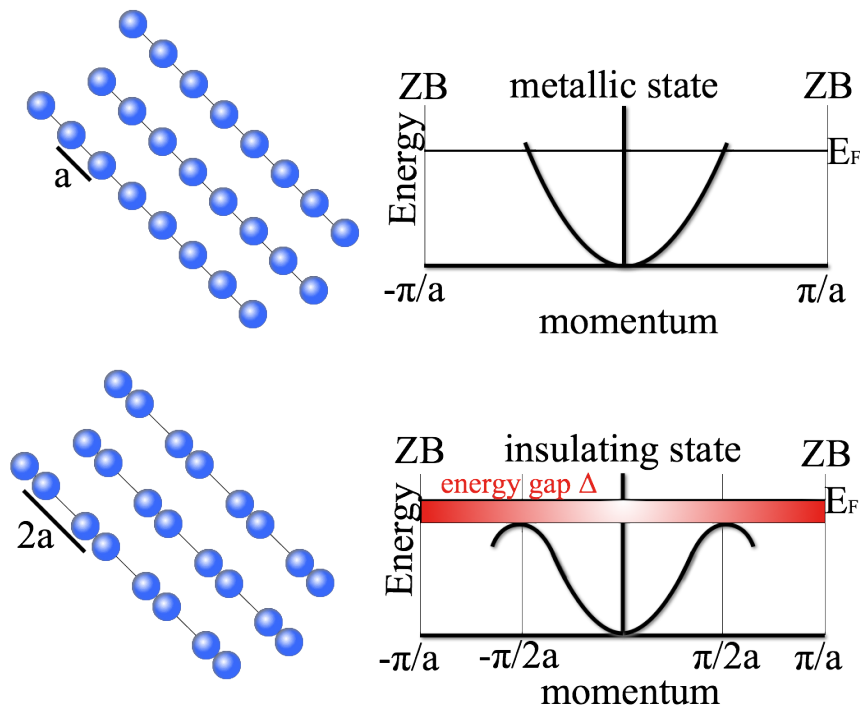


Figure 2.1: Schematic mechanism of the Peierls instability. Top: A linear chain of atoms occupied with one electron will result in a half filled band. Bottom: Below the critical temperature the chain will distort and open an energy gap at the new zone boundary.

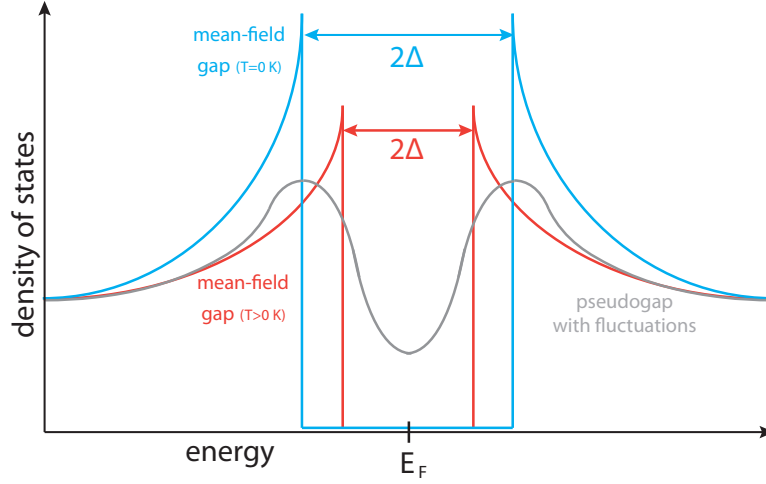


Figure 2.2: Mean-field description of the energy gap of the Peierls ground state. For $T = 0$ K the gap opens to its maximum size. At higher temperatures the gap size Δ shrinks according to the mean-field formalism. In the presence of fluctuations the Van-Hove-singularity will be smeared out and only a pseudogap will be observable. A gap observed in spectroscopy measurements may serve as a signature for a Peierls condensate. Compiled after [41]

2.1.1 Lindhard response function

The response of an electron gas to an external time dependent perturbation is given by the Lindhard dielectric function also called Lindhard response function. It is highly dependent on the dimensionality of the system. The time independent external potential is given as [41]

$$\Phi(\vec{r}) = \int_q \Phi(\vec{q}) e^{i\vec{q}\cdot\vec{r}} d\vec{q}, \quad (2.1)$$

where \vec{q} is the wave vector of the periodic perturbation. The induced charge density is then [40]

$$\rho^{ind}(\vec{r}) = \int_q \rho^{ind}(\vec{q}) e^{i\vec{q}\cdot\vec{r}} d\vec{q}. \quad (2.2)$$

They are related via the Lindhard response function $\chi(\vec{q})$

$$\rho^{ind}(\vec{q}) = \chi(\vec{q})\Phi(\vec{q}), \quad (2.3)$$

which for d dimensions is:

$$\chi(\vec{q}) = \int \frac{d\vec{k}}{(2\pi)^d} \cdot \frac{f(k) - f(k+q)}{\epsilon(k) - \epsilon(k+q)}. \quad (2.4)$$

$f(k)$ is the Fermi-Dirac distribution and $\epsilon(k)$ the electron energy. Assuming a linear dispersion in 1D the response simplifies to

$$\chi(\vec{q}) = -e^2 \cdot n(E_F) \cdot \ln \left| \frac{q + 2k_F}{q - 2k_F} \right|, \quad (2.5)$$

where $n(E_F)$ is the density of states at the Fermi energy E_F per spin. Note that $\chi(\vec{q})$ diverges for $q = 2k_F$. It can be interpreted that a spin or charge perturbation with a periodicity of $q = 2k_F$ will lead to an infinitely strong response in a 1D system at $T = 0$.

This is explained by so-called *perfect nesting* in the 1D Fermi surface. The main contribution to the integral in eq. 2.4 is due to pairs of electrons and holes at a distance $q = 2k_F$. Such pairs may be found for the 1D Fermi surface at every k_F , see fig. 2.3 (a). In higher dimensions perfect nesting is impossible. For a circular 2D Fermi surface or a spherical 3D Fermi surface only a single nesting vector may be found, see fig. 2.3 (b)+(c). Yet for anisotropic quasi-1D materials, the shape of the Fermi surface may be modulated to a certain degree and finite nesting becomes possible. This can be realized by a cosine modulation of the Fermi surface contour, see fig. 2.3 (d)

$$\epsilon(k) = \epsilon_0 + 2t_a \cos(k_x a) + 2t_b \cos(k_y b), \quad (2.6)$$

with the lattice constants a and b . For anisotropic crystals, $t_b/t_a \rightarrow 0$ [41], enough nesting conditions will be fulfilled. It follows:

$$\chi(q = 2k_F, T) = -e^2 n(E_F) \ln \left(\frac{1.14 \epsilon_0}{k_B T} \right), \quad (2.7)$$

where ϵ_0 is the Fermi energy. Again this expression is diverging for $T \rightarrow 0$.

2.1.2 Electron-phonon interaction

Until now the lattice has been completely neglected in the considerations on the modulation of the charge. The lattice of the system is usually included as a chain

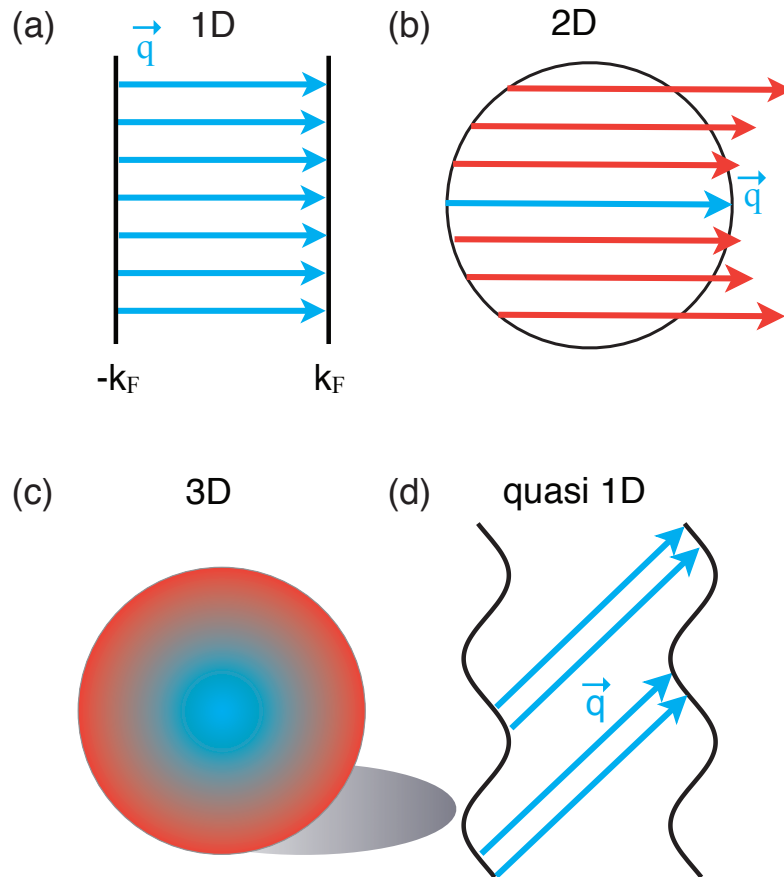


Figure 2.3: Fermi surfaces and nesting conditions for different dimensions. (a) For 1D perfect nesting is achieved. Each k_F can be connected with the same vector. For higher dimensions only poor nesting can be realized. (b) In 2D the Fermi surface is a circle and many inequivalent nesting vectors may be found. (c) This is also true for the 3D spherical Fermi surface. (d) The most realistic case is quasi-1D where the modulation of the straight 1D Fermi surface is described with a cosine function. Thus some nesting conditions will be fulfilled with the same vector.

of positively charged ions, surrounded by the free electron gas [41]. By switching on electron-phonon coupling in the model, a renormalized phonon spectrum is obtained with a softening of the phonon mode below a critical temperature. For a complete derivation within a mean-field approach in second quantization please refer to [41]. The resulting implications on the system are discussed in this chapter.

The phonon frequency is being renormalized to

$$\omega_{ren,q}^2 = \omega_q^2 + \frac{2g^2\omega_q}{\hbar}\chi(q, T), \quad (2.8)$$

where g is the electron-phonon coupling constant and ω_q represents the phonon frequency. As discussed in the previous chapter the response is highest for $q = 2k_f$, since the Lindhard dielectric function will diverge. Including eq. 2.7 into the renormalized phonon frequency, leads to

$$\omega_{ren,2k_F}^2 = \omega_{2k_F}^2 - \frac{2g^2n(\epsilon_F)\omega_{2k_F}}{\hbar} \cdot \ln\left(\frac{1.14\epsilon_0}{k_B T}\right). \quad (2.9)$$

For sufficiently low temperatures this expression results in a renormalized phonon frequency of 0 Hz. Hence the chain will perform a PLD with the same wavelength as the CDW. The critical temperature is

$$T_C = \frac{1,14}{k_B}\epsilon_0 e^{-\frac{1}{\lambda}}, \quad (2.10)$$

with the electron-phonon coupling constant λ . Close to the critical temperature the expression simplifies to

$$\omega_{ren,2k_F} = \omega_{2k_F} \left(\frac{T - T_C}{T_C}\right)^{1/2}. \quad (2.11)$$

Such behavior may be explained by looking at the temperature dependence of the Lindhard response function. At high temperatures the divergence at $q = 2k_f$ is smeared out due to thermal fluctuations. Towards lower temperatures these fluctuations fade and the CDW state is achieved much easier. Then the electrons screen the distortion of the lattice much more efficiently. Subsequently phonon modes with the same periodicity as the CDW will soften. Below the critical temperature this phonon will freeze and form the PLD eventually, see fig. 2.4.

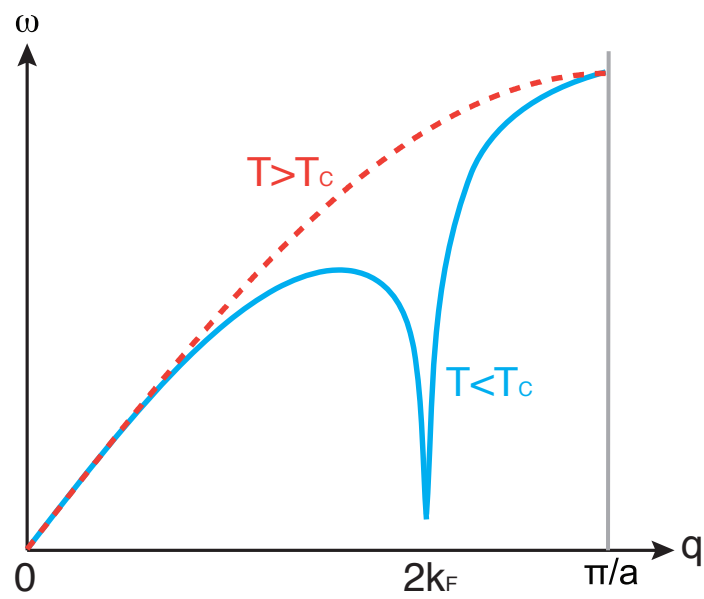


Figure 2.4: Phonon frequency renormalization due to electron phonon interaction. Far above T_C phonon dispersion is basically unaffected. Below T_C the phonon at $q = 2k_f$ freezes out and leads to a PLD.

2.1.3 Limitations of the Peierls picture

- **Long-range order:** In a perfect 1D system the long-range order will be disturbed by fluctuations above $T = 0$ K [42]. Consequently no CDW state will be realized. Therefore a finite coupling between the chains is needed in order to stabilize a long-range ordered state.
- **Mean-field formalism:** For the determination of the transition temperature a mean-field approach is used. It is, however a higher dimensional theory, which must fail in 1D. This is also the reason why the mean-field energy gap and the transition temperature do not follow the relation [41]

$$2\Delta = 3.52k_B T_{CDW}^{MF} \quad (2.12)$$

in real world systems as predicted mean-field theory. As a consequence, the transition temperature in reality is always be lower than T_{CDW}^{MF} . See, e.g. the Peierls transition temperature in $NbSe_3$, which is four times lower, than the predicted mean-field value [43].

- **Peierls relevance as driving force:** A recent theoretical study by Johannes *et. al* [44] has examined the stability of a Peierls ground state in a real world environment. They found, that such a state is easily destroyed at finite temperatures, imperfect nesting or by scattering. Moreover they conclude, that a nesting condition as a driving force for a phase transition is not sufficient. There needs to be an additional structural component to the transition in order to stabilized the distorted found state.

2.2 Tomonaga-Luttinger liquid

In the previous chapter electron-electron interactions were neglected and the system was essentially treated as a 1D electron gas. But what happens, if the interaction between the particles is switched on? The answer to this question was given independently by Tomonaga [45] and Luttinger [46] and later put together by Haldane to what he termed the Tomonaga-Luttinger liquid theory [23]. First the spinless description by Haldane will be presented and later the model will be generalized to include spin. Finally, the implications of a TLL system on the physics of the system as well as the measurable quantities in experiment will be discussed.

2.2.1 Excitations in one dimension

The dispersion relation of a 1D Fermi gas without interactions is shown in fig. 2.5 (a). All states below the chemical potential E_F are filled, while higher states are empty. The Fermi surface consists of two lines at $\pm k_F$. Consequently, low energy particle-hole excitations of such system can only have a momentum of $\Delta k = q \sim 0$ or $q \sim 2k_F$. Therefore, a gap opens in the particle-hole excitation spectrum as shown in fig. 2.5 (b). Note that such gap is easily filled in higher dimensions, where the Fermi surface is a circle and arbitrary connections between two Fermi points become possible. The energies of the excitations in 1D are [47]

$$E_k(q) = \epsilon(k+q) - \epsilon(k), \quad (2.13)$$

where $\epsilon(k)$ is the energy of the occupied and $\epsilon(k+q)$ the energy of the unoccupied state. Assuming a quadratic dispersion of the electron band

$$\epsilon(k) = \frac{\hbar^2}{2m}(k^2 - k_F^2), \quad (2.14)$$

and only looking at low energy excitations, one may simply expand the expression around k_F to

$$\epsilon(k) = \hbar v_F(k - k_F) + \frac{\hbar^2}{2m}(k - k_F)^2 + O(k^3), \quad (2.15)$$

with the Fermi velocity v_F . For $(k_F - q) < k < k_F$, the mean energy of an excitation $E(q)$ may be calculated using eq. 2.13 as [47]

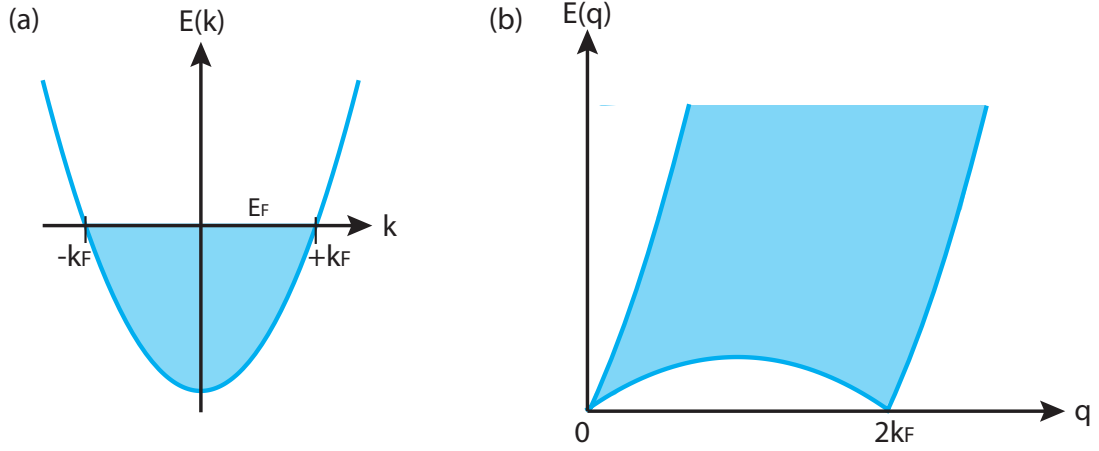


Figure 2.5: (a) Schematic of a quadratic dispersion relation of a 1D electron gas. Filled states up to the Fermi energy are shaded blue (b) 1D particle-hole excitation spectrum. Allowed excitations are in the shaded blue area. A gap opens up for low energy excitations and only $q \sim 0, 2k_F$ are allowed.

$$E(q) = \frac{\max(E_k(q)) + \min(E_k(q))}{2} \quad (2.16)$$

$$E(q) = \frac{1}{2}(\epsilon(k_F + q) - \epsilon(k_F) + \epsilon(k_F) - \epsilon(k_F - q))$$

$$E(q) \stackrel{eq.2.15}{=} v_F q.$$

Likewise one may consider the dispersion of these excitations as [47]

$$\delta E(q) = \max(E_k(q)) - \min(E_k(q)) \quad (2.17)$$

$$\delta E(q) = \epsilon(k_F + q) - \epsilon(k_F) - (\epsilon(k_F) - \epsilon(k_F - q))$$

$$\delta E(q) \stackrel{eq.2.15}{=} \frac{\hbar^2}{2m} q^2 = \frac{\hbar^2}{2mv_F^2} E(q)^2.$$

This means that the energy of a particle-hole excitations are linearly dependent on their momentum q . Since the excitations destroy a fermion and create another they are of bosonic character. Also the dispersion of these excitations goes faster to zero than the average energy, namely as $E(q)^2$, which implies increasing lifetime

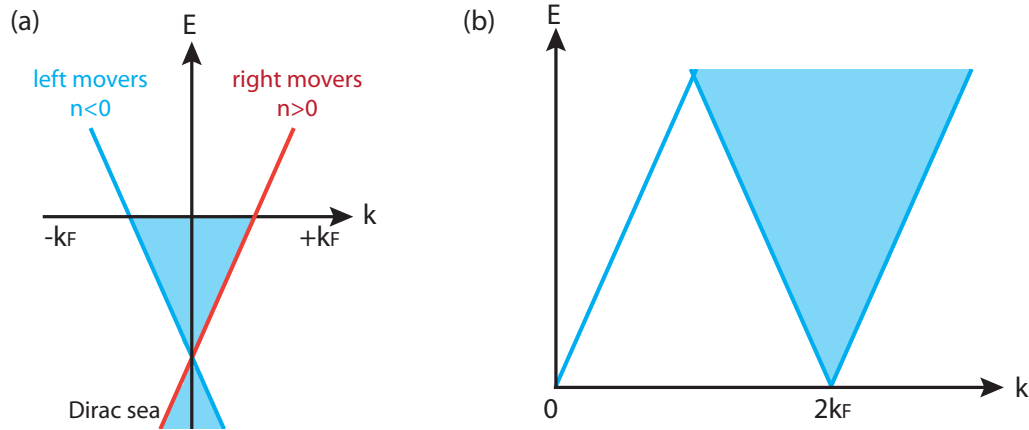


Figure 2.6: (a) Linearized dispersion relation in 1D. It is useful to divide the massless fermions into left- and right-movers. Occupied states in shaded blue. (b) According particle-hole excitation spectrum, which shows well defined excitations for low energies.

towards E_F . These two findings make the excitations well defined quasi particles, and thus point at a possible bosonic treatment of the 1D fermion system.

2.2.2 Tomonaga-Luttinger model and bosonization

In order to solve the problem of interacting fermions in 1D, and following the description of Schönhammer [48, 49], the Tomonaga-Luttinger (TL) model starts with the assumptions

- (i) The dispersion of the electrons may be linearized around $\pm k_F$.
- (ii) The interaction is weak and its range is longer than the mean particle distance (high density limit).
- (iii) There are only low energy excitations, which means no holes deep in the Fermi/Dirac sea and no high energy particles with $|k| - k_F \gg k_c$, where the cutoff is $k_c \ll k_F$.

Note that it is also possible to solve the problem under the assumption of an infinitely filled Dirac sea and extend the dispersion to $k = \pm\infty$ as originally performed by Luttinger [46]. Yet one has to deal with unphysical states and it can be shown to yield the same result as with the cut-off method, if the interaction is sufficiently weak [50].

If only forward scattering processes are considered, which will be discussed later, the TL model becomes exactly solvable [23]. The linearized dispersion of the 1D electron system and its excitation spectrum are shown in fig. 2.6. It is useful to treat the two branches of the 1D band separately and distinguish between left- and right-moving particles, see fig 2.6 (a). The linearization is readily justified for the low energy case [23]. Note, that the excitation spectrum for low energies again has a gap at low energies, see fig. 2.6 (b). Consequently the dispersion of the excitations is again linear around $q \sim 0, 2k_F$.

We will now discuss the concept of bosonization and later look at specific interaction scenarios. Starting with a linear dispersion around $\pm k_F$, and neglecting spin for the moment, the kinetic energy of the system in the second quantized form is given as [49]

$$\hat{T} = \sum_{n \geq 0} v_F(k_n - k_F) \hat{c}_n^\dagger \hat{c}_n + \sum_{n < 0} (-v_F)(k_n + k_F) \hat{c}_n^\dagger \hat{c}_n, \quad (2.18)$$

with the fermionic creation and annihilation operators \hat{c}_n^\dagger and \hat{c}_n . The equation has been separated into left and right moving particles, see fig. 2.6 (a). The Coulomb interaction in momentum space is given as [49]

$$\hat{V} = \frac{1}{2L} \sum_{n \neq 0} \tilde{V}(k_n) \hat{\rho}_n^\dagger \hat{\rho}_n + \frac{1}{2L} \hat{N}^2 \tilde{V}(0), \quad (2.19)$$

with the length of the system L , the particle number operator \hat{N} and the fourier transformation of the two-body interaction $\tilde{V}(k)$. The densities are expressed by the fermionic operators as

$$\hat{\rho}_n = \sum_{n' \geq 0} \hat{c}_{n'}^\dagger \hat{c}_{n'+n} + \sum_{n' < 0} \hat{c}_{n'}^\dagger \hat{c}_{n'+n} = \hat{\rho}_{n,+} + \hat{\rho}_{n,-} \quad ; \quad \hat{\rho}_n^\dagger = \hat{\rho}_{-n}. \quad (2.20)$$

Interestingly these density operators behave like bosons. For the low energy case, these follow the commutator relation [49]

$$[\hat{\rho}_{m,\alpha}, \hat{\rho}_{n,\beta}] = n \delta_{n,m} \delta_{\alpha,\beta} \hat{1}, \quad \alpha, \beta = +, -. \quad (2.21)$$

Consequently it is useful to construct new operators

$$\hat{b}_n = \frac{1}{\sqrt{|n|}} \begin{cases} \hat{\rho}_{n,+} & \text{for } n > 0 \\ \hat{\rho}_{n,-} & \text{for } n < 0, \end{cases} \quad (2.22)$$

which follow the well-known bosonic commutation relations

$$[\hat{b}_n, \hat{b}_m] = 0 \quad \text{and} \quad [\hat{b}_n, \hat{b}_m^\dagger] = \delta_{n,m} \hat{1}. \quad (2.23)$$

The Coulomb interaction may now be written in terms of these new bosonic operators

$$\hat{V} = \sum_{n>0} q_n \frac{\tilde{V}(k_n)}{2\pi} \left(\hat{b}_n^\dagger \hat{b}_n + \hat{b}_{-n}^\dagger \hat{b}_{-n} + \hat{b}_n^\dagger \hat{b}_{-n}^\dagger + \hat{b}_{-n} \hat{b}_n \right) + \frac{1}{2L} \tilde{V}(0) \left(\hat{N}_+ + \hat{N}_- \right)^2. \quad (2.24)$$

Likewise we find by inspection of the commutator of the kinetic energy with the bosonic density operator [49]

$$[\hat{b}_n^\dagger, \hat{T}] = v_F k_n \hat{b}_n^\dagger. \quad (2.25)$$

This means, that the bosonic operator \hat{b}_n^\dagger acts as the raising operator of the kinetic energy. This remarkable finding is known as the *Kronig identity* [51], which expresses the fermionic kinetic energy in terms of bosonic kinetic energy. Consequently we can also rewrite the kinetic energy in terms of these new bosonic operators:

$$\hat{T} = \sum_{n>0} v_F k_n \left(\hat{b}_n^\dagger \hat{b}_n + \hat{b}_{-n}^\dagger \hat{b}_{-n} \right) + \frac{\pi}{2L} v_F \hat{N}^2 + \frac{\pi}{2L} v_F \hat{J}^2, \quad (2.26)$$

with

$$\hat{J}^2 = \left(\hat{N}_+ - \hat{N}_- \right)^2, \quad (2.27)$$

which is the current density operator or the difference between left- and right moving particles. Note, that both the kinetic energy as well as the two-body interaction are quadratic in the bosonic densities, which makes the Hamiltonian trivial to

diagonalize. Consequently, we find for the Hamiltonian of the interacting fermions in the bosonic form

$$\begin{aligned}
 \hat{H} &= \hat{T} + \hat{V} \\
 &= \sum_{n>0} k_n \left\{ \left(v_F + \frac{\tilde{V}(k_n)}{2\pi} \right) (\hat{b}_n^\dagger \hat{b}_n + \hat{b}_{-n}^\dagger \hat{b}_{-n}) + \frac{\tilde{V}(k_n)}{2\pi} (\hat{b}_n^\dagger \hat{b}_{-n}^\dagger + \hat{b}_{-n} \hat{b}_n) \right\} \\
 &\quad + \frac{\pi}{2L} (v_N \hat{N}^2 + v_J \hat{J}^2) \\
 &= \hat{H}_{boson} + \hat{H}_{N,J},
 \end{aligned} \tag{2.28}$$

with the two velocities

$$v_N = v_F + \frac{\tilde{V}(0)}{\pi} \quad \text{and} \quad v_J = v_F. \tag{2.29}$$

Importantly since the boson operators commute with the particle number operators [23] the Hamiltonian may be split in two parts, which may be treated separately. The velocity v_N determines the energy cost for adding a particle [49], while v_J is the energy cost for changing the difference between left and right moving particles. Since the bosonic part of the Hamiltonian is separated one may diagonalize it by using the Bogoliubov transformation [23]

$$\hat{a}_n^\dagger = c_n \hat{b}_n^\dagger + s_n \hat{b}_{-n}. \tag{2.30}$$

This results in the diagonalized form

$$\hat{H}_{boson} = \sum_{n \neq 0} \omega(k_n) \hat{a}_n^\dagger \hat{a}_n + const, \tag{2.31}$$

with the dispersion relation

$$\epsilon(k_n) = \hbar\omega(k_n) = \hbar v_F |k_n| \sqrt{1 + \frac{\tilde{V}(k_n)}{\pi v_F}}. \tag{2.32}$$

For small k_n and smooth potentials $\tilde{V}(0)$, this results in a linear dispersion with a charge velocity of $v_C = \sqrt{v_J v_N}$

$$\epsilon(k_n) \approx \hbar |k_n| \sqrt{v_F \left(v_F + \frac{\tilde{V}(0)}{\pi} \right)} \stackrel{\text{eq. 2.29}}{=} \hbar |k_n| \sqrt{v_J v_N} = \hbar |k_n| v_C. \quad (2.33)$$

Note, that v_C is larger than v_F for $\tilde{V}(0) > 0$ [49], meaning that the charge velocity is increased over the Fermi velocity of the non-interacting system. For now we will not discuss the coefficients c_n and s_n from the Bogoliubov transformation, which will be more important in the upcoming chapter, when looking at specific interaction scenarios. The particles may interact via scattering processes, that are described in the so-called *g-ology*.

2.2.3 Interaction scenarios and g-ology

No interaction, no spin

The Hamiltonian for the case of non-interacting spinless particles is simply given by the kinetic energy as in eq. 2.26

$$\hat{H}_0 = \hat{T} = \sum_{n>0} v_F k_n \left(\hat{b}_n^\dagger \hat{b}_n + \hat{b}_{-n}^\dagger \hat{b}_{-n} \right) + \frac{\pi}{2L} v_F \left(\hat{N}^2 + \hat{J}^2 \right). \quad (2.34)$$

After diagonalization this leads to the trivial result of a single linear dispersion characterized by the Fermi velocity, see eq. 2.32 for $\tilde{V}(k_n) = 0$

$$\epsilon(k_n) = \hbar v_F |k_n| \quad (2.35)$$

Tomonaga-Luttinger model: Forward scattering, no spin

The low-energy interactions of 1D electrons are described in terms of scattering processes, which are summarized in the g-ology. Four possible cases exist, see fig. 2.7. These are:

- g_1 is $2k_F$ backscattering, where the particles switch branches. In the TL model this scattering is neglected which makes the model exactly solvable [47]. Note that for spinless Fermions g_1 and g_2 are the same, since one can not distinguish the outgoing particles.

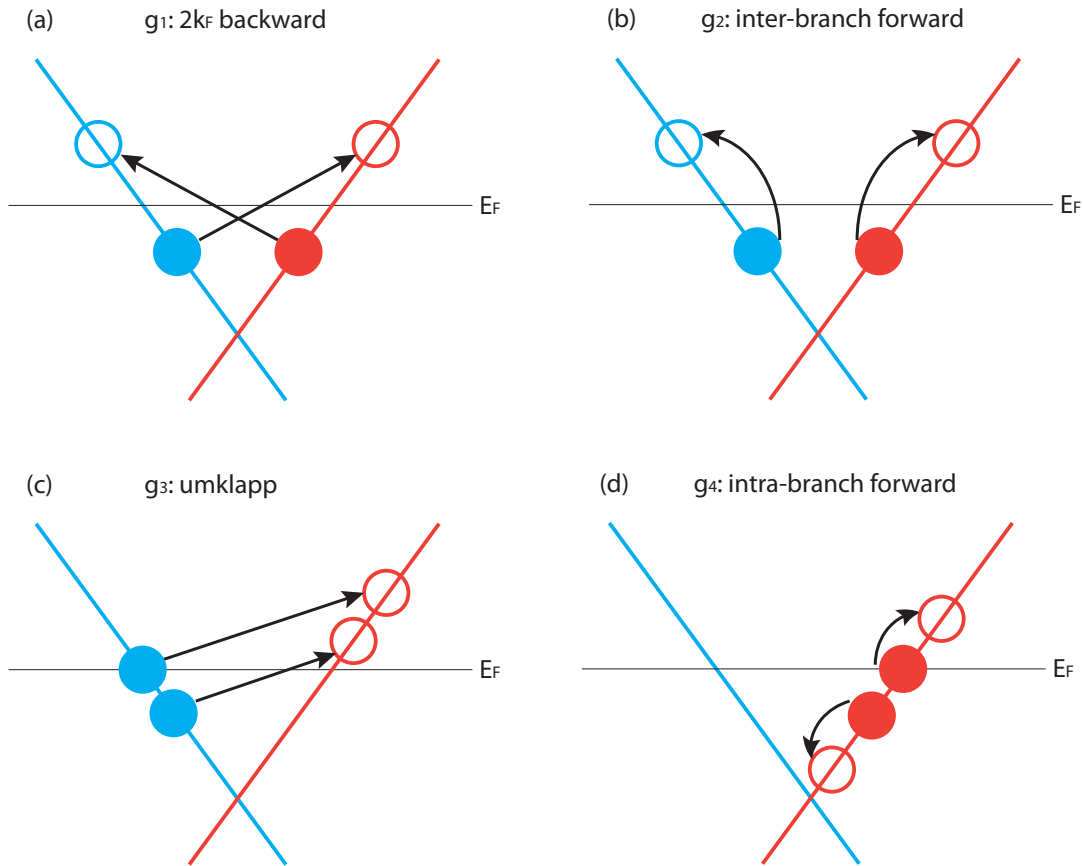


Figure 2.7: The four scattering processes in 1D (a) $2k_F$ backscattering, which is neglected in the TL model. (b) Inter-branch forward scattering. (c) Umklapp scattering is also neglected. (d) Intra-branch forward scattering. After [47].

- g_2 is inter-branch forward scattering. This means, that two fermions couple from each side of the Fermi surface, but each species stays inside its branch.
- g_3 is the umklapp scattering. This term is only relevant for special band fillings and therefore also neglected in the TL model.
- g_4 is intra-branch forward scattering and couples fermions from one branch of the Fermi surface.

Consequently only g_2 and g_4 are used in the TL model, which means, that only forward scattering will be relevant. The two interactions may be incorporated into the Hamiltonian eq. 2.28 and lead to the generalized form [49]

$$\begin{aligned} \hat{H}_{TL} = \sum_{n>0} k_n \left\{ \left(v_F + \frac{g_4(k_n)}{2\pi} \right) (\hat{b}_n^\dagger \hat{b}_n + \hat{b}_{-n}^\dagger \hat{b}_{-n}) + \frac{g_2(k_n)}{2\pi} (\hat{b}_n^\dagger \hat{b}_{-n}^\dagger + \hat{b}_{-n} \hat{b}_n) \right\} \\ + \frac{\pi}{2L} (v_N \hat{N}^2 + v_J \hat{J}^2), \end{aligned} \quad (2.36)$$

with

$$v_N = v_F + \frac{g_4(0) + g_2(0)}{2\pi} \quad \text{and} \quad v_J = v_F + \frac{g_4(0) - g_2(0)}{2\pi}. \quad (2.37)$$

In using again the Bogoliubov transformation to diagonalize the TL-Hamiltonian [49]

$$\hat{a}_n^\dagger = c_n \hat{b}_n^\dagger + s_n \hat{b}_{-n}, \quad (2.38)$$

one finds for the coefficients

$$c_n = \frac{1}{2} \left(\sqrt{K_n} + \frac{1}{\sqrt{K_n}} \right) \quad \text{and} \quad s_n = \frac{1}{2} \left(\sqrt{K_n} - \frac{1}{\sqrt{K_n}} \right), \quad (2.39)$$

with

$$K_n = \sqrt{\frac{v_J(k_n)}{v_N(k_n)}}, \quad (2.40)$$

and the renormalized velocities

$$v_{N,J}(k_n) = v_F + \frac{g_4(k_n) \pm g_2(k_n)}{2\pi}. \quad (2.41)$$

This means, that the TL model is an exactly solvable model for interacting electrons in one dimension! The dispersion is given as

$$\epsilon(k_n) = \hbar |k_n| \sqrt{v_J(k_n) v_N(k_n)} = \hbar |k_n| v_c, \quad (2.42)$$

with the charge velocity v_c . The interaction strength is given by the so-called *stiffness coefficient* K_n . $K_n < 1$ is repulsive and $K_n > 1$ attractive interaction. $K_n = 1$ is the non-interacting case. This can be easily seen in

$$K_n = 1 = \sqrt{\frac{v_J(k_n)}{v_N(k_n)}} \Rightarrow v_J(k_n) = v_N(k_n) \stackrel{eq.2.41}{=} v_F, \quad (2.43)$$

which yields the same dispersion as eq. 2.35.

Note, that the low energy physics of a 1D interacting spinless fermion system is described only by two parameters: The stiffness constant K_n and the charge velocity v_c . This solution to the TL model was first performed by Haldane [23], who also showed in his seminal paper, that even for non-linear dispersions these relations survive.

Spin-charge separation: Forward scattering, with spin

Up to now the spin of the electrons has been completely neglected. As it turns out the inclusion of spin is rather straight forward [49]. One starts again with the kinetic energy and two body interaction as eqs. 2.18 and 2.19 and follows the bosonization procedure with some additional considerations. First one adds spin labels to fermionic operators [49]

$$\hat{c}_n^\dagger(\hat{c}_n) \rightarrow \hat{c}_{n,\sigma}^\dagger(\hat{c}_{n,\sigma}) \quad \text{with} \quad \sigma = \uparrow, \downarrow \quad (2.44)$$

and to the density operators

$$\hat{\rho}_n \rightarrow \hat{\rho}_{n,\sigma}. \quad (2.45)$$

Therefore, also the boson operators generalize to

$$\hat{b}_n \rightarrow \hat{b}_{n,\sigma}. \quad (2.46)$$

The interactions will also have to include spin

$$g_\nu(k_n) \rightarrow g_\nu^{\sigma,\sigma'}(k_n) = \delta_{\sigma,\sigma'} g_{\nu,\parallel}(k_n) + \delta_{\sigma,-\sigma'} g_{\nu,\perp}(k_n) \quad , \quad \nu = 2, 4. \quad (2.47)$$

Now it is useful to construct new boson operators for charge (ρ) and spin (σ)

$$\hat{b}_{n,\rho} = \frac{1}{\sqrt{2}}(\hat{b}_{n,\uparrow} + \hat{b}_{n,\downarrow}) \quad \text{and} \quad \hat{b}_{n,\sigma} = \frac{1}{\sqrt{2}}(\hat{b}_{n,\uparrow} - \hat{b}_{n,\downarrow}). \quad (2.48)$$

This allows the kinetic energy to be separated into spin and charge parts, which commute [49]. Also the interaction matrix elements may be rewritten in terms of spin and charge

$$g_{\nu,\rho}(k_n) = g_{\nu,\parallel}(k_n) + g_{\nu,\perp}(k_n) \quad (2.49)$$

$$g_{\nu,\sigma}(k_n) = g_{\nu,\parallel}(k_n) - g_{\nu,\perp}(k_n) \quad , \quad \nu = 2, 4 \quad (2.50)$$

as well as the particle number operators

$$\hat{N}_{\alpha,\rho/\sigma} = \frac{1}{\sqrt{2}} \left(\hat{N}_{\alpha,\uparrow} \pm \hat{N}_{\alpha,\downarrow} \right) \quad \text{with} \quad \alpha = +, -. \quad (2.51)$$

Finally, we are able to write down the TL-Hamiltonian for spin 1/2 fermions

$$\hat{H}_{TL}^{1/2} = \hat{H}_{TL,\rho} + \hat{H}_{TL,\sigma}, \quad (2.52)$$

where each $\hat{H}_{TL,\rho/\sigma}$ is of the form eq. 2.36. This means, that the Hamiltonian is separated into spin and charge excitations, which may be treated independently. This property is called *spin-charge separation*. Diagonalizing the two Hamiltonians leads to the dispersions

$$\epsilon_\rho(k_n) = \hbar v_\rho |k_n| \quad , \quad v_\rho = \sqrt{v_{J,\rho} v_{N,\rho}} \quad , \quad K_\rho = \sqrt{\frac{v_{J,\rho}}{v_{N,\rho}}} \quad (2.53)$$

$$\epsilon_\sigma(k_n) = \hbar v_\sigma |k_n| \quad , \quad v_\sigma = \sqrt{v_{J,\sigma} v_{N,\sigma}} \quad , \quad K_\sigma = \sqrt{\frac{v_{J,\sigma}}{v_{N,\sigma}}}. \quad (2.54)$$

Consequently the TL-system is characterized by two velocities for spin and charge excitations and by two stiffness coefficients K_ρ and K_σ that describe the interaction strength. This means that the excitations of the 1D electron gas may be treated as two indecent species of particles. These are called *spinon*, carrying the spin excitation and *holon*, carrying the charge excitation. Of course in experiments, probing

the system is only possible by adding or removing one single electron to/from the 1D chain. So the response of the TLL system to such an external perturbation has to be known, in order to interpret the experimental data. This response is given by the spectral function of the system, which may now be finally calculated with the results of this chapter.

2.2.4 Spectral function

Spectroscopic measurements like angle resolved photoemission spectroscopy (ARPES) or scanning tunneling spectroscopy (STS) inject or remove one electron to/from the system. The response to such perturbation is given by the single-particle Green's function. However its treatment, and especially the calculation of the measurable spectral function is not straight forward, but rather lengthy and cumbersome. Consequently there is a wealth of theoretical publications on the topic [34, 48, 49, 52–57]. Therefore the calculation will only be sketched here in order to obtain some measurable quantity for comparison with the STS data of chapter 6.3.2.

For the spinful TL model the Green's function at $T = 0$, an infinitely long chain $L \rightarrow \infty$ and $r = 2/k_c$ is [48, 49]

$$ie^{iE_F t} G_+^<(x, t) = \frac{-i}{2\pi} e^{ik_F x} \prod_{a=\rho, \sigma} \frac{1}{(x - v_a t - i0)^{1/2}} \left(\frac{r^2}{(x - v_a t - ir)(x + v_a t + ir)} \right)^{s_a^2/2}, \quad (2.55)$$

where E_F is the chemical potential, + denotes that only right-movers are treated, and < indicates an electron removal process. The spectral function is calculated from the Green's function via a double fourier transformation in time and space to energy and k-space [48, 49]. STS will always probe the angle integrated spectral function, which will be focussed on here. If the interaction of the electrons is spin rotation invariant (SU(2)), then $K_\sigma = 1$ and the calculation of the angle-integrated spectral function follows as [49]

$$\rho_+(\omega, T = 0) \sim \int_{-\infty}^{\infty} dt e^{i\omega t} i e^{i\mu t} G_+^<(0, t) \quad (2.56)$$

$$\sim (-\omega)^{s_\rho^2} \Theta(-\omega), \quad (2.57)$$

which can be written in terms of the anomalous dimension α

$$\rho_+(\omega, T = 0) \sim (-\omega)^\alpha \Theta(-\omega) \quad \text{with} \quad \alpha = s_\rho^2 = \frac{1}{4}(K_\rho + K_\rho^{-1} - 2). \quad (2.58)$$

More generally the exponent α is given by

$$\alpha = \frac{1}{4}(K_\sigma + K_\sigma^{-1} + K_\rho + K_\rho^{-1} - 4), \quad (2.59)$$

but it simplifies to eq. 2.58 for spin rotational invariant interactions $K_\sigma = 1$.

The angle integrated spectral function thus follows a power law over energy close to the chemical potential with the anomalous dimension α . When examining the temperature dependence at the chemical potential, it can be similarly shown that it also follows a power law upon temperature with the same exponent [49]

$$\rho_+(\omega = 0, T) \sim T^\alpha. \quad (2.60)$$

The complete temperature and energy dependence for small $\omega \ll v_F q_C$ and $T \ll v_F q_C$ is given by using the Fermi-Dirac function $f(x) = (e^x + 1)^{-1}$ [27, 58, 59]

$$\rho(\omega, T) \sim f(\omega/T) T^\alpha \cosh(\omega/T) \left| \Gamma \left(\frac{1 + \alpha}{2} + i \frac{\omega}{2\pi T} \right) \right|^2. \quad (2.61)$$

This is an important finding, since the measurable density of states (DOS) only depends on terms with ω/T , and thus it is possible to perform a universal scaling relation to yield a universal curve for all temperatures and energies. This will be important, when analyzing the temperature dependent tunneling spectra in chapter 6.3.2

2.2.5 Tomonaga-Luttinger model with boundary

Up to now the description of the 1D system in terms of the TL model considered an infinitely long chain. In the tunneling experiments presented in this thesis it is also possible to study open boundary chains, i.e. chain ends at terrace steps or at defects. An advanced treatment of the Green's function with a position dependence for the distance from the chain end is performed to address such effect [34]. As it turns out for large distances from the end, the same result is recovered as in the

previous chapter for the infinite chain. Yet, more importantly at the boundary a similar result for the spectral function as for the infinite case may be found, with [34]

$$\rho(\omega, 0) \sim |\omega|^{\alpha_B} \quad \text{with} \quad \alpha_B = \frac{K_\rho^{-1} + K_\sigma^{-1}}{2} - 1. \quad (2.62)$$

The boundary exponent is increased over the bulk value, which leads to an increased suppression of the DOS towards the chemical potential at the chain end. This should be detectable in STS, when performing spectroscopy close a chain end.

The crossover region between the edge and bulk was first modeled by Eggert *et al.* [36]. They have calculated the spectral function depending on the distance from the chain end for a semi-infinite chain. The result is shown in fig. 2.8. The spectral function $\rho(\omega x)$ is plotted over a universal axis $(\omega x/v_C)$ with the distance from the chain end x and the charge velocity v_C . Note that there is a crossover between the two exponents. Two cases may be distinguished

$$\omega x/v_C < 1 \rightarrow \alpha_{end} \quad (2.63)$$

$$\omega x/v_C > 1 \rightarrow \alpha_{bulk} \quad (2.64)$$

At low energies the edge exponent dominates the spectrum, while towards higher energies the bulk regime is recovered. The crossover is dependent on both energy and distance from the edge. Importantly the low energy part will always be dominated by the edge exponent. Yet the energy scale shrinks with the distance from the edge with $\propto 1/x$ [36]. Consequently far away from the chain end only the bulk value will be measurable in experiments.

Note, that starting from the crossover region the curve begins to oscillate, fig. 2.8. These oscillations are not due to $2k_F$ Friedel scattering, but are a result from the calculations within the Hubbard model and importantly should be observable in experiments. However the oscillations vanish asymptotically with $\sin(2\omega x/v_C)(\omega x)^{-13/16}$ [36] and therefore require high resolution spectroscopy data to be resolved.

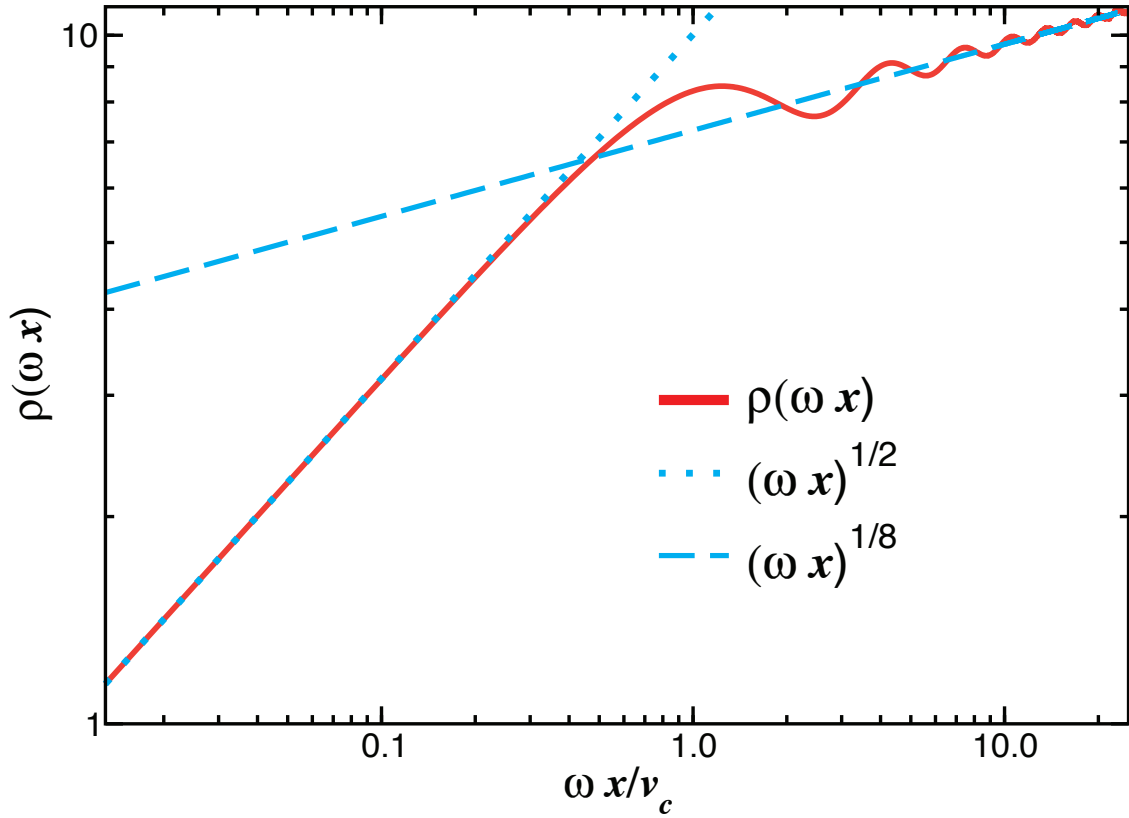


Figure 2.8: Spectral function $\rho(\omega x)$ plotted on the universal axis $\omega x/v_c$ in arbitrary units. At fixed boundary distance r , the low energy part is governed by the edge exponent, while at higher energies there is a crossover to the bulk regime. Note that the oscillations are not due to Friedel oscillation but result from the calculations within the Hubbard model. After [36], plot S. Eggert, private communications.

2.2.6 Summary

Since the treatment of the TLL physics can be quite lengthy, it is useful to summarize the theoretical findings that will be most important for the experimental studies in a brief list.

- (i) Fermionic excitations in 1D may be described as bosons.
- (ii) Spin and charge excitations may be treated separately.
- (iii) The TL state is described by the two stiffness constants K_ρ and K_σ as well as the charge and spin velocity v_ρ and v_σ .
- (iv) The DOS is predicted to follow a power law depression at low energies with $\rho = |\omega|^\alpha$ with $\alpha = s_c^2 = \frac{1}{4}(K_\sigma + K_\sigma^{-1} + K_\rho + K_\rho^{-1} - 4)$.
- (v) The DOS is predicted to obey universal scaling behavior over energy and temperature and may be described with
$$\rho(\omega, T) \sim f(\omega/T) T^\alpha \cosh(\omega/T) \left| \Gamma\left(\frac{1+\alpha}{2} + i\frac{\omega}{2\pi T}\right) \right|^2.$$
- (vi) At the chain end the power-law exponent is predicted to change to
$$\alpha_B = \frac{K_\rho^{-1} + K_\sigma^{-1}}{2} - 1.$$
- (vii) There is a crossover region between bulk and end states, which may be observed as a kink in the tunneling spectrum. Also oscillations around the crossover region may be detected at very high energy resolution.

2.2.7 Limitations of the Tomonaga-Luttinger model

- **One band:** All considerations made were for a single band with two crossings of the Fermi energy. Yet real world systems will likely comprise a more complex band situation. This is also the case for the scrutinized Au chains on Ge(001), which is a two band (four branch) system. Additional modeling by theory will be needed in this direction.
- **Non-linear dispersion:** The TL-model is strictly only valid for an linear dispersion and for low energy excitations. In experiment however one may access also higher energy excitations by ARPES and STS and thus the criterion for linearity may no longer be met. There are first works towards a

spinless non-linear TLL theory [60–62], but a complete model for fermions has not yet been established [63, 64].

- **Phonons:** Lattice contributions have been completely neglected in the TL-model. However in real-world systems it is not possible to separate the electrons from the lattice. Consequently above zero temperature there will also be phonons present in the system that might couple to the TLL state and potentially lead to a Peierls transition, thus rendering the system insulating.

3 Experimental methods for surface analysis

“If there is no duct tape involved it’s not an experiment, it’s a measurement” (Carsten Detlefs, ESRF)

3.1 Tunneling microscopy

The scanning tunneling microscope was first introduced by Binnig and Rohrer in 1981 [65, 66]. For the first time they combined a vibration isolation system with a piezoelectric scanner and an atomically sharp tip in order to record the topography of a surface. Although the technology already existed at their time, many scientists in the field did not believe in the feasibility of a scanning tunneling microscopy (STM). However, until today it has developed to a versatile and powerful tool to study the local topographic and spectroscopic properties of a surface with atomic resolution.

3.1.1 Basic principle

Tunneling effect

The tunneling effect describes the ability of quantum mechanical objects, like electrons, to tunnel through a thin barrier, which is classically forbidden. In fig. 3.1 the lion in a classical world is not allowed to leave the quantum well and the human next to it is safe. Yet, if the barrier of the well is thin enough and the lion is assumed to be quantum mechanical, he has a finite probability to tunnel outside of the well. In STM this mechanism is used by placing a metallic tip in a few nanometer proximity to the sample surface and applying a voltage between the

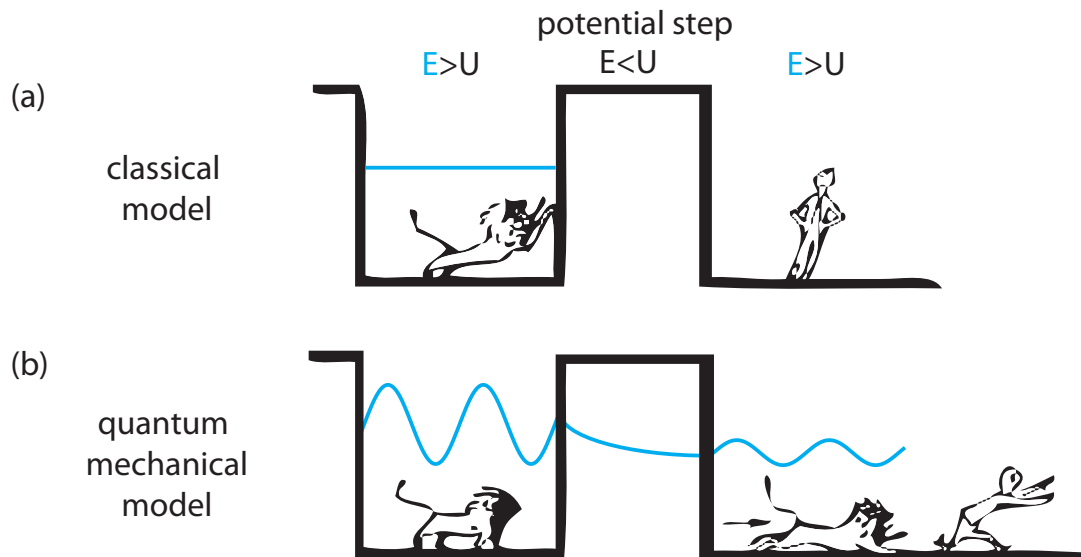


Figure 3.1: Difference between classical and quantum-mechanical view. (a) In QM the lion has a finite probability to tunnel through the potential barrier, while (b) classically he would not be allowed to leave the quantum well. After [67].

two. The electrons will tunnel between the tip and the surface, which is measured as a current. Since the tunneling probability is exponentially dependent on the tip-surface distance, the height of a homogeneous sample may be scanned in sub Å precision [68]. The lateral resolution is basically given by the tip apex, which is (preferably) the dimension of a single atom.

Image acquisition

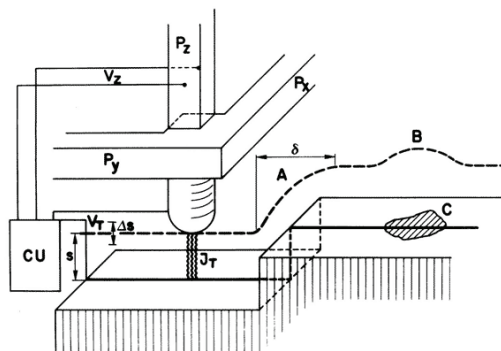


Figure 3.2: Schematic setup of a STM. The tip is moved by three piezo crystals over the surface, while the tunneling current is held constant. At a step (A) or at a material with higher DOS (B) the tip is displaced by the feedback loop. [65, 66].

The original principal setup of the STM is shown in fig. 3.2. The tunneling tip is brought within a few nanometers distance to the sample surface, by moving the P_Z piezodrives. In using the piezoelectric effect it is possible to position the tip with picometer precision in all three dimensions [69]. As soon as the desired setpoint tunneling current is detected by the feedback loop the approach stops. In order to scan the surface textbooks distinguish two modes:

- (i) The first mode is termed *constant-current*, because the tip height is always adjusted to keep the tunneling current at the specified setpoint. The tip is subsequently moved by the P_X and P_Y piezos, describing a line by line scan of the surface. At every point the tunneling current is measured and the height is adjusted. Thereby a topographic line profile is created. At steps or protrusions, fig. 3.2 (A), the tip is displaced to follow the contour. Yet also at areas with different DOS, as seen in area (C), the tip is displaced to match the constant current criterium. This shows very nicely, that in STM one measures only profiles of constant DOS. Therefore the interpretation of images always has to include structural and electronic properties of the scrutinized material. This will also be seen in the images of the Au/Ge(001) nanowires in chapter 5.3.
- (ii) The second scanning mode is called *constant-height*. This mode is much faster, since the tip is held at a defined distance to the surface and the current is recorded. So no feedback loop is needed for the image acquisition. Yet this mode is only applicable for flat samples, like metal crystals. Otherwise the chance of a tip crash at constant height is very likely.

In real measurements there is always an admixture of both modes, and the feedback loop as well as the scan speed may be adjusted to blend between the two. Therefore always the height as well as the tunneling current is detected at all times. However for slow scan speeds the feedback loop is given enough time to adjust the tip height at every point of the sample and one may assume that the signal was acquired in constant current mode. This was the preferred method for all data presented in this thesis.

3.1.2 Tunneling current

Tersoff and Hamann provided the first theoretical description of the tunneling current between the tip and sample [70, 71]. Although their model includes some simplifications about the wave function and geometry of the tip and is only valid for small applied voltages, it has been most successful in describing the physics of STM. This model will be presented here by following the two seminal publications Refs [70, 71]. One starts by using Bardeen's transfer Hamiltonian approach for the tunneling between two metals, separated by a thin oxide layer [72]. Accordingly, the current is given as

$$I_T = \frac{2\pi e}{\hbar} \sum_{\mu,\nu} f(E_\mu)[1 - f(E_\nu + eU)] |M_{\mu\nu}|^2 \delta(E_\mu - E_\nu), \quad (3.1)$$

where $f(E)$ is the Fermi-Dirac distribution, U the applied bias, Ψ_μ and Ψ_ν are the eigenstates of tip and sample, respectively. The delta function provides the energy conservation. $M_{\mu\nu}$ represents the transition matrix element between the two independent eigenstates and may be expressed as

$$M_{\mu\nu} = \frac{\hbar^2}{2m} \int (\Psi_\mu^* \vec{\nabla} \Psi_\nu - \Psi_\nu \vec{\nabla} \Psi_\mu^*) d\vec{S}, \quad (3.2)$$

where the integral runs over an arbitrary surface between tip and sample. With the simplification of low temperatures and small biases $U < \Phi$, where Φ is the work function, the Fermi-Dirac distributions are eliminated and the expression turns to

$$I_T = \frac{2\pi}{\hbar^2} e^2 U \sum_{\mu,\nu} |M_{\mu\nu}|^2 \delta(E_\nu - E_F) \delta(E_\mu - E_F), \quad (3.3)$$

where E_F is the Fermi energy of tip and sample in equilibrium.

Point probe

Considering the simplest case of a point probe, the tip eigenfunctions are arbitrarily localized and the matrix-element is simply proportional to the square amplitude of the wave function of the sample at the position of the tip \vec{r}_0

$$I_T \propto \sum_{\nu} |\Psi_\nu(\vec{r}_0)|^2 \delta(E_\nu - E_F). \quad (3.4)$$

With this simple expression it is already apparent, that the tunneling current depends on the local density of states (LDOS) of the sample at the Fermi energy at the location of the tip. As stated earlier, this means that the STM records profiles of constant LDOS rather than actual topography.

Modeled tip

In order to provide a more realistic situation of the tunneling experiment, the calculation of the matrix element $M_{\mu\nu}$ in eq. 3.1 is the most challenging part. Therefore one has to assume some symmetries of the wave functions of tip and sample. For a periodic surface, one may perform a fourier expansion of the wave function of the sample

$$\Psi_\nu = \Omega_s^{-\frac{1}{2}} \sum_{\vec{G}} a_G \exp \left[- \left(\kappa^2 + |\vec{k}_\parallel + \vec{G}|^2 \right)^{\frac{1}{2}} z \right] \times \exp(i(\vec{k}_\parallel + \vec{G}) \cdot \vec{x}), \quad (3.5)$$

where Ω_s is the sample volume and $\kappa = \hbar^{-1} \sqrt{2m\Phi}$ is the inverse decay length of the wave function into vacuum, Φ is the work function of the surface. \vec{k}_\parallel is the Bloch-vector of the surface state and \vec{G} is the reciprocal lattice vector of the unit cell. In a non-periodic scenario the sum over \vec{G} is replaced by an integral.

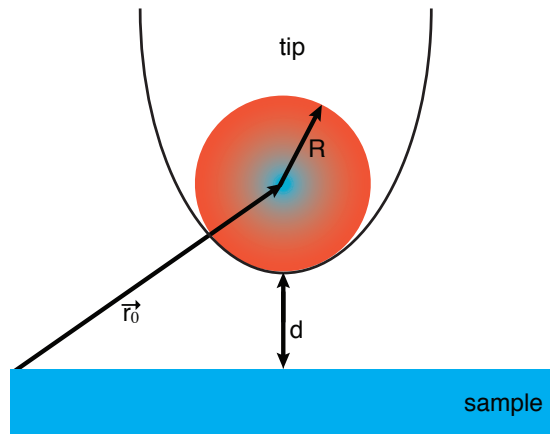


Figure 3.3: The simplified tip model after Tersoff and Hamann [70, 71], assuming a spherical tip with s -orbital wave function at a distance d away from the surface.

For the geometry of the tip, Tersoff and Hamann assumed the tip to be spherical, with a radius R at the distance d to the surface, see fig. 3.3. The vector \vec{r}_0 points from the coordinate origin to the center of the tip. Generally one has no information about the tip wave function, since it depends on the material of the tip and its geometry. Yet, for the region of interest one may assume the wave function to be described as a spherical s-orbital

$$\Psi_\mu = \Omega_t^{-\frac{1}{2}} c_t \kappa R e^{\kappa R} (\kappa |\vec{r} - \vec{r}_0|)^{-1} e^{-\kappa |\vec{r} - \vec{r}_0|}, \quad (3.6)$$

where Ω_t is the probe volume. c_t is a parameter, that depends on the tip geometry, its electronic structure and the tip-vacuum boundary condition. For $R \gg \kappa$ it is of the order of unity. For simplicity it is assumed, that the work function of tip and sample are equal. Again, this function may be expanded to

$$(\kappa r)^{-1} e^{-\kappa r} = \int d^2 q b(\vec{q}) \exp[-(\kappa^2 + q^2)^{1/2} |z|] \times \exp(i\vec{q} \cdot \vec{x}), \quad (3.7)$$

$$b(\vec{q}) = (2\pi)^{-1} \kappa^{-2} (1 + q^2/\kappa^2)^{-1/2}. \quad (3.8)$$

With these two wave functions for tip and sample the calculation of the matrix element eq. 3.2 becomes straightforward and the tunneling current eq. 3.1 may be calculated to

$$I_T = 32\pi^3 e^2 V \Phi^2 D_t(E_F) R^2 \hbar^{-1} \kappa^{-4} e^{2\kappa R} \times \sum_\nu |\Psi_\nu(\vec{r}_0)|^2 \delta(E_\nu - E_F), \quad (3.9)$$

where D_t is the density of states per unit volume of the tip. The sum basically represents the density of states of the sample at the Fermi energy. This is in accordance with the point probe result of eq. 3.4 and again means, that the STM records profiles of constant DOS. A closer inspection of the sum term reveals that

$$|\Psi_\nu(\vec{r}_0)|^2 \propto \exp[-2\kappa(R + d)] \quad (3.10)$$

and therefore the tunneling current shows exponential dependence of the tip-sample distance

$$I_T \propto e^{-2\kappa d}, \quad (3.11)$$

which explains the high sensitivity of STM. Note that the result of Tersoff and Harman is strictly valid only for

- (i) Small applied voltages $U < \Phi$.
- (ii) Spherical tip with s-orbital.

The first criterium is mostly fulfilled for all spectroscopy experiments presented in this thesis. Considering the tip orbital, most spectra were taken, using a Gold tip. Gold has a 6s valence state, so the assumption of s-like states holds. Some samples were also measured with a tungsten tip, which has a 5d state at the Fermi energy. Orbitals with angular dependence are weighted by $(1 + q^2/\kappa^2)^{-1/2}$ in the matrix element [69]. However this weighting only becomes important for large tip radii R and may therefore be neglected.

High bias regime

When performing tunneling microscopy on semiconductors, the low bias assumption is not always justified, since bonds at the surface may lie several eV below or above the Fermi energy. However, such states are only important for the bonding geometry and the structure of the sample and don't contribute to the conduction properties, which only depend on the electrons close to E_F . The exact treatment of a high bias tunneling scenario is challenging, since the eigenstates of sample and tip may depend on the applied voltage. For simplicity one assumes that these states do not change with the bias. By applying the Wenzel-Kramers-Brillouin-approximation (WKB) for planar tunneling, the current follows as [67]

$$I_T = \int_{E_F}^0 \rho_s(\vec{r}, E) \cdot \rho_t(\vec{r}, E - eV) T(E, eV, \vec{r}) dE, \quad (3.12)$$

where ρ_s and ρ_t are the DOS at \vec{r} of sample and tip, respectively. E is measured from the individual Fermi levels. The tunneling transmission probability is given as:

$$T(E, eU) = \exp\left(-2(d+R)\sqrt{\frac{2m}{\hbar^2}\left(\frac{\Phi_t + \Phi_s}{2} + \frac{eU}{2} - E\right)}\right) = \exp(-2\kappa d), \quad (3.13)$$

where Φ_t and Φ_s are the work functions of tip and sample. A closer inspection of the transmission probability T may be divided in two regions

- (i) $eU > 0$, positive sample bias, unoccupied sample states
- (ii) $eU < 0$, negative sample bias, occupied sample states.

In both cases the tunneling probability is highest for $E = 0$ eV, meaning that electrons at the Fermi energy of the negatively biased electrode will always dominate the signal. Deeper lying states will be exponentially damped by T .

Assuming a structureless DOS of the tip material, this means it is possible to (i) selectively tunnel into the *unoccupied states* of the sample, see fig. 3.4 (a). The leading edge of the tunneling current will always be dominated by the states at E_F of the tip. The reverse scenario however (ii) will always be dominated by the *unoccupied states* of the sample at the Fermi energy, fig. 3.4 (b). Again it should be stressed, that such effect is only relevant for high biases and does not effect the spectroscopy data shown in the current thesis. The structural observations will, on the other hand be affected by the transmission probability. This will be important, when analyzing the structure of the nanowires in chapter 5

3.2 Tunneling spectroscopy

As laid out in the previous chapter the STM records a signal, which is a convolution of topography and density of states. This fact may be used to locally measure the DOS of the sample and thereby collecting structure and electronic information simultaneously. Such capability is unique to the STM and has therefore made it a

very powerful tool to study the interplay of structure and electronics. A measurement may be performed by collecting $I(V)$ spectra with the feedback loop turned off, or by using a lock-in amplifier. Both methods were used in this thesis.

3.2.1 $I(V)$ spectra and extraction of the density of states

In order to record $I(V)$ spectra, the tip is rastered across the surface in constant-current mode and a topographic image is obtained. At the desired position, the tip is stopped and eventually the feedback loop is opened. The tip now rests at constant distance to the surface. Subsequently the bias is ramped over a voltage range, e.g. ± 0.1 V and the current is recorded. After the measurement is done, the feedback loop is turned on again and the scan continues. Usually such spectra are affected by noise, even at low temperature and long integration times. So the measurement is performed several times for statistical confidence.

As shown in eq. 3.12, the tunneling current may be described as

$$I_T = \int_{E_F}^0 \rho_s(\vec{r}, E) \cdot \rho_t(\vec{r}, E - eV) T(E, eV, \vec{r}) dE. \quad (3.14)$$

Assuming a constant DOS of the tip and a constant tunneling probability over the scrutinized voltage range, the derivative of the expression simplifies to

$$\frac{dI_T}{dV} \propto \rho_s(r, E). \quad (3.15)$$

So the derivative of the $I(V)$ curve will directly display the LDOS of the sample. Note, that the derivative will be even more affected by noise than the $I(V)$ curve itself. Therefore in the current thesis up to 65000 spectra have been averaged for one single dataset over equivalent sample areas to gain statistical confidence.

As a remark, for higher bias windows, e.g., ± 1 V it is more common to use the normalized conductivity

$$\frac{dI/dV}{I/V} = \frac{d \ln(I)}{d \ln(V)}, \quad (3.16)$$

because this expression eliminates the bias dependence of the transmission probability as well as the tunneling setpoint. However, by definition the normalized

conductivity is 1 at 0 V bias and therefore any physics taking place at the Fermi energy may not be detected.

3.2.2 Lock-In spectroscopy

In using a lock-in amplifier, the signal to noise ratio may be dramatically increased, yet on the cost of longer measurement times. Thereby the tunneling voltage is modulated with a periodic sine or cosine bias, which has a frequency higher than the cutoff of the feedback loop. Therefore the image acquisition is not affected by the periodic signal. The amplitude may be set to a desired value. Higher amplitude will result in a better signal, yet it will also average over that bias window and therefore over features in the sample DOS. The amplifier then compares the tunneling current for a signal with the same frequency and phase. This signal is then directly proportional to dI/dV and will therefore reflect the LDOS [65, 66, 74, 75]. With this method it is not only possible to perform tunneling spectroscopy $dI/dV(V)$ but also to scan the surface with a fixed voltage. The resulting image acquired from the lock-in channel will then render the spatially resolved DOS at a fixed energy. Such measurements have been performed in chapter 6.2, to detect the conduction channels at the scrutinized nanowire surface.

3.3 Low energy electron diffraction

In the wake of quantum mechanics and in a time when the wave nature of matter was not yet fully established, Davisson and Germer by serendipity discovered electron diffraction from a Nickel crystal in 1927 [76]. Due to progress in ultra-high vacuum (UHV) technology and the simplicity of this powerful method, low energy electron diffraction (LEED) has developed to a powerful tool to study the quality and long-range order of a crystal surface. Informations, that may be collected by this technique are:

- (i) By inspection of the diffraction pattern and knowledge of simple geometrical scattering theory the unit cell of the surface may be revealed.
- (ii) By using the kinematic theory to analyze the diffraction spot profiles one finds information about the domain size as well as temperature effects.
- (iii) By variation of the kinetic energy of the primary electrons and recording of the spot intensity, intensity vs. voltage LEED (I(V)-LEED), information about the atomic positions within the unit cell may be gained. This requires to apply the advanced dynamical theory of scattering to account for the strong interaction between slow electrons and matter.

The Au nanowires on Ge(001), studied in this work are scrutinized with LEED using the first two methods in order to probe the delicate long-range order and to study the second order phase transition occurring in this system, see chapter 5.

Principle

A typical schematic for a LEED instrumentation is shown in fig. 3.5. Electrons are emitted from a heated filament and focussed by a Wehnelt cylinder. A lens system then accelerates the electrons into the grounded drift tube and subsequently onto the sample. In order to produce a field free region the sample and the first grid of the optics are grounded. The diffracted electrons then pass through the grid optics. The second grid is at slight negative potential in order to repel inelastically scattered electrons. The fraction of elastically scattered electrons is only few percent, since the excitation probability of plasmons for slow electrons is very high [77], see fig.

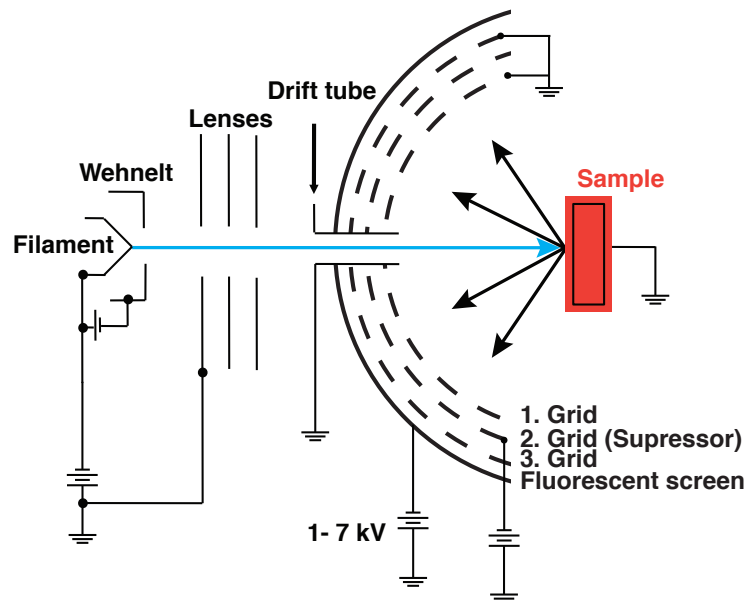


Figure 3.5: Schematic of a typical LEED optics setup. Electrons are emitted from a filament and subsequently accelerated onto the sample. The diffracted electrons then pass a set of grids at different potentials and are then accelerated onto a fluorescent screen. In looking from the filament side the pattern may be seen on the screen. After [77].

3.6. A third and optionally a fourth grid allow focussing onto the fluorescent screen, which is at high positive potential of 1-7 kV. The diffraction pattern is then visible on the screen, when looking from the filament side.

3.3.1 Surface sensitivity

Since electrons interact very strongly with matter [77], as compared to i.e. X-rays, their mean free path is only of the order of a few nanometers. This is especially true for slow electrons. In fact the mean free path for electrons in a solid obeys the so called *universal curve* for many different materials, see fig. 3.6 [78]. This characteristic behavior has a pronounced minimum at 50-100 eV, where the probability of plasmon excitation in the sample is the highest [79]. It subsequently decreases for lower and higher energies and therefore the mean free path increases. For typical LEED settings between 20 and 150 eV the mean free path is approximately 1.5 - 2 nm only. Therefore the surface of the sample will dominate the signal acquired.

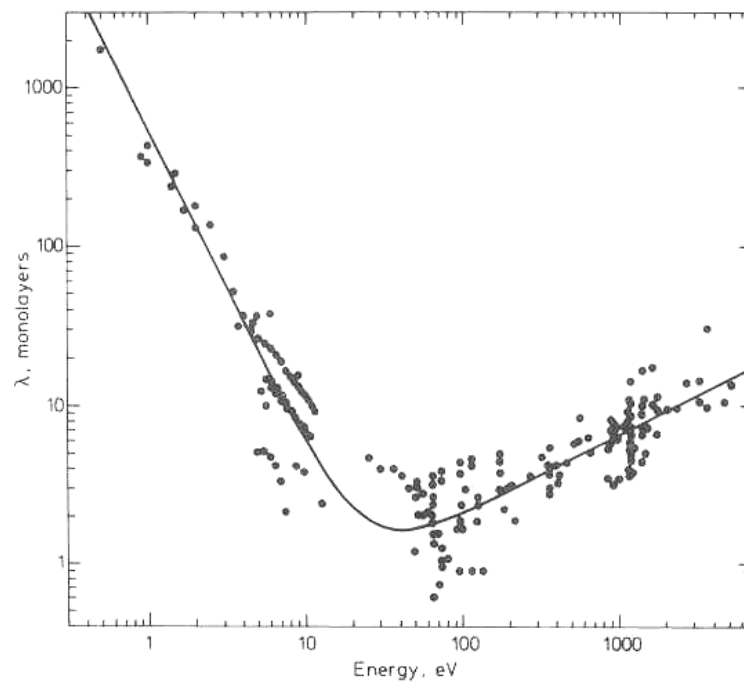


Figure 3.6: *The mean free path of electrons in matter as a function of their kinetic energy [78]. A universal curve results for virtually all materials which has its minimum around 50-100 eV. There the portability to excite plasmons and inelastically scatter is the highest.*

3.3.2 Geometric theory

The two dimensional lattice of a surface may be described within the framework of five Bravais lattices that are spanned by the vectors \vec{a}_j [40]. The corresponding reciprocal lattice vectors \vec{b}_i have to fulfill the condition

$$\vec{b}_i \cdot \vec{a}_j = 2\pi\delta_{ij}, \quad (3.17)$$

where the Kronecker delta $\delta_{ij} = 1$ for $i = j$ and $\delta_{ij} = 0$ for $i \neq j$. This means, that the reciprocal vectors are orthogonal to their real space counterparts. Using the normal vector of the surface \vec{n} the reciprocal lattice vectors may be constructed using [80]

$$\vec{b}_1 = 2\pi \frac{\vec{a}_2 \times \vec{n}}{|\vec{a}_1 \times \vec{a}_2|} \quad \vec{b}_2 = 2\pi \frac{\vec{n} \times \vec{a}_1}{|\vec{a}_1 \times \vec{a}_2|}. \quad (3.18)$$

Consequently a reciprocal lattice vector at a surface is defined by

$$\vec{G} = h \cdot \vec{b}_1 + k \cdot \vec{b}_2. \quad (3.19)$$

Since the translational symmetry perpendicular to the surface is infinite, the reciprocal lattice points in this direction are infinitely dense, resulting in a rod at each \vec{G} . Therefore a scattering condition for electrons at a surface is much easier fulfilled than in a bulk crystal. This condition is nicely described by the Laue equations, which can be deduced from simple geometrical considerations as shown in fig. 3.7. Two atoms from a crystal are placed at a distance \vec{R} . The incoming electron wave is described by the vector \vec{k} and the scattered wave by \vec{k}' . Constructive interference will only occur, if

$$x + x' = \frac{\vec{k} \cdot \vec{R}}{k} - \frac{\vec{k}' \cdot \vec{R}}{k'} = n\lambda, \quad (3.20)$$

where n is a positive integer and λ the wavelength of the electron. In case of elastic scattering, $k = k' = 2\pi/\lambda$, this simplifies to

$$\Delta\vec{k} \cdot \vec{R} = 2\pi n \quad \text{with} \quad \Delta\vec{k} = \vec{k} - \vec{k}'. \quad (3.21)$$

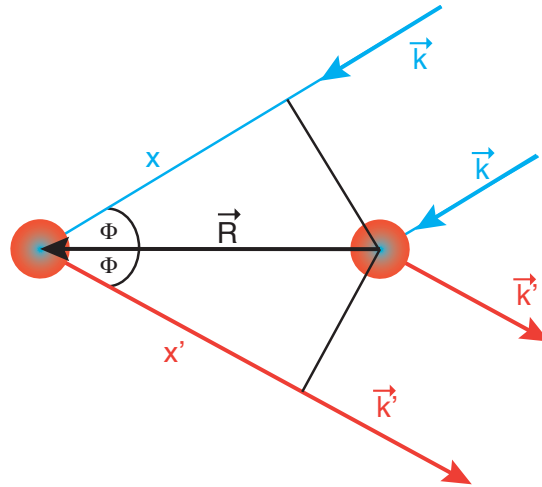


Figure 3.7: Geometrical description of the scattering condition at a crystal. This simple consideration leads to the Laue equations for scattering. \vec{k} is the incoming electron wave and \vec{k}' the scattered wave. \vec{R} corresponds to the lattice vector of the surface.

Since \vec{R} corresponds to a lattice vector, this is exactly the definition for a reciprocal lattice vector as in eq. 3.17. This formula is known as the Laue equation. Therefore scattering will occur, if

$$\Delta\vec{k} = \vec{G}. \quad (3.22)$$

A very helpful representation of the scattering condition is the Ewald construction, fig. 3.8. The surface lattice will result in rods in reciprocal space. For elastic scattering the Ewald sphere has a radius of $|\vec{k}|$ with its circumference fixed at the origin of coordinates. In case of normal electron incident, as in LEED, this results in a situation as depicted in fig. 3.8. At every intersection of the Ewald sphere with the rods a solution to the Laue equations exists and in this direction electrons will be scattered. Consequently the LEED pattern is a direct representation of the reciprocal lattice of the surface.

Note that by tuning the primary energy of the electrons the radius of the sphere may be set. For high energies the circle will grow and therefore more scattering conditions will match. Yet also the scattering angles become steeper. Therefore upon increasing the primary energy in LEED, the diffraction spots will move closer to the backscattered (0,0) spot.

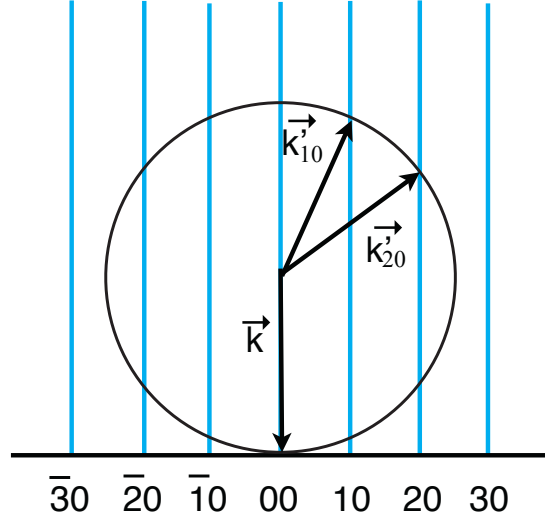


Figure 3.8: Ewald construction for a surface lattice. At each intersection of the Ewald sphere with a crystal truncation rod, a scattering condition is fulfilled. After [81]

3.3.3 Kinematic theory

The kinematic theory is based on the assumption of weak interaction between the scatterer and the radiation. This is justified for X-rays or fast electrons. However for slow electrons as in LEED also multiple scattering events have to be considered to describe the complete picture. Nonetheless the kinematic theory is useful for judgement of the disorder at the surface, which also includes temperature effects. These will be important when analyzing the phase transition in the Au nanowires in chapter 5.

Consider a plane electron wave with the wavelength λ that is traveling in direction \vec{s}_0 [77]

$$\Psi = \Psi_0 e^{i\vec{k}_0 \vec{r}}, \quad (3.23)$$

with the wave vector $\vec{k}_0 = \frac{2\pi}{\lambda} \vec{s}_0$. As sketched in fig. 3.9 the point of observation lies at X, which is far away from the sample. A scattered wave from \vec{R}_j arrives with an amplitude

$$\Psi = \left(\Psi_0 \frac{e^{i\vec{k}_0 \vec{R}}}{R} \right) \cdot f_j(\vec{k}_0, \vec{k}) e^{i(\vec{k} - \vec{k}_0) \vec{R}_j}. \quad (3.24)$$

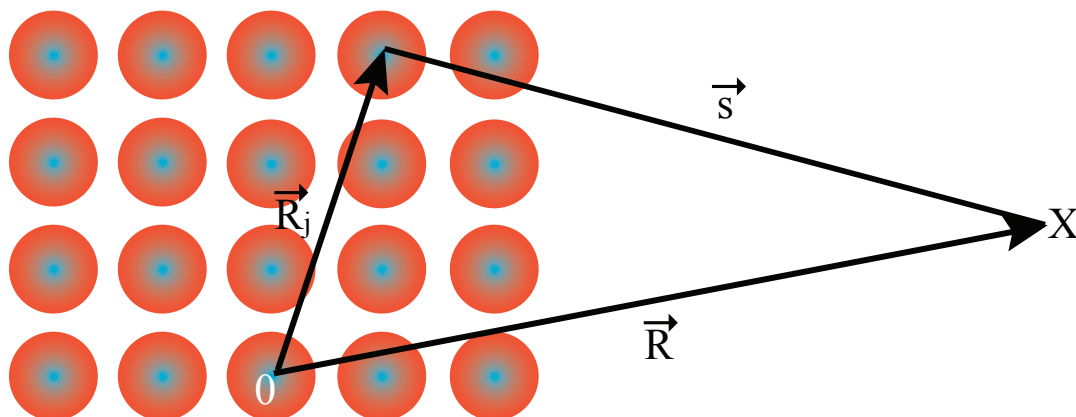


Figure 3.9: Electron scattering schematic for the kinematic theory of diffraction. The point of observation X is far away from the origin. The scattered wave arrives from \vec{s} . Summation over all \vec{s} yields the diffracted intensity.

The first term again describes the plain wave. The second is the atomic scattering factor and the third gives the phase shift between the origin and the point of observation. Summation over the complete crystal surface leads to

$$\Psi \propto \sum_j f_j(\vec{k}_0, \vec{k}) e^{i(\vec{k}-\vec{k}_0)\vec{R}_j}. \quad (3.25)$$

The sum over all atoms may be split in two terms with a lattice periodic factor G and an atom or structure factor F , that describes the arrangement within the unit cell [77]

$$\Psi \propto F \cdot G. \quad (3.26)$$

Of course the measurable quantity in experiment is the square of the waves amplitude

$$I \propto |\Psi|^2 = |F|^2 |G|^2. \quad (3.27)$$

Basically G contains information on the long range order of the surface and domain size. F on the other hand contains information on the atoms within the unit cell. In the dynamical theory of diffraction G is unaltered but special attention is paid to the structure factor F , since multiple scattering events have to be accounted for. Yet, even in the kinematic theory the temperature dependence of the

surface and influence of movement of the atoms may be estimated. These effects are described by the Debye Waller factor [81].

3.3.4 Debye-Waller factor

As laid out in the previous chapter, the scattering amplitude depends on the square of the structure factor F^2 , which contains the position of the atoms within the unit cell. Yet, above zero temperature this position is not fixed, but a function of time, since the atoms will begin to vibrate in the lattice. This may be described by the time dependent position of the j^{th} atom $\vec{R}_j(t)$ [40, 77]

$$\vec{R}_j(t) = \vec{r}_j^0 + \vec{u}_j(t), \quad (3.28)$$

where \vec{r}_j^0 is the equilibrium position of the atom and $\vec{u}_j(t)$ is the time-dependent thermal vibration. Inserting this in eq. 3.24 and only considering the structure contributions (ignoring contributions from the lattice) this yields

$$I \propto |\Psi|^2 = |F|^2 = I_0 e^{-((\Delta k)^2 \cdot \langle u^2(t) \rangle)}, \quad (3.29)$$

where I_0 is the scattering amplitude of the fixed lattice and $\Delta k = k - k_0$. $\langle u^2(t) \rangle$ is the mean square displacement of the atoms. By assuming independent motion of the atoms and using Debyes theory of specific heat [40, 77]:

$$\langle u^2(t) \rangle = \frac{3h^2}{4\pi^2 m k_B} \cdot \frac{T}{\Theta_D^2}, \quad (3.30)$$

with m the atom mass, k_B Boltzmanns constant and Θ_D the Debye temperature. In using the Laue condition eq. 3.21 and the condition for constructive interference eq. 3.20 this yields

$$\Delta k = \frac{4\pi \cos(\phi)}{\lambda}, \quad (3.31)$$

where λ is the electron wavelength and ϕ is the scattering angle. Insertion of eqs. 3.30 and 3.31 in eq. 3.29 yields

$$I = I_0 \cdot e^{-2M} \quad \text{with} \quad 2M = \frac{12h^2}{m k_B} \left(\frac{\cos \phi}{\lambda} \right)^2 \cdot \frac{T}{\Theta_D^2}. \quad (3.32)$$

The exponential function is known as the Debye Waller factor. Important consequences are that the scattering intensity

- (i) decreases with increasing temperature.
- (ii) decreases for higher electron energies (shorter wavelengths).
- (iii) depends on the scattering angle (strongest influence on the 0th order reflex).

These considerations will be important in the discussion on the phase transition in the Au nanowires in chapter 5.7.2.

3.4 Experimental setup

Low-temperature STM

The majority of the experiments were performed at the low-temperature STM (LT-STM) in the Matzdorf group at the University of Kassel. Therefore the description of the experiment will be limited to this commercially available setup. Ultra high vacuum conditions are necessary to ensure sufficiently long measurement times before the surface is covered with adsorbents. Consequently the chamber consists of three parts:

- (i) A fast entry load-lock for introduction of samples and tunneling tips,
- (ii) A preparation chamber (PC) for surface cleaning and evaporation of gold for the self organized nanowires,
- (iii) An analysis chamber (AC) housing the two cryostats and the STM therein.

A schematic of the setup may be seen in fig. 3.10 (a) and (c). The base pressure of the PC and AC was 5×10^{-11} mbar and never exceeded 1×10^{-9} mbar during sample preparation or transfer. This regime is reached by a combination of turbo molecular and ion getter pumps. Especially the getter pumps are necessary to have no moving parts at the chamber during an STM measurement. This minimizes vibrational disturbances.

The Au/Ge(001) nanowires were prepared as described in chapters 4.3 and 5.2. An Omicron Sepcta-LEED installed in the preparation chamber was used to ensure surface quality before inserting the sample into the cryostat, but also to study the temperature dependence of the phase transition, see chapter 5.7.2.

STM measurements were performed with an Omicron LT-STM either at a base temperature of 77 K with liquid nitrogen (LN₂) or at 4.7 K with liquid helium (LHe). Temperatures in between could be accessed by a resistive heater, that was installed at the STM base. A picture of the STM stage is shown in fig. 3.10 (b). The sample enters face down and the tunneling tip on the tube scanner approaches from below. An eddy current damping system along with three springs supplies the necessary decoupling from the rest of the chamber. In addition the complete setup rests on a dedicated foundation in the basement.

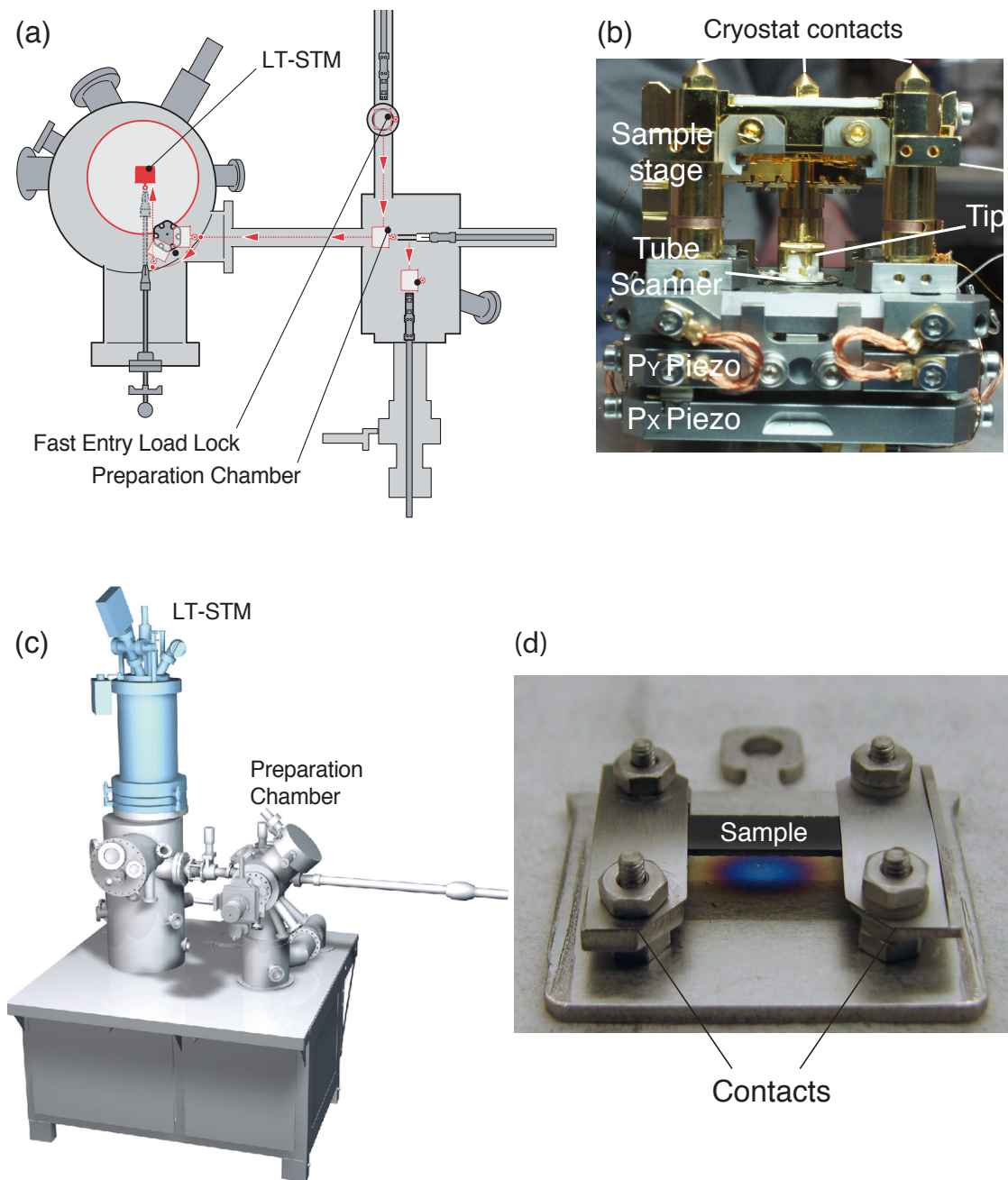


Figure 3.10: (a) Schematic of the UHV setup for LT-STM measurements and sample preparation. (b) Sample stage of the LT-STM, removed from the cryostats. (c) 3D view of the setup with the cryostat in blue. [82] (d) Sample holder of the LT-STM. The sample is contacted on both top and bottom with Mo stripes.

The sample holder for direct current heating is shown in fig. 3.10 (d). The sample is clamped between two Molybdenum stripes in the center of the sample carrier. Therefore the sample is contacted both on the top and the bottom. This will be important, when discussing the circuiting of the tunneling spectroscopy experiment in chapter 6.3.1. One side of the sample holder is isolated in order to inject the heating current needed for the sample preparation. In the tunneling experiment both sides are connected to ground.

Considering the performance of the STM preamplifier, the resolution broadening due to electronics has been determined on an energy gap of a superconductor to 5 meV [25]. Additional broadening is induced in some measurements by the amplitude of the lock-in amplifier, as well as temperature broadening of the tunneling tip. This will be discussed at each relevant section in chapter 6 on the tunneling spectroscopy results.

Variable-temperature STM

Considering the STM measurements above room temperature, an Omicron variable temperature STM (VT-STM) was used. It is attached to a PC which offers the same preparation possibilities as stated above. The base pressure in this chamber is 1×10^{-10} mbar and never exceed 1×10^{-9} mbar during preparation. After preparation the sample is transferred into the STM, where first an image is acquired at room temperature (RT). When the tip condition is stabilized a direct heating current may be applied to the sample in order to increase the temperature. The voltage drop over the sample is accounted for in the tunneling circuit. Using high scan speeds to avoid thermal drift, it becomes possible to study the sample surface above room temperature as presented in chapter 5.7.1 for the study of the phase transition.

ARPES using Synchrotron radiation

For completeness, the ARPES measurements were performed at two different synchrotron light sources.

- (i) Advanced Light Source (ALS), Berkeley, USA: The ARPES band maps and the Fermi-surface were measured at the Electronic structure factory, beamline 7.0.1 with a Scienta R4000 analyzer at a photon energy of $h\nu = 100$ eV with a total resolution of ~ 30 meV. These results are presented in chapter 6.1
- (ii) Swiss Light Source, Villigen, CH: The high resolution line shape of the 1D band, as shown in chapter 6.3.1, was measured the SIS beamline using a photon energy of $h\nu = 21.2$ eV and a Scienta R4000 analyzer. The total energy resolution could be reduced to ~ 10 meV.

Details and results about the synchrotron experiments on the Au/Ge(001) nanowires may be found in [A.6, A.16]. For more general information on the synchrotron setup and experiments see the recent introductory book by P. Willmott [83].

4 Choosing the substrate

“There is plenty of room at the bottom.” (Richard Feynman, 1959)

4.1 Previous studies on nanowires at surfaces

Growing 1D nanostructures at surfaces is a challenging task. The most crucial factor on the resulting chain structure is the choice of the right substrate. Nearly all previous studies to date have been performed on the Si surfaces [84]. These are the In chains on Si(111) and the Au reconstruction on the stepped silicon substrates Si(553) and Si(557). Earlier studies on these systems focussed on the importance of Peierls physics as well as TLL behavior, see chapter 2. The local structure of such surface reconstructions can be studied with STM very conveniently. The electronic structure may be probed using ARPES with high precision. Consequently these systems seem to be the ideal candidates for the examination of the above mentioned low dimensional properties. For comparison with the results of this thesis, a short review of these three most thoroughly studied nanowire reconstructions with the most important findings will be given here.

4.1.1 In chains on Si(111)

When depositing In on Si(111) the threefold symmetry of the surface is broken. This leads to the formation of 1D nanowires. This is the first nanowire system at a surface, where the occurrence of a Peierls transition has been claimed. The seminal paper of Yeom *et. al* [31] served as the prototypical case of proof of a charge density wave at a nanowires surface reconstruction. They found, that upon deposition of In the surface reconstructs in a $p(4\times 1)$ unit cell. In STM nanowires are observed, which are four atoms wide and consist of two closely neighboring In zig-zag chains [31], see fig. 4.1 (a) left. ARPES measurements find three surface

states, which are all metallic at room temperature [85], see fig. 4.1 (a) left. The band fillings of these three states are $m_1 = 0.11$, $m_2 = 0.38$ and $m_3 = 0.50$. In addition the m_3 band shows a highly anisotropic character, which was determined from tight binding fits of the Fermi surface contour, see [85]. The resulting ratio of the transfer integral is $\frac{t_{\parallel}}{t_{\perp}} = 72$. This makes the In/Si(111) surface a prime example for the Peierls scenario with half filling, see chapter 2.1.2.

Upon cooling to 120 K the chain structure is found to undergo a symmetry breaking phase transition with a doubling of the periodicity in chain direction, see fig. 4.1 (a) right. This was further supported by electron diffraction [31]. At the same time the bandstructure is altered and only two bands may be detected in ARPES. These new bands are both back folded at the $\times 2$ zone boundary (\bar{K} -point), thereby matching the new real space periodicity and making the surface insulating. This is explained by a charge transfer of the m_1 to the m_2 band, which then has a band filling of $m_2' = 0.49$. It matches the half filling scenario and stabilizing the CDW ground state [85], see fig. 4.1 (c). Consequently all indications of a Peierls instability are presented, like the CDW in real space and the metal-insulator transition (MIT) due to the back folding of the bands with a corresponding nesting condition. With these findings the system seems to perfectly coincide with the model described by Peierls.

However subsequent theoretical calculations found that the $\times 2$ distortion of the In chains does result in the correct ground state and also not to an insulating surface [86]. Therefore the Peierls mechanism alone may not explain the ground state. Further calculations proved, that the inclusion of a shear phonon is necessary, leading to the formation of In hexagons in the ground state [87, 88]. This new structure leads to an insulating band situation with the m_1 band shifted above the Fermi energy and both the m_2 and m_3 band backfolded at the $\times 2$ zone boundary. These calculations therefore reproduce both experimental findings from STM and ARPES. Yet in this scenario the driving force of the transition is not the Peierls instability, but rather the softening of the shear phonon at 120 K [87, 88]. Consequently the paradigmatic character for a Peierls instability in this surface system is at least partially rebutted.

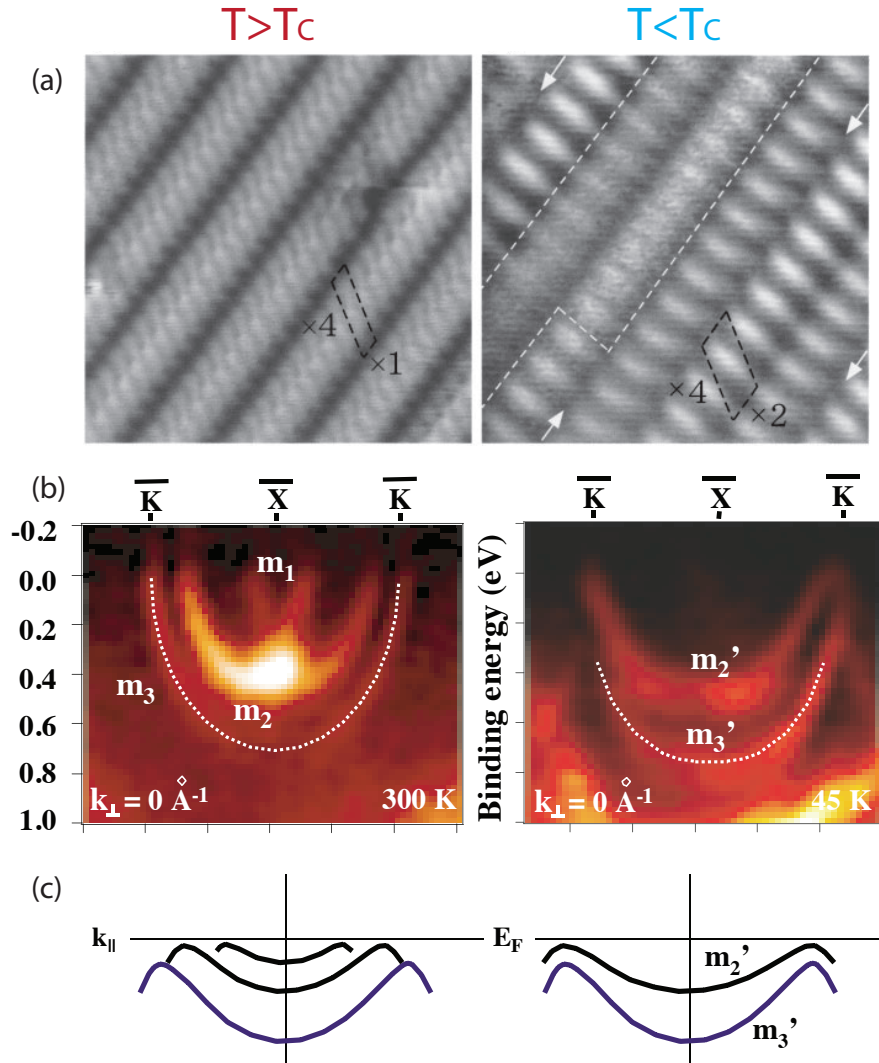


Figure 4.1: (a) STM image of the In/Si(111) nanowire reconstruction above the transition (left) and below (right), from [31]. A period doubling may be observed in the LT phase. (b) ARPES measurements of the In/Si(111) surface above (left) and below (right) the critical temperature, from [85]. (c) A backfolding of the bands at the new zone boundary \bar{K} is seen in the LT phase. In addition only two bands remain, from [85].

4.1.2 Au chains on Si(557)

A fundamentally different approach to grow self organized nanowires is the use of miscut substrates. In the case of Si(557) the (111) surface is miscut by 9.5° towards the $[\bar{1}\bar{1}2]$ direction. The resulting surface is stepped with a terrace width of 1.92 nm [89]. Deposition of Au leads to the reconstruction of three kinds of chains. On each terrace a chain of Au atoms that are incorporated into the first layer exists [90]. Additionally the Si atoms at the step edges form honeycomb chains of Si hexagons [90]. The structure is similar to that of graphene. Furthermore Si adatoms form a third chain. In STM only two chains may be seen in fig. 4.2 (a). The chain with high $\times 2$ corrugation is identified as Si adatoms, while the neighboring rather structureless chain is the Si honeycomb step edge. The bandstructure detected by ARPES is shown in fig. 4.2 (c). Two parabolic bands are seen situated symmetrically around the Γ point. The band fillings are $S1 = 0.49$ and $S2 = 0.42$ [89]. The S1 band is clearly metallic at RT, while the S2 band is slightly recessed from the Fermi energy, see fig. 4.2 (d). Tight binding fits of the Fermi surface contour yield a ratio of the transfer integrals $\frac{t_{\parallel}}{t_{\perp}} > 60$ for both bands, thus rendering the states highly anisotropic [89].

Upon cooling a doubling of the step edge chain periodicity is found in STM, while the adatom chain remains unchanged [91], see fig. 4.2 (b). At the same time the S1 band is recessed from the Fermi energy, rendering the surface insulating [91], see fig. 4.2 (d). From STS measurements of the energy gap a mean field transition temperature could be calculated to $T_C = 260$ K [91]. Again these observations seem to coincide perfectly with the Peierls picture.

Later density functional theory (DFT) calculations by Riikonen *et al.* found that a buckling of the Si step edge atoms leads to the doubling of the periodicity [92, 93]. At the same time the buckling result in a gap between the filled and empty states. Consequently at low temperatures the amplitude of the buckling leads to a MIT for the S1 band. The S2 band is attributed to bonds between the Au and the Si adatoms, and is gaped at the zone boundary. The transition may be explained by vibration of the step edge atoms. At high temperatures the vibration reduces the gap size. However the proposed theoretical model predicts an asymmetric energy gap, which is not observed in experiments [94].

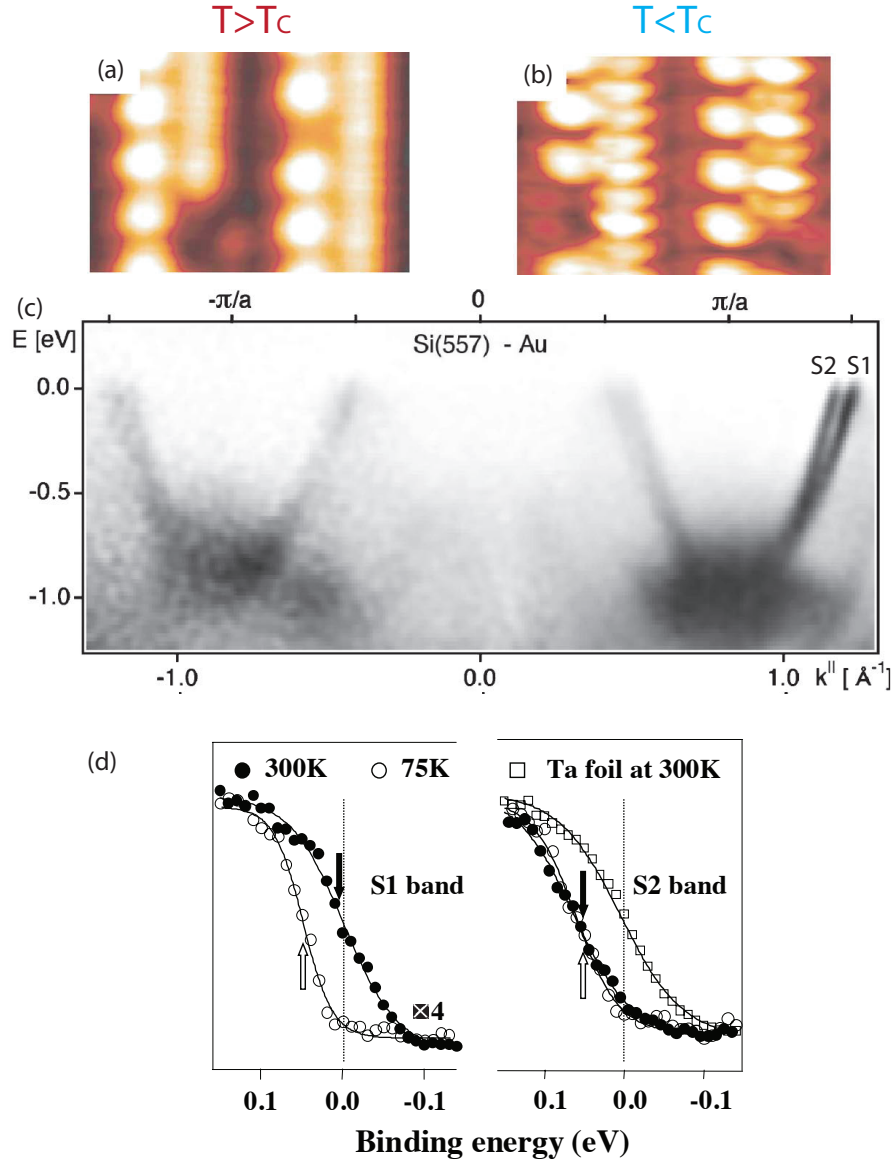


Figure 4.2: (a) STM image of the Au/Si(557) chains. The high corrugation chain is identified as Si adatoms, while the structureless chain comes from the Si step edge, from [91]. (b) Below the transition temperature the step edge chain period is doubled, from [91]. (c) ARPES at RT shows two metallic bands S1 and S2 almost half-filled [89]. (d) EDC analysis at the Fermi vectors of S1 and S2. At 300 K, S1 is clearly metallic, while S2 is gaped. Below the transition temperature both bands are insulating, from [91].

Furthermore it was shown by spin resolved ARPES measurements, that the S1 and S2 state originate from the same band and are spin-orbit split due to the Rashba effect [95]. This renders the band situation even more complicated, since the states S1 and S2 are completely spin polarized with opposing spins. Consequently the transition in the Au/Si(557) system is not completely settled and still under current debate. More input from theory is now needed to understand the phase transition and to incorporate the spin orbit split bands.

Finally it should be mentioned, that early ARPES studies on the Au/Si(557) chains have claimed the occurrence of a TLL [32]. These studies showed two dispersing features, which merged at the Fermi energy. This finding was interpreted as spinon and holon dispersion branches. At the same time no clear Fermi cutoff could be found in the spectra and a power-law behavior was claimed. However later studies with higher resolution completely disproved these findings [89]. The ARPES data in fig. 4.2 (b) clearly show, that the features at the Fermi energy are split and that a clear Fermi cutoff exists, see fig. 4.2 (d).

4.1.3 Au chains on Si(553)

In turning to the related surface Si(553) many similarities may be found. Here the surface is miscut by 12.3° towards the $[11\bar{2}]$ direction. The higher miscut angle leads to a reduced width of the terraces of 1.48 nm. The deposition of Au results in similar structure to that of Au/Si(557). Gold is substituted in the topmost surface layer, forming a zig-zag double chain, while at the step edge Si honeycomb chains are formed [96, 97]. But the adatom chain is not present here. In STM the structure is seen as two chains [33], see fig. 4.3 (a). Both chains show mostly a $\times 1$ period at RT, with only some parts showing a $\times 2$ periodicity. The high corrugation chain corresponds to the step edge. In ARPES similar to Au/Si(557) two parabolic bands S1 and S2 are detected, but additionally a third band S3 is found. The fillings correspond to $S1 = 0.51$, $S2 = 0.56$ and $S3 = 0.27$ [98], see fig. 4.3 (b).

A tight binding fit of the Fermi surface yields hopping ratios $\frac{t_{\parallel}}{t_{\perp}}$ of $S1 = 46$, $S2 = 39$ and $S3 = 12$. These are smaller than that of the Au/Si(557) chains, which may be explained by the reduced terrace size. This enhances the coupling between the chains [98]. In fact a systematic study of miscut Si(111) substrates showed, that the coupling between the chains increases with decreasing terrace size [89].

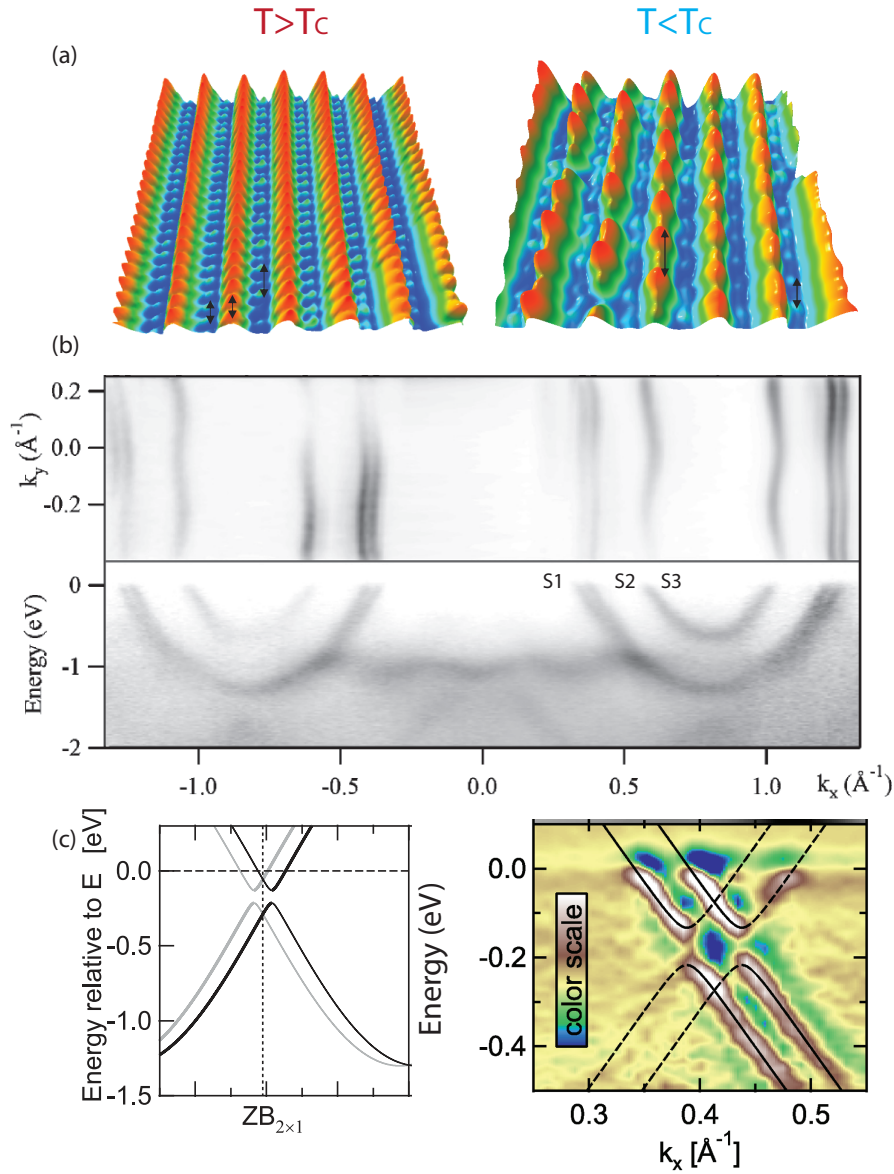


Figure 4.3: (a) STM images of the Au/Si(553) surface above (left) and below (right) the transition temperature, from [33]. Two chain types are visible with the strong corrugation (red color code) undergoing a $\times 3$ and the other a $\times 2$ transition upon cooling. (b) The corresponding band structure at room temperature. At the bottom the dispersing features are seen. Three bands are detected. Top: Fermi surface contour with marginal wiggling, from [98]. (c) Avoided band crossing pattern due to spin-orbit splitting. High resolution ARPES data showing avoided crossings at the zone boundary, thereby pointing at spin orbit split bands S1 and S2, from [99].

The low temperature structure of the surface observed with STM is shown in fig. 4.3 (a) left. While the honeycomb chain undergoes a $\times 3$ transition, the Au chain simultaneously is doubled in its periodicity [33]. The observations seem to coincide with a gapping of the S1 and S3 band [33]. These are close to $1/2$ and $1/3$ filling and thus the transition was interpreted as two simultaneous Peierls transitions. As in the case for Au/Si(557) the S2 band was found to be gapped at all temperatures, according to [33].

A similar mechanism to the step edge buckling as in the Au/Si(557) chains seems unlikely, since the period of the step edge is tripled. Yet there are also further evidences against a Peierls transition. High resolution ARPES studies of the S1 and S2 band have found, that they are both backfolded at the $\times 2$ zone boundary, see fig. 4.3 (c). Interestingly there is a pattern of avoided crossings and it was followed that the bands are spin orbit split [99]. Because two fermions cannot occupy the same state the crossing pattern opens, see fig. 4.3 (c). This would not be the case for unpolarized electron bands. Later calculations seem to corroborate this picture, where a spin polarization of every third electron at the honeycomb chains was proposed. [100]. Lastly spin resolved ARPES measurements performed in our group find the bands to be spin orbit split [manuscript in preparation]. Therefore again the simple Peierls picture cannot hold for this surface system and further calculations are needed to understand the transition occurring in this system.

To sum up the findings from these three nanowire systems:

- (i) All three chains undergo a symmetry breaking phase transition upon cooling.
- (ii) The electronic structure also changes and forms energy gaps for most bands.
- (iii) The earlier Peierls interpretation was challenged by calculations (hexagon formation, step edge buckling).
- (iv) At least in the Au chains on the stepped surfaces, spin-orbit interactions have to be taken into account.
- (v) In none of the systems could TLL behavior be shown, pointing to a finite electronic coupling between these chains.

- (vi) The need for better confined 1D nanowires at surfaces arises in order to find a model system for a 1D electron liquid. Consequently a different approach to their fabrication is needed.

4.2 The Ge(001) surface

A fundamentally different approach to the growth of nanowires for a 1D model system is the use of Ge(001) as a substrate. The nanowires growth is guided by the intrinsic Ge dimer rows. In this chapter first a general description on the Ge(001) surface will be given. Thereafter the newly developed cleaning procedure of the surface will be shown and compared to other existing mechanisms. Eventually the possible chain reconstructions will be discussed in the following chapter along with the new results on the Au/Ge(001) nanowires.

Germanium belongs to the group IV elements, like silicon and carbon. Although the first transistor was made from Ge, the technological development since then has strongly been focussed on Si. However in recent years more and more research has been done on Ge, because of the possibility to grow low-dimensional (low-D) nano structures by self organization.

Bulk germanium condenses in the diamond lattice, which may be described as two FCC lattices shifted by $1/4$ along the cube diagonal. Each atom has four nearest neighbors to which it is covalently bound. The 4s and 4p orbitals overlap and form sp^3 hybrid-states by linear combination of the original s and p wave functions. Since there are excellent detailed review articles on the reconstruction of the Ge(001) surface [101, 102] only a brief outline of the most important facts will be given.

When cutting the Ge crystal along a [001] direction, i.e. along one side of the cube, there will be two unsaturated orbitals (dangling bonds) per atom, reaching into the vacuum. Because this state is energetically unfavorable two neighboring germanium atoms will react and form a dimer. The result will then be the creation of dimer rows. Since it is not possible to polish the crystal perfectly flat, there will be terraces which are separated by an atomic step. Between each step the dimer rows will be rotated by 90° , but will all lie in parallel on one terrace. This is due to the A-B stacking of the substrate. Consequently the dimer rows will run along

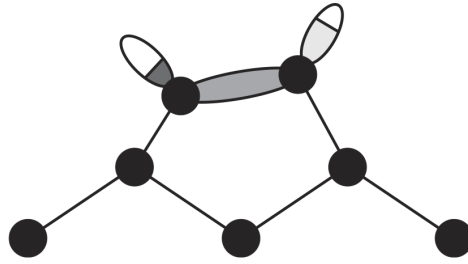


Figure 4.4: *Buckled Ge dimer at the reconstructed surface, from [101]. Dimers are bound by a σ -bond of two p orbitals. Two dangling bonds remain and reach out of the surface, forming a weak additional π -bond.*

the $[110]$ and $[\bar{1}10]$ directions. Therefore one will end up with two domains on a sample crystal.

By dimerization the total energy of the system is minimized. A further energy reduction is performed by a buckling of the dimer axis perpendicular to the sample surface, see fig. 4.4. Since left or right buckling configurations of the dimer are energetically degenerate, at RT the system rapidly switches at 10^8 - 10^{10} Hz between the two configurations [80], see fig. 4.5 left. Therefore the structure in STM will appear at the same height, with no detectable buckling. This leads to a (2×1) reconstruction of the surface. However towards low temperatures the vibration stops and the long range order of the system is described as alternating left and right buckled dimers, rendering a $c(4 \times 2)$ unit cell, see fig. 4.5 right. The latter may also be seen at RT in the vicinity of defects and on terrace steps, where the buckling is pinned [101].

4.3 Preparation of clean Ge(001) surfaces

The preparation of a clean and low-defect Ge(001) surface is a formidable task. Main difficulties are due to the oxide of Ge, which serves as a protection layer in ambient atmosphere. Unlike silicon, the GeO_2 layer

- (i) does not match the Ge lattice and therefore will strain and crack [103, 104].
- (ii) is solvable in water and will therefore be etched in ambient air humidity.

Constant etching and regrowth lead to an incorporation of contaminants into the oxide and also to the interface of Ge/GeO. Therefore in this thesis a cleaning

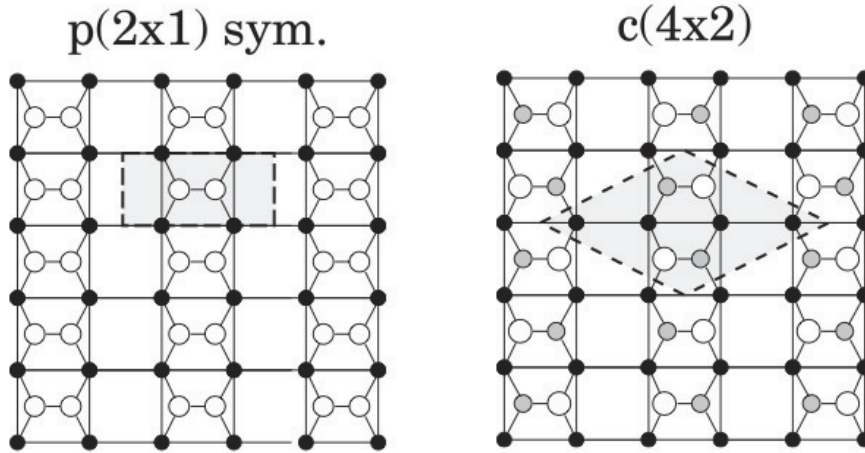


Figure 4.5: Left: $p(2\times 1)$ reconstruction of Ge(001). Topmost atoms are represented by white circles. The dimer rows run vertical. Right: low-temperature $c(4\times 2)$ phase with buckled dimer configuration. Alternating left right buckling leads to a larger unit cell, from [80, 101].

procedure has been developed, which is both reliable and fast, leading to a clean Ge(001) surface with reproducible results [A.9].

The cleaning process is divided in two steps. The *ex situ* preparation involves wet chemical etching and passivation by growth of a thermal oxide. Afterwards the samples are degassed and the oxide is eventually removed *in situ*. In short the recipe is:

- | | |
|---|-------------------------------|
| 1) Acetone bath in sonicator, 2 min | → removal of photoresist |
| 2) Triple organic baths, 2 min each | → removal of hydrocarbons |
| 3) Dry blow with nitrogen | → removal of solvents |
| 4) Piranha (7:2:1) etch, 5 sec | → removal of native oxide |
| 5) Water rinse, 1 min | → removal of acid |
| 6) Oven at 380 °C in high purity air, 5 min | → growth of protective oxide |
| 7) Heating in UHV at 250 °C, 6 hours | → removal of adsorbates |
| 8) Flash annealing in UHV to ~ 600 °C | → removal of protective oxide |

4.3.1 Piranha etching and thermal passivation

The *ex situ* sample preparation is conducted in a clean room environment, provided by a flow-box. Commercially available Ge crystals were used from a variety of different suppliers (CrysTec, MaTeck and Crystal). Resistivities due to different

doping level ranged from 0.04 Ωcm to 20 Ωcm . All crystals yielded similar results. The n-doped Ge(001) samples are ultrasonically cleaned in standard grade acetone, to remove a protective photoresist. Adsorbed hydrocarbons are subsequently removed by stirring the samples in ultra-pure acetone, propanol and methanol for 2 min each. Residual solvents are blown off with dry nitrogen. Afterwards the samples are dipped in piranha solution with $\text{H}_2\text{SO}_4:\text{H}_2\text{O}_2:\text{H}_2\text{O}$ (7:2:1) for 5 s. This step not only strips the native oxide but also etches several layers of the Ge surface. Furthermore piranha solution is very aggressive to remaining carbon and hydrocarbon contaminants. Due to self heating of the solution by hydration of the SO_4^{2-} anions in water, the etching process takes place at elevated temperatures ($T \sim 80^\circ\text{C}$). All chemicals are used in highest available purity. Since especially H_2O_2 may contain a marginal amount of organic impurities, it should be used in highest purity without stabilizers, and also in lowest effective concentration in the piranha solution. After etching, the samples are rinsed in deionized water for 1 min. The water was chosen in triple distilled purity (impurities ≤ 1 ppb) with a conductance below 2 $\mu\text{S}/\text{cm}$, since the surface after etching has no protective oxide and any impurity will react with it.

Thereafter, the samples are blown dry with nitrogen and placed in an oven at 380°C in a high purity synthetic air for 5 min, in order to produce a clean passivating oxide layer, which also buries residual contaminants. The elevated temperature is necessary to provide the activation energy for the oxidization [105]. Afterwards the samples are mounted onto the sample holder and eventually transferred into the UHV system.

4.3.2 Degassing and oxide removal

The sample-holder is degassed *in situ* for 6 h at 250°C , using direct current heating of the semiconductor substrate. This is highly important to remove physisorbed gas particles from the sample holder, since the dangling bonds of the free surface will quickly react after oxide removal. This may even lead to a complete destruction of the surface, if the vacuum conditions are not sufficient. A later removal of such reacted adsorbates is virtually impossible since especially carbon and germanium form a very strong bond (460 kJ/mol) which can only be broken at temperature higher than the melting point of Ge (263 kJ/mol) [106].

The oxide layer is removed by flash annealing for $t \sim 1$ sec to $T \sim 600^\circ\text{C}$. The short annealing time ensures that there is no unnecessary activation every for further reactions with contaminants after the oxide is removed. The oxide desorption follows the reaction [107]:



which in our case results in a total conversion of dioxide into the gaseous phase, so that the passivation layer can be completely removed in UHV. Thereafter the surface typically shows terrace diameters of about 100 nm with very low defects and carbon contamination is barely detectable.

4.3.3 Protective oxide quality

The formation of GeO_2 occurs via sub-oxides and only gradually leads to a closed oxide film, due to the lattice mismatch of 21 % and strain relaxation between Ge and GeO_2 [103, 104]. Angle dependent X-ray photoelectron spectroscopy (XPS) studies have been performed to judge the quality of the oxide layer, regarding thickness and homogeneity. Electrons escaping the sample normal to the surface have the highest probing depth, while shallow angles increase the surface sensitivity. By analyzing the oxide-shifted component of the Ge 3d core level, the thickness of the passivating oxide may thus be determined. For comparison a unprocessed (as bought) as well as an etched and thermally oxidized sample are scrutinized.

The resulting spectra for the thermally grown oxide layer is shown in fig. 4.6 (a). Starting with the highest probing depth ($\alpha = 0^\circ$), two peaks are detected from the Ge bulk (29.4 eV) as well as GeO_2 (32.4 eV). Since most signal stems from the bulk the Ge peak dominates the spectrum. When increasing the angle in steps of 10° , the surface sensitivity is enhanced, so that the GeO_2 signal increases at the expense of the bulk Ge signal.

The thickness of the oxide may be determined by thee analysis of the angular dependence of the spectra. This is done by comparison of the substrate intensity (I_{sub}) and GeO_2 intensity (I_{ox}) of the Ge 3d core level, according to [108, 109]

$$d_{ox} = \lambda_{ox} \ln \left(\frac{\rho_{sub} \lambda_{sub}}{\rho_{ox} \lambda_{ox}} \frac{I_{ox}}{I_{sub}} + 1 \right) \cos \alpha, \quad (4.2)$$

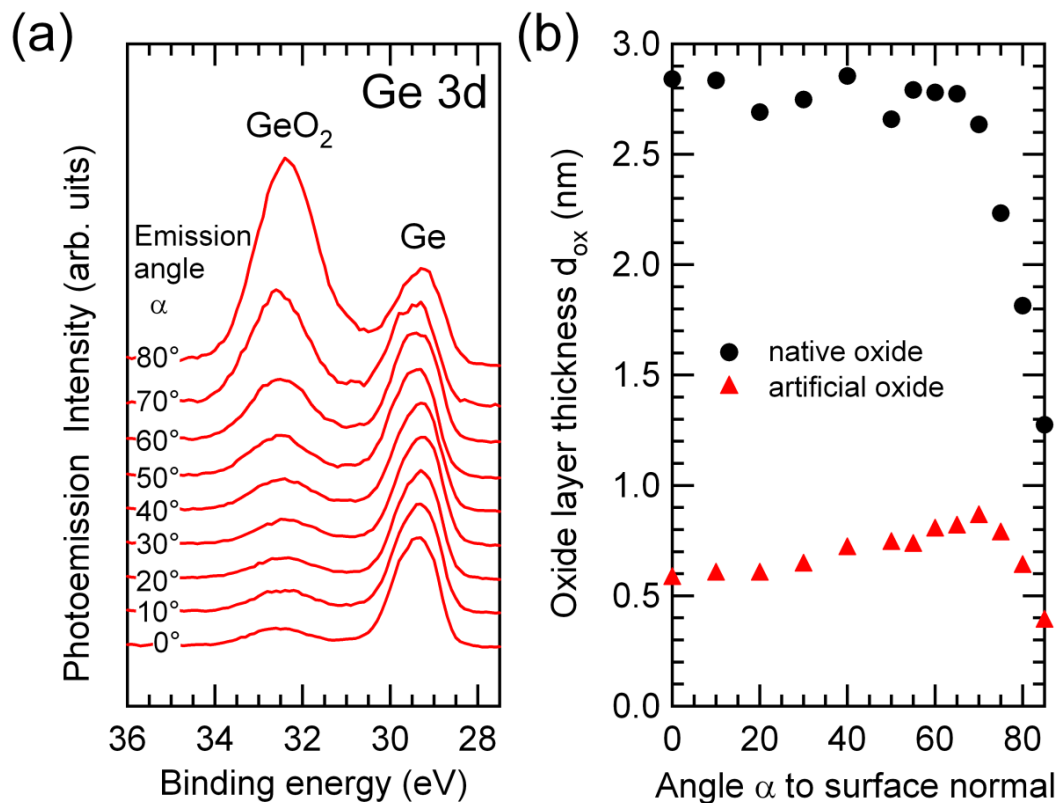


Figure 4.6: (a) Ge 3d core level spectra depending on the electron emission angle α to surface normal, starting from normal emission towards in-plane. All spectra are normalized to the Ge 3d bulk peak. (b) Reduced oxide layer thickness for thermally oxidized samples (red triangles) and the native oxide samples (black dots). For native oxide samples the oxide thickness amounts to 2.8 nm compared to the thermally grown oxide of only 0.6 nm. The intensity drop off at $\alpha = 70^\circ$ results from elastic scattering of the photoelectrons. From [A.9].

where ρ represents the atom densities. According to Tanuma, Powell and Penn [110] one may calculate the inelastic mean free path for the oxide $\lambda_{ox} = 2.89$ nm and the Ge substrate $\lambda_{sub} = 2.99$ nm. The calculated oxide thickness is plotted over the emission angle, see fig. 4.6 (b). The curve shows a constant thickness for $0 < \alpha < 60^\circ$, which indicates a homogeneous and smooth oxide layer. The drop-off at 70° is due to elastic scattering of the photoelectrons. Consequently one finds for the thermally grown oxide a thickness of 0.6 nm (~ 3 monolayer [104]) and 2.8 nm for the native oxide. The latter is four times larger than the artificial oxide, which is consistent with previous studies on the typical native oxide layer thickness [109, 111]. However a thin oxide is desired in order to completely remove it upon flash annealing the sample. Furthermore in the native oxide layer and its interface with the Ge(001) substrate, all sorts of impurities from the polishing process of the manufacturer will be contained.

The composition of the oxide may be judged from the chemical shift of about 3 eV in the upper Ge 3d core level of fig. 4.6 (a). One finds in good agreement with Molle *et al.* that it is only GeO₂, since the formation of GeO₂ is favored over GeO in the temperature growth regime below 400 °C [111].

In using atomic force microscopy (AFM) one may directly judge the surface roughness with the oxide on top, see fig. 4.7 (a). Roughness analysis of an area about $1 \mu\text{m}^2$ yields a root-mean-square value of approximately 0.28 nm, which compares well to the roughness of the free Ge(001) surface obtained from STM. This points at the growth of a homogeneous oxide layer with an overall constant thickness.

4.3.4 Surface quality after oxide removal

XPS may also be used to judge the surface cleanliness before and after the desorption of the thermally grown oxide. The initial oxygen contribution to the Ge 3d core level vanishes in the photoelectron spectra (lower panel fig. 4.7 (b)), leaving only the bulk signal. Furthermore the initial O 1s peak disappears completely, see fig. 4.7 (c), reflecting the overall removal of the oxide layer. Note that there is a small contribution of the Ge Auger L₂M₂₃M₂₃ peaks (534 eV and 525 eV) in the O 1s spectra [112].

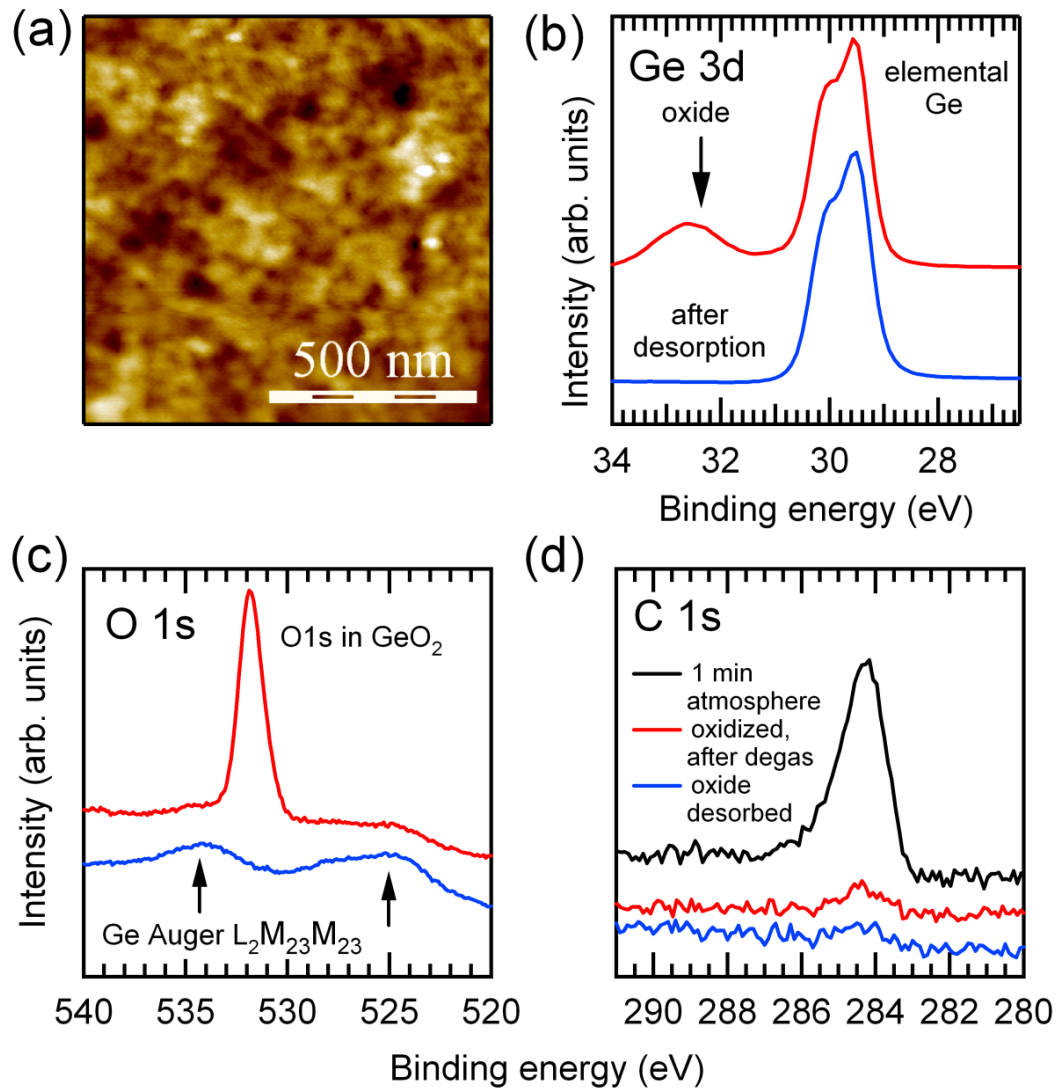


Figure 4.7: (a) AFM image of $1 \mu\text{m}^2$ for thermally grown GeO_2 with a root-mean-square roughness of 0.28 nm. Core-level spectra before (red, upper curve) and after (blue, lower curve) removal of thermally grown oxide. (b) Ge 3d, (c) O 1s and (d) C 1s. After desorption no traces of carbon or oxygen are detectable, pointing to a complete lift off of the oxide and a carbon free surface. From [A.9]

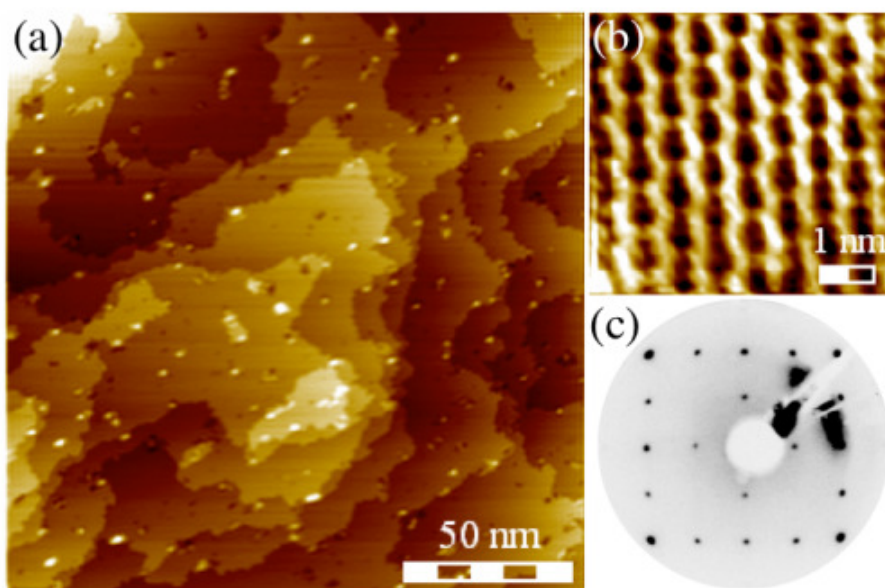


Figure 4.8: (a) STM overview image of the Ge(001) surface (+1.7 V, 0.5 nA, RT). Typical terrace widths are 50-100 nm. Few protrusions are visible. (b) Closeup STM image (+1.5 V, 0.5 nA, RT) of the defect-free $c(4 \times 2)$ reconstruction. (c) LEED pattern at 41 eV; sharp reflexes with low background demonstrate high sample quality. From [A.9]

The level of contaminations may be directly seen from the intensity of the C 1s core level. The oxide-desorbed surface in fig. 4.7(d) has almost no detectable C 1s signal compared to the oxidized sample. Thus remaining contaminations after etching are effectively buried upon oxidation and subsequently removed. For comparison, an actual carbon contribution on the oxide-removed substrate can be seen after exposure to atmosphere for 1 min in fig. 4.7 (d).

In order to judge the quality of the free surface STM has been performed to resolve the surface with atomic precision. An overview image shows regular flat terraces with a mean diameter of ~ 100 nm, fig. 4.8 (a). This distribution depends essentially on step pinning due to remaining defects, the surface roughness caused by polishing as well as the miscut of the crystal. Notably only few protrusions are detected and their density is very low compared to other chemical cleaning procedures or ion bombardment and annealing (IBA) [113–115]. These are most likely due to residual carbon contamination or dopant segregation to the surface. Yet both (C and Sb) are well below the detection limit in the XPS spectra. Since studies of undoped substrates show the same protrusions [113], it is likely that

they are due to carbon. Additional investigations on the annealing duration show the immobility of such protrusions so that no clustering can be observed, a fact which is also reported in Ref. [114]. In looking more closely, one may even resolve the intrinsic dimer rows, fig. 4.8 (b), which show both a regular (2×1) and the co-existing $c(4\times 2)$ surface reconstruction with low defect density.

In using LEED one may judge the surface long range order, averaged over a larger sample area. The diffraction pattern shows a sharp and low background (2×1) pattern in fig. 4.8 (c). The pattern was recorded at the minimum of the universal curve (41 eV), see chapter 3.3.1, in order to maximize surface sensitivity. Since the signal to background ratio is very high this points at a low defect and contamination density.

4.3.5 Comparison with alternate cleaning procedures

Ion bombardment and annealing

The standard method for cleaning a Ge(001) surface is the use of several cycles of Ar^+ bombardment with subsequent annealing IBA [113]. Yet the surface damage due to the ions may not be completely recovered and many cycles will lead to carbon protrusions, which hinder further self-organized growth on the surface [113, 114]. Also the time consumption of the method is rather high since each cycle requires ~ 60 min, and typically 5-7 cycles are needed. Furthermore the long and frequent annealing times lead to a high thermal budget in the sample, which can lead to dopant segregation at the surface. However by evaporation of a Ge buffer layer on top of the IBA treated surface, all damage may be recovered and a nearly perfect surface may be produced [113]. Yet this involves an additional and lengthy processing step in UHV, which is not possible to perform at all setups.

Etch and oxidization treatments

Usually chemical treatments of the Ge(001) surface involve an oxidizing agent like hydrogen-peroxide (H_2O_2) and subsequent removal of the oxide-layer in a second bath of HCl or HF [115–117]. The final passivation oxide is usually removed in UHV by annealing. It yields a surface similar to the IBA treatment, with a comparable protrusion density, yet carbon is not always removed effectively [113]. This may

be due to a poor oxide layer quality since passivating Ge(001) with GeO₂ in liquid oxidizers (H₂O₂/H₂O, NH₄OH/H₂O₂/H₂O or HNO₃) [116, 117] is inefficient. This is due to the fact that GeO₂ is water soluble, so constant etching and reformation of the oxide will occur in aqueous solutions [115, 117]. Also these chemical procedures always leave detectable amounts of carbon residue at the surface [113–115], which are caused either by an insufficient etching process or an incomplete oxide layer. However, residual carbon and oxygen on the surface hinder surface mobility and the development of larger terraces [113, 114]. So a complete removal is paramount.

In order to avoid the oxidation in a liquid, alternative methods have tried to perform this step by UV/ozone treatment [115] or *in situ* oxidation with molecular oxygen [118]. Both procedures effectively remove most carbon contaminations but add an additional and complex processing step. Also the UV/ozone treatment results vary with conditions of the lab [114].

Besides its cleaning efficiency, our proposed method does not require special safety equipment, since only relatively harmless substances are used. This is unlike, e.g., HF or UV/ozone, where special precautions have to be fulfilled. Thus the piranha etching and thermal oxidization treatment is fast, simple and reproducible, resulting in a clean and long-range ordered surface.

5 Structural elements of Au/Ge(001) nanowires

5.1 Current knowledge about nanowires on Ge(001)

Ge(001) has become a well suited substrate to guide the growth of self organized nanowires. Studies of noble metal growth on this substrate have recently been frequent publications in the literature. Ag and Pd form 2D reconstructions and lead to the formation of germanide clusters [119, 120]. Where as Au and Pt will reconstruct in 1D nanowires. The following chapter will give a brief introduction on these two chain systems. For a recent review see [A.3]

Pt nanowires on Ge(001)

Historically the Pt chains have attracted more attention, since they grow very well by cold deposition and subsequent annealing [121, 122]. Depending on the tunneling setpoint dimers along (fig. 5.1 (a)) or perpendicular to the chain direction are observed in STM [123]. The Pt wires are spaced at 16 Å, which is four times the lattice constant of Ge. Consequently the symmetry of the surface is described by a p(4×2) unit cell. It is also possible to image the wires down to 50 meV tunneling bias, thus pointing at a metallic character of the wire reconstruction. However, it was observed with STS that the signal at the Fermi energy is vanishing and therefore the chains are not very well suited for the study of conduction properties of 1D chains, see fig. 5.1 (b). This was later corroborated by DFT [124, 125]. These calculations also yielded a structural model, the so-called tetramer-dimer-chain-model, consisting of Ge-dimers in chain direction, see 5.1 (c). The conduction path is formed by alternating Pt-Ge building blocks in chain direction.

This model could reproduce the obtained STM images, as well as the tunneling spectra [124, 125]. The temperature broadened DOS from DFT qualitatively matches the experimental tunneling spectrum. The chains are thus characterized as a zero-gap semi metal. As the Ge surface is only scarcely covered with Pt chains, no ARPES data exists to assess the band-structure. Efforts with deposition onto the heated Ge substrate could improve the coverage up to 50 %. However, the sample quality was not sufficient for ARPES studies in recent experiments [A.3].

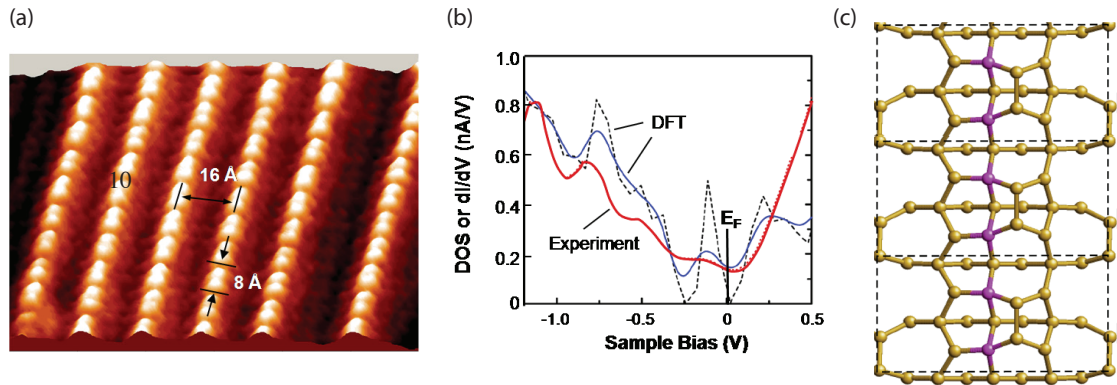


Figure 5.1: (a) STM image of the Pt/Ge(001) surface. Regular chains with 16 Å spacing are detected at -1.4V. Along the chains dimerized structures are visible. (b) Tunneling spectroscopy shows marginal conductance at E_F with good agreement from DFT calculations. (c) Tetramer-dimer-chain-model with Ge atoms in yellow and Pt in pink. The conduction path is built by alternating Pt and Ge atoms. From [A.3].

Au nanowires on Ge(001)

Up to the beginning of this thesis only two publications existed on the Au reconstruction on Ge(001). First adsorption studies had been performed by Wang *et al.* [37, 38]. The authors examined the surface regarding the Au coverage and annealing temperature after deposition. The optimum recipe was 1.5 monolayer (ML) of Au deposited at 675 K. Then the surface structure was found to completely reconstruct in wire form, see fig. 5.2 (a). These chains consisted of two rows, bright and dark as seen in the STM images. Note, that the wires are intercepted by vacancy defects. The wire length is determined from STM images to about 5-7 nm, while the spacing of the chains is 16 Å. The depicted long range order is $p(4 \times 2)$ with local $c(8 \times 2)$ segments. However this claim was not documented with a LEED pattern and based on STM observations. From these a ball-and-stick model was

proposed for the wire structure, see fig. 5.2 (b). The bright lines were identified as Au-Au dimers, while the dark lines were proposed to be Au-Ge heterodimers. A higher DOS of Au at the chemical potential explained the contrast detected in STM between the two types of rows. Also in the images a slight zig-zag is seen in the chains. It was interpreted as a buckling of the dimers and included in the model.

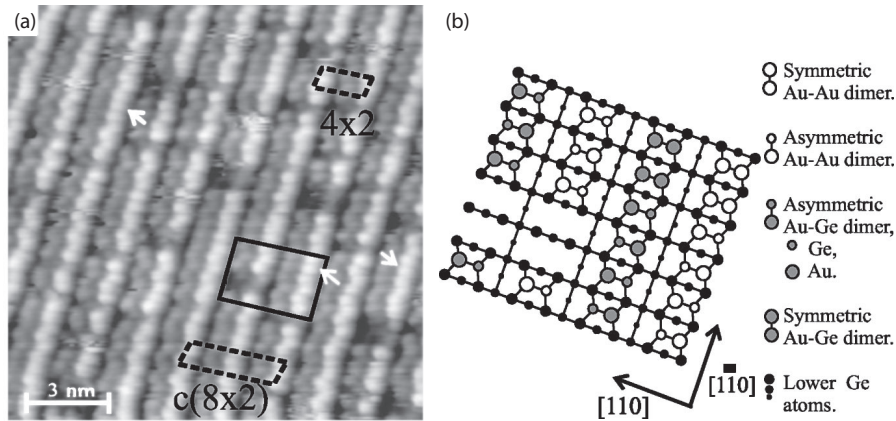


Figure 5.2: First Au adsorption studies on Ge(001) by Wang *et al.* (a) STM image of the Au reconstructed Ge(001)-surface. The authors found two types of wires, bright and dark in the image. The long range order was found to be (4×2) with local $c(8 \times 2)$ segments. The solid black box indicates the area for the structural model. (b) The bright wires are identified as Au dimers, while the lower contrast wires were interpreted as Au-Ge dimers, according to a simple ball and stick model. From [37].

These first studies proved, that the growth of Au nanowires on the Ge(001) surface is feasible. Yet the system has not been fully characterized and consequently some open questions remained:

- (i) What is the true long range order?
- (ii) What is the local structural description?
- (iii) What is the structural model?
- (iv) What are the electronic properties?
- (v) Does a Peierls Instability or exotic TL physics play a role?

These open questions were the trigger for this thesis.

5.2 Growth regimes and phase diagram of Au/Ge(001)

In order to optimize the nanowire growth conditions own studies have been performed. They were focussed on the Au coverage as well as the substrate temperature. After the clean Ge surface is prepared according to the recipe described in chapter 4.3, Au was evaporated onto the surface via an electron beam evaporator. During deposition the substrate was heated in order to ensure the mobility of the Au atoms on the surface.

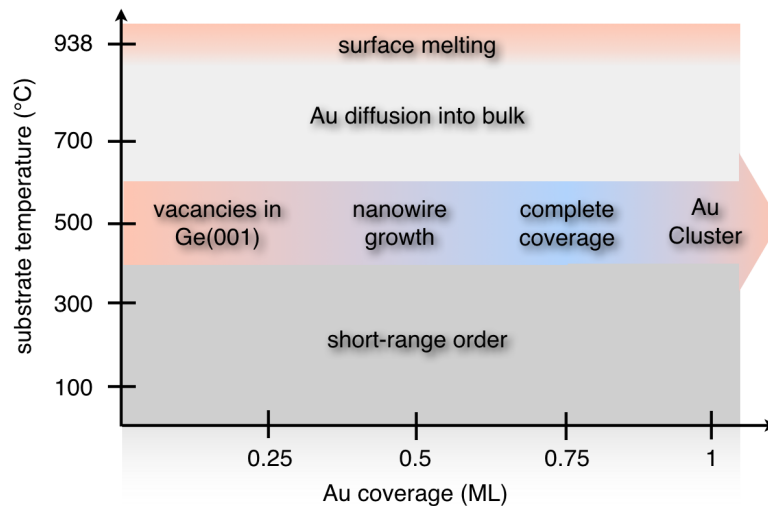


Figure 5.3: Schematic phase diagram for Au on Ge(001). At low substrate temperature only short-range ordered nanowires grow. Around 500 °C the growth of long-range ordered nanowires occurs, with the optimum at 0.75 ML coverage. These parameters lead to a complete coverage of the surface with nanowires. At higher coverages Au cluster will grow additionally on top of the chains. Towards higher temperatures Au diffuses into the Ge bulk and leaves a disordered surface behind.

Only a narrow parameter window of substrate temperature and Au coverage will result in the desired long-range ordered nanowires, see phase diagram fig. 5.3. The exact determination of the Au amount is very challenging, since e.g. a quartz crystal thickness monitor has to be carefully calibrated in order to make precise statements. This was achieved by Gallagher *et al.* by using the LEED signal of the Au/Si(111) (5×2) reconstruction, where the Au coverage is well-known [126]. The optimal Au coverage for the nanowire reconstruction was found to be 0.75 ± 0.05 ML of Au.

Here 1 ML is 4 gold atoms per 4 Ge atoms in the unit cell. Notably this is only half the coverage as that stated in the studies of Wang *et al.* [37].

In this thesis the optimal substrate temperature during deposition was identified to be 500 °C. Although further experiments have shown, that cold deposition with subsequent annealing yields the same chain reconstruction [127]. However, the long-range order is much improved by using a preheated substrate. At lower temperatures only short-range ordered structures will form [37, 38]. Whereas at higher temperatures the Au will diffuse into the Ge bulk, leading to a disordered surface. At the optimal temperature two other phases occur with different Au coverages: Vacancies and Au clusters. Closer inspection of these two phases allows the study of the growth mode of the Au/Ge(001) nanowires.

Vacancies (low Au coverage)

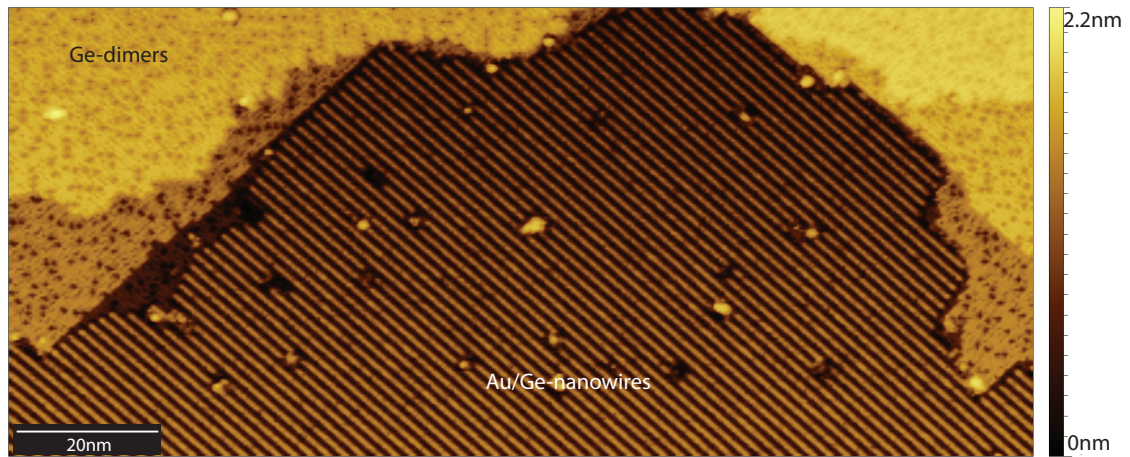


Figure 5.4: STM overview image at 77 K of the Ge(001) surface, deposited with Au. The lower terrace is completely covered with parallel Au chains. Neighboring terraces do not show nanowires, but many vacancies (black dots). This hints at an intermixing and diffusion of Au into the Ge substrate.

Fig. 5.4 is representing a STM image of a sample grown below the optimum coverage of 0.75 ML Au. The lower terrace is completely covered with nanowires. All lie in parallel with the identical spacing of 16 Å. Also on this terrace some protrusions are visible, which can be interpreted contaminations or excess Au atoms. Yet, their density is very low and the wire length is not ultimately limited by these defects.

Neighboring terraces, on the top left and right of fig. 5.4, are not covered with nanowires. The dimer rows of the free Ge(001) surface are still visible, and 90° rotated to the row direction between an atomic terrace step. However, the dimers are interrupted by many vacancy defects, represented as dim dots. These defects have no long-range order and are most likely due to a diffusion of Au atoms into the Ge bulk. Such processes leave a vacancy in the surface. Similar observations have been made for Pt and Pd on Ge(001) [120, 122]. There the noble metal adsorbates also diffuse into the substrate bulk. Upon a critical coverage of noble metal atoms, these reemerge and the surface reconstructs. A similar mechanism may also be involved in the present system. However, a significant difference between Pt and Au growth is that Au chains always cover a complete terrace, while Pt forms isolated chains [121, 122].

Consequently the growth mode of the Au chains may be concluded as follows. First the surface is intermixed with Au, see phase diagram, fig. 5.3 along the arrow of optimum temperature. The density of Au-induced Ge vacancies increases until the critical coverage is reached. It is limited by the bulk solubility of Au in Ge, 1.36×10^{-15} [128]. Yet this would result in a coverage of 50 ML onto a $500 \mu\text{m}$ sample, which is clearly not reached during evaporation [A.1]. This suggests that Au is only incorporated in the topmost layers of the substrate. After substrate is saturated with Au complete terraces will be converted to the nanowire reconstruction. Meanwhile still at neighboring terraces the dimer rows with vacancies exist. Apparently the interface between the nanowires and the dimer rows is energetically unfavorable and therefore avoided.

One may speculate, if the terraces covered with nanowires grow at the expense of the surrounding terraces [126]. Upon evaporation of Au the mean terrace size increases dramatically compared to the free Ge(001) surface. This has been described as a *surfactant effect* [129, 130] and leads to a lowering of the potential barrier for movement of the Ge atoms at the surface. The structure of the Au/Ge(001) chains is rather complex and a severe rearrangement of the surface atoms seems likely, as will be discussed in the following chapters. The surfactant effect is also observed in the Pt/Ge(001) system, where the terrace size is even larger than for Au [122]. Yet, complete coverage of the surface with Pt chains has not been reported so far.

Au cluster growth (high Au coverage)

In the high Au coverage regime, clusters will eventually grow on top of the nanowire reconstruction. Fig. 5.5 shows facets of these clusters. Their height varies from 10 to 100 nm, depending on the substrate temperature upon exposition and Au coverage.

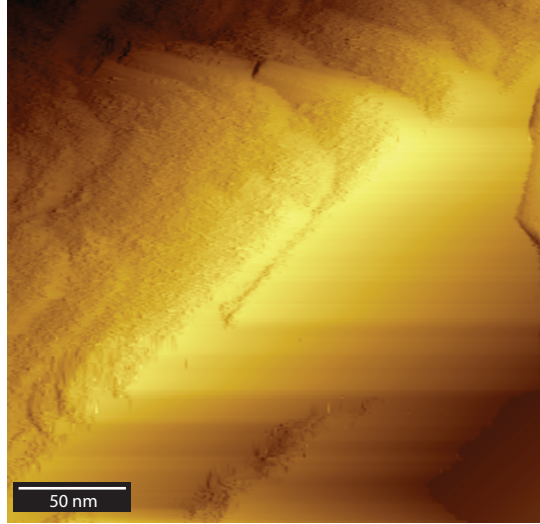


Figure 5.5: Overview STM image $250 \times 250 \text{ nm}^2$ of a gold cluster at high surface coverage. $T = 4.7 \text{ K}$.

A closer inspection of the clusters allows to resolve the structure on their top. Fig. 5.6 (a) shows an atomic resolution STM image of the cluster surface. Parallel rows are resolved, which lie at a distance of 8.7 \AA . As expected at these tunneling conditions no atoms are observed along the rows [131]. The periodicity corresponds to that of the Au(110) (2×1) missing row reconstruction [132], with lattice constants of 4.08 \AA and 2.88 \AA . A close match of the structure can be achieved to the Ge lattice constant of 3.99 \AA in one direction. This may explain the deviation between the ideal 8.2 \AA and the observed 8.7 \AA of the row spacing. There is potentially some lattice strain involved in the growth of the Au facets.

The (2×1) reconstruction is observed for deposition of Au onto the cold substrate only, while heating leads to a (1×1) reconstruction [38]. This counter-intuitive finding may be explained by Ge intermixing into the cluster at higher temperatures, since the solubility of Ge in Au is as high as 3 % for bulk materials [38]. The incorporation of Ge will then induce a straining of the crystal lattice and result in

a different surface reconstruction. This is a further indication for mass transport taking place at the surface at elevated temperatures during growth.

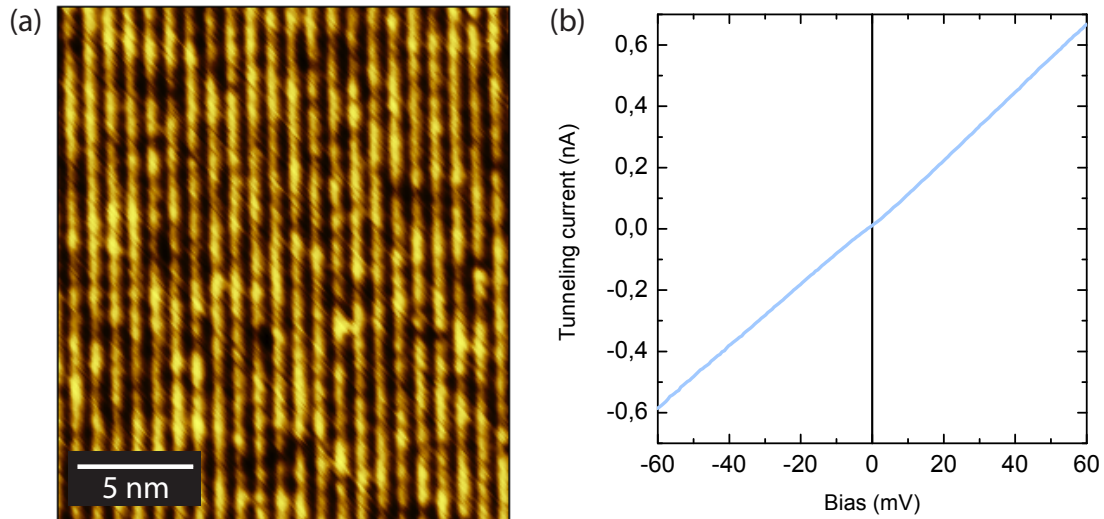


Figure 5.6: (a) Surface of Au cluster on top of the nanowires. Rows are identified at 8.7 Å distance, matching the (2×1) reconstruction of the Au(110) surface. (-1 V, 0.5 nA, 4.7 K) (b) Spectroscopy average over 160 spectra shows finite slope of the $I(V)$ -curves at the Fermi energy of the Au clusters. This proves the metallic character of the Au cluster and more importantly a good contact situation between the Ge substrate and the external contacts even at the lowest accessible temperature.

Spectroscopic studies on the cluster surface clearly show metallic behavior, see fig. 5.6 (b). The $I(V)$ spectra average over 160 equivalent locations has a finite slope at the Fermi energy (zero bias). Most notably the spectroscopy has been performed at 4.7 K on a semiconducting Ge-substrate. A metallic behavior of the cluster leads to the conclusion, that the substrate is still a good conductor even at these low temperatures. Moreover no contact effects like a Schottky barrier occur. This is very important for the spectroscopic studies of the nanowires, since a poorly conducting or insulating substrate would have an undesired effect on the tunneling experiment. This would result in charging of the wires or coulomb blockade effects and the electronic properties of the chains themselves could no longer be studied. However the metallic character of the Au clusters serves as a direct reference for a good contact situation. The tunneling spectra of the nanowires will be discussed in chapter 6.3.

Growth of nanowires (ideal Au coverage)

Upon deposition of 0.75 ML of Au at 500 °C the whole surface will be covered with the Au/Ge(001) chain reconstruction, fig. 5.7. There are two domains at the surface as guided by the substrate A-B stacking sequence, see chapter 4.2. Between single atomic steps the wire direction is rotated by 90°. On each terrace all wires lie in parallel at a distance of 16 Å. The overall defect density is very low. Only occasionally protrusions are visible on top of the chains. The wire length is ultimately limited by atomic vacancies, which are visible as black lines in the wires. However the individual chain length may easily reach 100 nm or more. Already at this scale it is apparent, that the wires are well separated by deep trenches and that no cross bonds exist between them. Only a weak corrugation is detected on the wire top, so that the charge is almost equally delocalized in chain direction. Yet, upon close inspection a weak and complex structure may be detected, which will be described further in the following chapter.

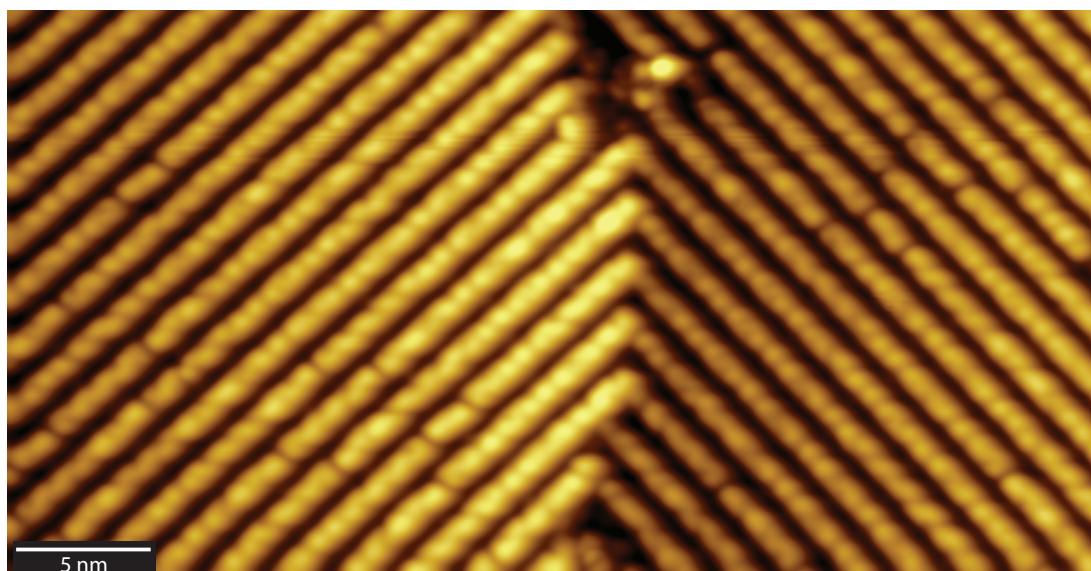


Figure 5.7: Dual domain STM image of the Au/Ge(001) surface at optimum Au coverage. Wires of the two domains are orthogonal to each other. (+1.2 V 0.3 nA, 4.7 K).

5.3 Chain architecture description

5.3.1 Structural elements

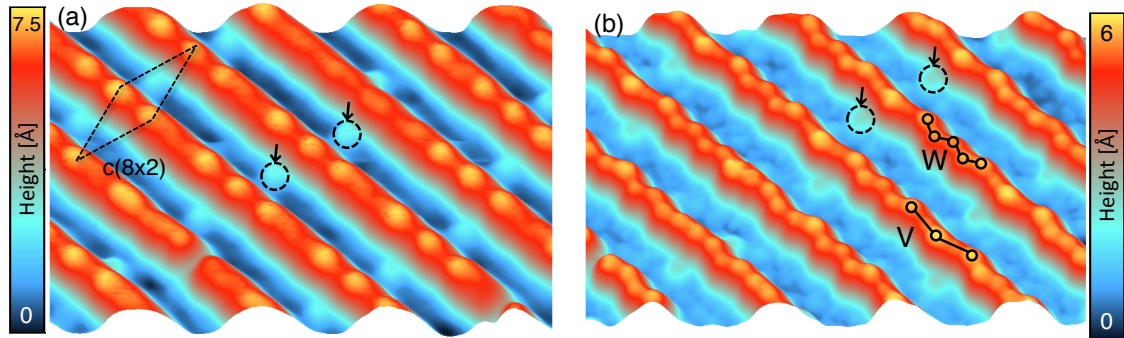


Figure 5.8: (a) Unoccupied states STM image (+0.8 V, 0.4 nA, 10 nm \times 6 nm, 77 K). Triplets of charge clouds are visible. Arrows highlight small protrusions between the nanowires. The unit cell is indicated by a dashed line. (b) Occupied states STM image (-0.8 V, 0.4 nA, 10 nm \times 6 nm, 77 K). A zig-zag-shaped structure appears between the triplet sites. The long-range order is built by V- and W-shaped segments. [A.9]

The ground state phase of the nanowire structure is scrutinized by STM at 77 K and shown in fig. 5.8. In the unoccupied states image, fig. 5.8 (a), the 16 Å wide spacing of the chains with deep grooves in between becomes apparent. On the wire top individual charge clouds are visible every 8 Å in chain direction. The structure may be described in a $c(8 \times 2)$ reconstruction. This is the basic symmetry of the surface and may be detected for most tunneling conditions. However, upon close inspection an additional superstructure is resolved. The symmetry in chain direction is fourfold due to the formation of *triplets* on the chain top. This results in a 32 Å periodicity of the superstructure along the chains.

When imaging the occupied states, the structure changes dramatically, fig. 5.8 (b). Now the wires appear even thinner. The long-range order may be described by alternating V and W zig-zag segments. Again this structure follows a 32 Å periodicity. In addition, protrusions are visible between the chains in both images, indicated with arrows. These protrusions are always closer to one ridge and never in the middle of the trough. Also these protrusions share the 32 Å superstructure periodicity.

Considering the alignment of triplets and the zig-zag pattern, the identical sample surface is studied in fig 5.9. When comparing the two states the triplets of the

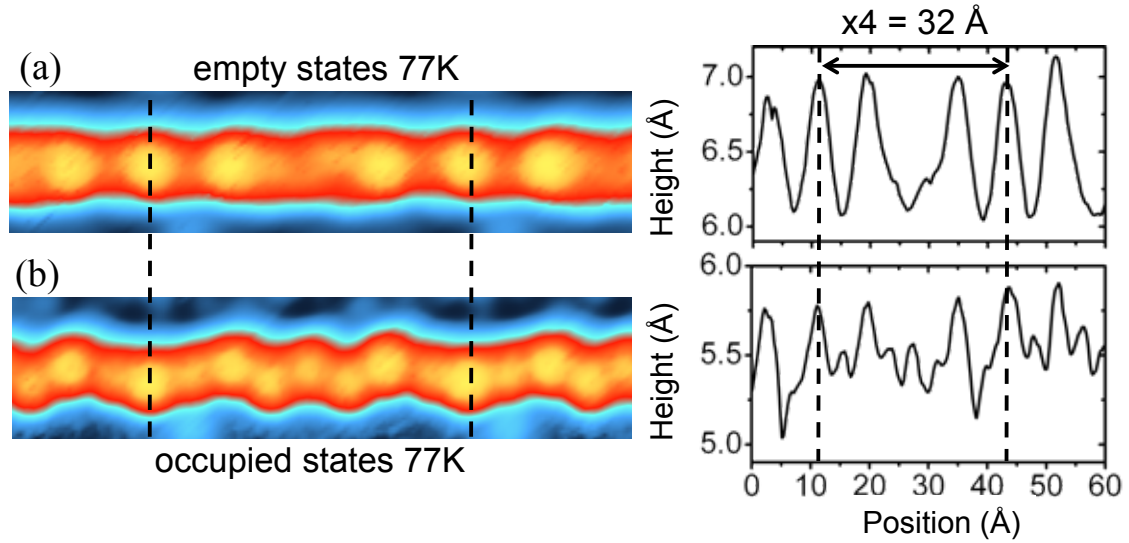


Figure 5.9: (a) Unoccupied states at (+0.8 V, 77 K), and corresponding line profile. (b) Occupied states at (-0.8 V, 77 K) of identical sample location. A zig-zag structure appears between triplet sites. The long-range order contains V- and W-shaped segments. From [A.9].

unoccupied states correspond to the V shape of the zig-zag. The W structure lies exactly in between two triplets. This is a very nice example for the capability of STM to detect electronic states, rather than true topography of the surface. Both images are taken at rather high bias conditions of ± 0.8 V, so that energetically deeper lying electronic states will be detected. Thus triplets and V-W will depend on the back bonding structure of the chains rather than on the conduction electrons. The zig-zag is rather sharp and well confined. Thus one may speculate whether these states originate from the Ge 4p orbitals, while the broader spherical charge clouds in the empty states correspond to the Au 6s wave function. However detailed conclusions may only be based on DFT calculations, which will be discussed in chapter 5.8.

5.3.2 Long-range order

The superstructure on top of the $c(8 \times 2)$ basic structure also has a weak lateral coupling. The triplets show a lateral correlation and a shift of 4 Å, e.g. in *up* direction, see fig. 5.10 for the left four wires. Most remarkable a *down*-shift is observed with equal probability, right three wires. A given interchain phase correlation (up

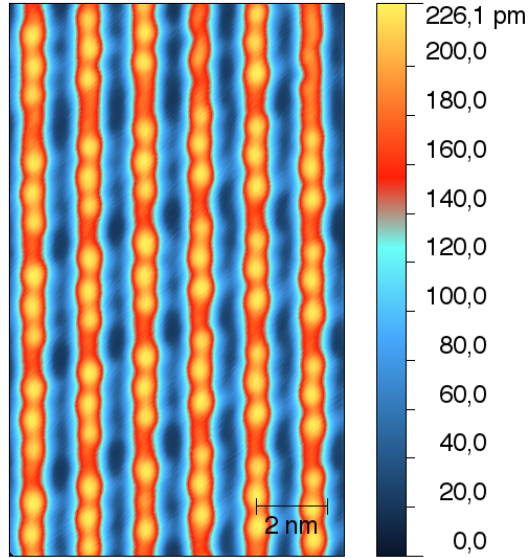


Figure 5.10: STM image of the nanowires at (+ 1 V, 1 nA, 4.7 K). Triplets are visible along the chains, with specific alignment with respect to the neighboring chains, described by the in matrix.

or down) persists typically over five to seven wires until the direction changes, suggesting that both alignments are energetically equivalent. This superstructure may be described by a superstructure matrix

$$\vec{M} = \begin{pmatrix} 0 & -8 \\ 4 & 1 \end{pmatrix} \quad (5.1)$$

Since the spacing of the chains is very large, the lateral order already points at a weak coupling of the wire structure via the substrate. Yet again, these conclusions are only for the deeper bound states and do not necessarily have to be applicable to the conduction electrons, which may as well be decoupled from the structure.

5.3.3 Bias series

In using the ability of STM to detect different electronic states, depending on the applied bias (chapter 3.1.2), the Au/Ge(001) chains have been scrutinized over a wide energy window of ± 1.6 V. All images were subsequently taken on the same sample surface. The deeper bound states are shown in fig. 5.11. In the unoccupied states images the characteristic triplet structure is visible. Yet, while the triplets

seem symmetric for the two high bias settings, starting from 1.2 V it becomes apparent, that the outer charge clouds of the triplets are somehow connected to the neighboring outer triplet cloud. On the other hand, the center of the triplet appears to be separated from the other two charge clouds. This impression becomes stronger with decreasing bias. Furthermore, in all unoccupied states images the protrusions between the chains are well resolved as white dots on the blue background. These do not move over time and occupy a fixed position close to a triplet. It is noteworthy that the protrusions are not located at a triplet center, but always between two charge clouds of the triplet. Also as stated above, the protrusions are always closer to one wire and not located in the middle of the trough. Since there seems to be only weak long range order of the protrusions with respect to its position at the triplet, four degenerate positions are observed: Top/bottom of the chain and left/right of the triplet. This may be seen in the bottom row of protrusions in fig. 5.11. The left protrusion is placed at the left position of the triplet, while its two neighbors occupy the right location. Also in the 1.6 V - 1.0 V images additional structures are resolved *between* the protrusions at a distance of 8 Å in chain direction. These structures might be due to gold dimers that build the trough region, see chapter 5.8.

Images of the occupied states do not change drastically over the range from -1.6 V to -0.7 V. In all images the characteristic V and W alternating segments are detected. This is due to the leading edge effect in tunneling probability, see chapter 3.1.2, which will enhance the sensitivity to states at and just below the Fermi energy of the sample. Notably the V shape is asymmetric with respect to the chain direction and all V segments in fig. 5.11 point downward. Yet, the upward pointing version is also equally observed, leading to the conclusion of two energetically equivalent configurations. Typically though along one wire the orientation does not change over several 10 unit cells. Additionally protrusions are observed in the grooves at all negative bias settings in fig. 5.11. Note that these protrusions are always closer the side of the wire where the V points.

The low energy states of the Au/Ge(001) chains are depicted in fig. 5.12. The unoccupied states at 0.6 V to 0.4 V still show a weak triplet structure. Yet, the center charge cloud is further enhanced, while the outer ones are more and more smeared out to continuous segments. The most dramatic change is seen in the lowest bias images 0.2 V and 0.1 V. Here, the center charge cloud of the triplet

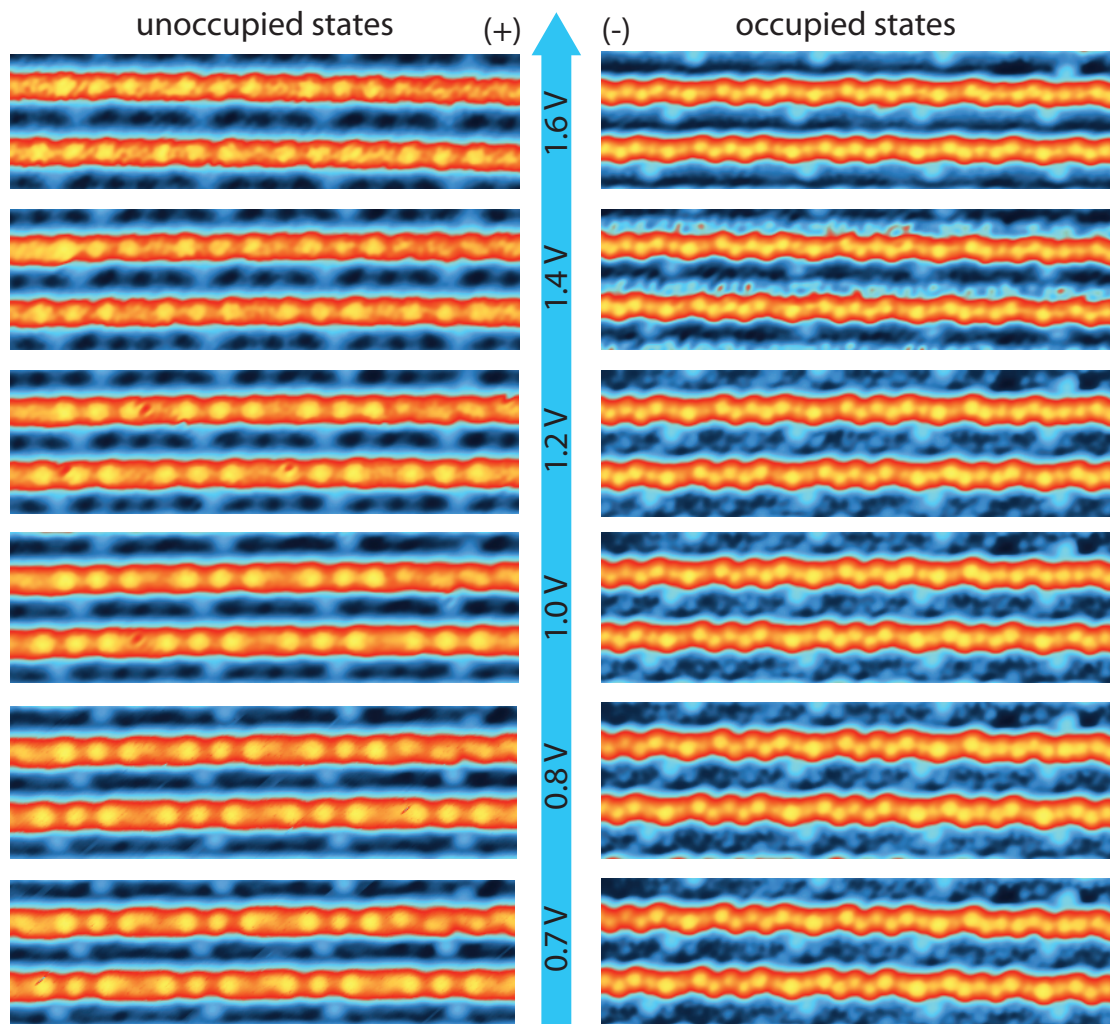


Figure 5.11: High energy bias series of the identical sample surface of $100 \text{ \AA} \times 26.3 \text{ \AA}$ at 77 K. All states show the fourfold superstructure on top of the basic $c(8 \times 2)$ symmetry. In addition protrusions between the chains are visible at a distance of 32 \AA matching the superstructure. Unoccupied states show triplets in chain direction, while occupied states appear as alternating V and W segments.

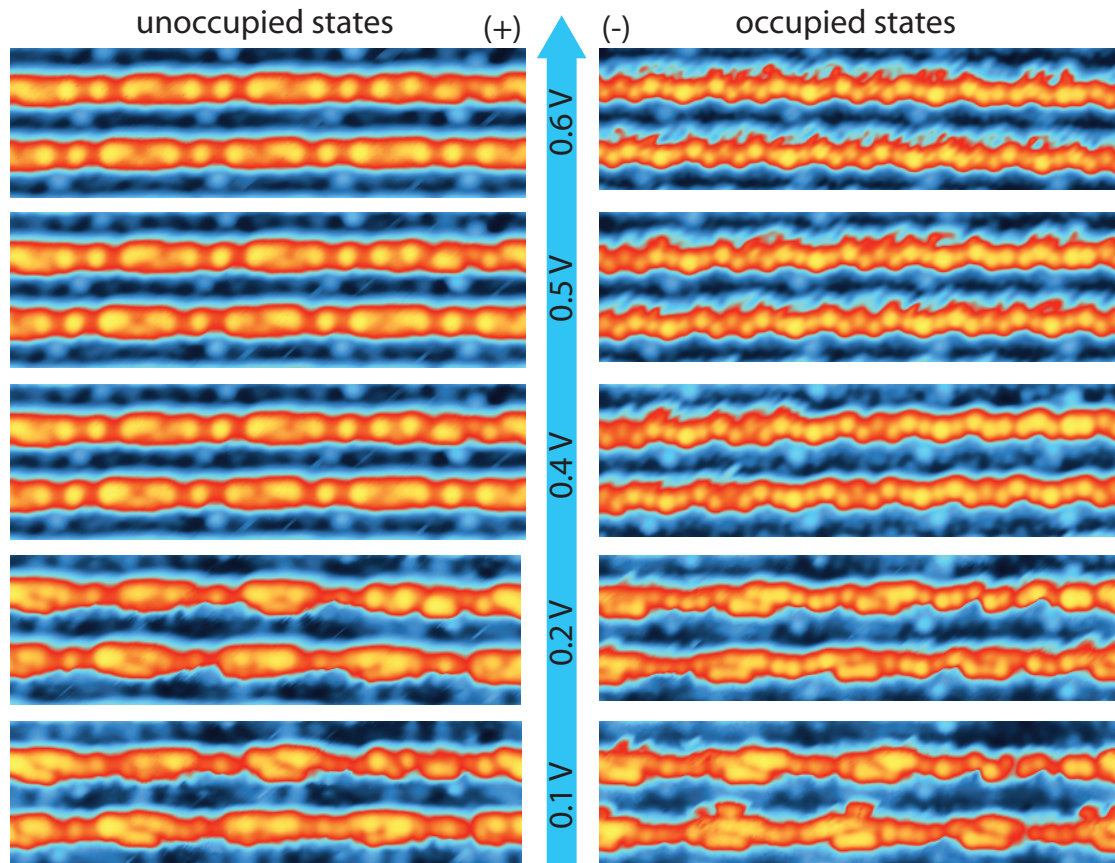


Figure 5.12: Low energy bias series of the identical sample surface, also as in fig. 5.11. $100 \text{ \AA} \times 26.3 \text{ \AA}$, 77 K. States close to the Fermi energy $\pm 0.1\text{-}0.2 \text{ V}$ show a dramatically different structure, due to the dominance of the 1D band in this tunneling window. Yet all images show the (4×1) superstructure symmetry.

fades away, while the structures in between are broadened. In addition nodes of charge are detected *perpendicular* to the chain direction for some of the connecting segments.

In the occupied states at -0.6 V to -0.4 V again the characteristic V-W structure is observed with no visible changes between the images. Most notably at -0.2 V and -0.1 V the W segment broadens and subsequently turns into the structure which was detected in the unoccupied states. Perpendicular nodes in the charge distribution are also detected.

In both states and at every bias the protrusions in the troughs are visible, leading to the conclusion, that these are due to real topography rather than electronic effects. On the other hand, the dramatic change of the wire structure can only be explained by the contribution of different wave functions. Especially the change at ± 0.2 V can only be explained by effects of the surface band structure, which lies in the vicinity of the Fermi energy, see sketch of the band situation in fig. 5.13 [A.6]. A detailed analysis of the band structure will be performed in chapter 6.1, but for the current discussion of the tunneling images a sketch is more than sufficient. The band bottom of the 1D band lies at ~ 150 mV in the occupied states. Apart from a hole-like band at the Γ point this is the only band crossing the Fermi energy and will therefore make a dramatic contribution to the tunneling signal and thus the detected structure in STM. It should be considered, that the tunneling probability depends on the electron momentum in the surface plane and highest at the center of the brillouin zone [70], according to eq. 3.5. Yet, the 1D electron band is situated at $k_{\parallel} = \pm 0.2 \text{ \AA}^{-1}$. Computing this expression with typical tunneling parameters (tip-sample distance of 8 \AA and a work function of 4 eV) this results in a reduction of the tunneling probability by only 35%.

$$I_T \propto \sum_{\nu} |\Psi_{\nu}(\vec{x})|^2 \quad \text{with} \quad \Psi_{\nu} = \Omega_s^{-\frac{1}{2}} \sum_{\vec{G}} a_G e^{\left[-(\kappa^2 + |\vec{k}_{\parallel} + \vec{G}|^2)^{\frac{1}{2}} z \right]} \times e^{i(\vec{k}_{\parallel} + \vec{G}) \cdot \vec{x}}, \quad (5.2)$$

$$I_T[k_{\parallel} = 0.2 \text{ \AA}^{-1}] / I_T[k_{\parallel} = 0 \text{ \AA}^{-1}] = 0.65 \quad (5.3)$$

Therefore the 1D band will contribute with the same order of magnitude to the tunneling signal as the hole band at the Γ point. This hole band on the other hand is also present at lower binding energies and therefore will be seen at all bias values

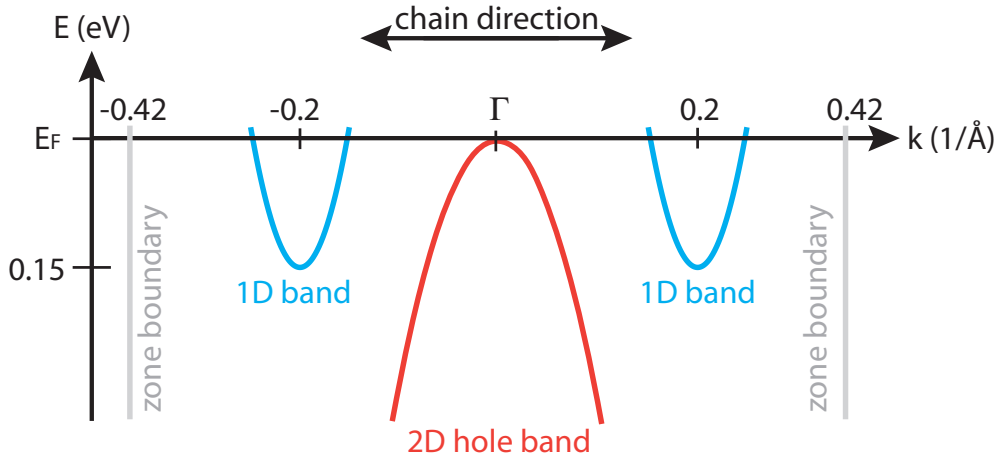


Figure 5.13: Schematic band situation for the Au/Ge(001) nanowires for discussion of the structure observed in STM. The 1D-band is electron-like and crosses the Fermi energy, while the 2D band has its maximum at E_F . More detailed analysis of the band structure is performed in chapter 6.1. Compiled according to [A.6].

for the occupied states. However, since this hole band has its maximum at the Fermi energy it will have no influence when imaging the unoccupied states. This might explain the dramatic change in the obtained topography when changing the tunneling polarity.

A summary of the band structure and a comparison to STM images is compiled in the following table:

ARPES	STM	structure	orbital character
hole band	occupied states	W+V	Ge 2p
1D band	\pm low bias	nodes	unknown
n.A.	unoccupied states	triplets	Au 6s

The occupied states at high binding energies are dominated by the hole band. This band is very similar to the Ge bulk band [A.6] and a connection seems appropriate. Note however that this band has no dispersion perpendicular to the surface and is therefore clearly a surface state [A.6]. The 1D band is of unknown origin and may result from a complex surface structure with multiple binding geometries. Yet, it is the only other band that clearly crosses the Fermi energy and thus must be held responsible for the structure in STM at low bias. The unoccupied states of course are only accessible by STM and not by ARPES for principal reasons. Therefore, the assignment of the triplets to the Au 6s orbital is not supported by

analysis of the bandstructure. However the spherical shape of the triplet charge clouds supports the conclusion of an s-orbital.

It should be stressed that the above discussion has to be viewed *cum grano salis*, since STM always detects structure and electronic effects simultaneously. Any final explanation may only be based on detailed DFT calculations. Yet, for the sake of discussion and as a starting point and input for a model these experimental observations are highly important.

5.3.4 Lateral confinement

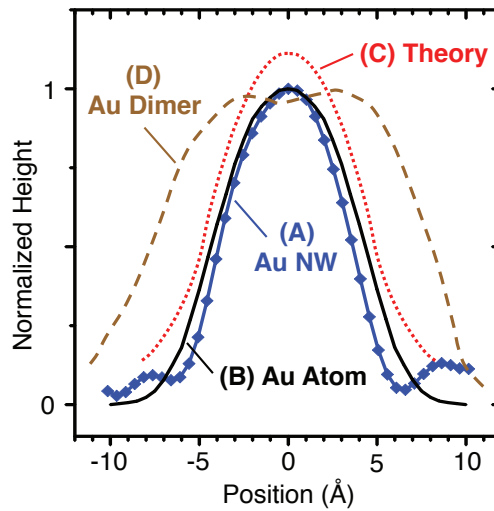


Figure 5.14: Lateral profile comparison. (A) Nanowire data, ~ 7.3 Å FWHM. (B) Single Au atom on alumina [133]. (C) Calculation for Na atom on metal surface [134], offset for clarity. (D) Au dimer on alumina [135]. The nanowire profile matches best with the single atom data. From [A.1].

Considering the lateral confinement of the charge within the nanowires, a detailed analysis of lateral profiles has been performed, see fig. 5.14. The wire width is determined to (7.3 ± 0.3) Å FWHM as seen by STM. Note, that this value includes the apex of the tip as well as the tunneling barrier. As a comparison measurements of a single Au atom on an alumina surface are shown in black [133]. Here the width is determined to 9 Å. Also the calculated profile for a Na atom on a metal surface is depicted as the red curve, yielding a FWHM of 8.9 Å [134]. Both comparison curves are in good agreement with the wire profile. In contrast the profile of an Au

dimer, brown [135], cannot be matched with the obtained wire width. Therefore, the assignment of a single atom in wire width seems appropriate. Note that STM does not probe the atom positions directly, as stated in chapter 3.1.2, but is an excellent probe for charge distributions. To conclude it is safe to say, that the charge along the wire is confined to atomic dimensions, which is unprecedented from related nanowires systems.

When comparing not only the lateral width but also the position of *neighboring* charge clouds in the occupied states images, fig. 5.15, a zig-zag amplitude of only $1.28 \pm 0.03 \text{ \AA}$ is detected. Such amplitude may not be explained by a buckled dimer, which has been proposed as a structural building block of the nanowires [136]. For comparison a Ge-Ge dimer at the free surfaces has a buckling undulation of 2.45 \AA [101]. Therefore the observed zig-zag may not be explained by a simple buckled dimer model. This important finding will be discussed in more detail in chapter 5.8 with the structural elements from DFT.

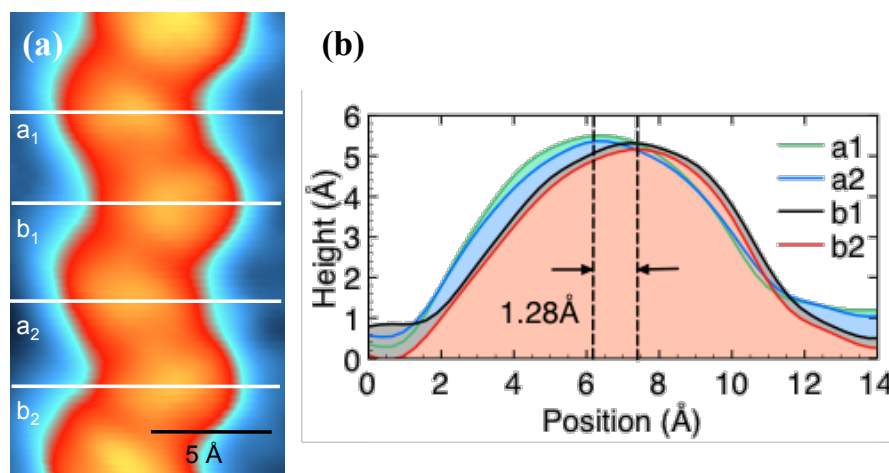


Figure 5.15: (a) High resolution STM image of the zig-zag chain element (-0.7 V , 0.4 nA , $1.1 \times 1.9 \text{ nm}$, 77 K) with four line profiles along the white lines. (b) Line profile analysis, leading to a zig-zag amplitude of $(1.28 \pm 0.03) \text{ \AA}$. From [A.9].

5.4 Dynamics

During the bias series of the Au/Ge(001) nanowires, chapter 5.3.3, no structural rearrangements of the chain architecture could be detected within the scan duration of approximately 12 hours. Yet in rare cases some parts of the wires appear noisy,

see fig. 5.16. On the right hand side of the image a vacancy defect interrupts the chain. Closely neighboring is a noisy area detected. The exact same sample surface was scrutinized two hours later with the same result, thereby excluding scan artifacts. Due to the slow scan speed of STM this noise may be due to a flipping of the wire structure between two configurations. Such effect has been studied by Mocking *et. al* [137], where their STM tip was fixed on the noisy area and the tunneling current was recored over time, see fig. 5.16 (c). It can be seen, that the current is alternating between two configurations, top and bottom. The frequency is determined to 25 Hz, which is far more than the scan speed in STM. They come to the conclusion that the dimer must be flipping between two energetically equivalent configurations. Note, that such noisy areas are only observed close to defects and therefore will not represent the undisturbed chain geometry. The finding of dynamics in the chains architecture will play an important role later on, when discussing the phase transition in chapter 5.7.3.

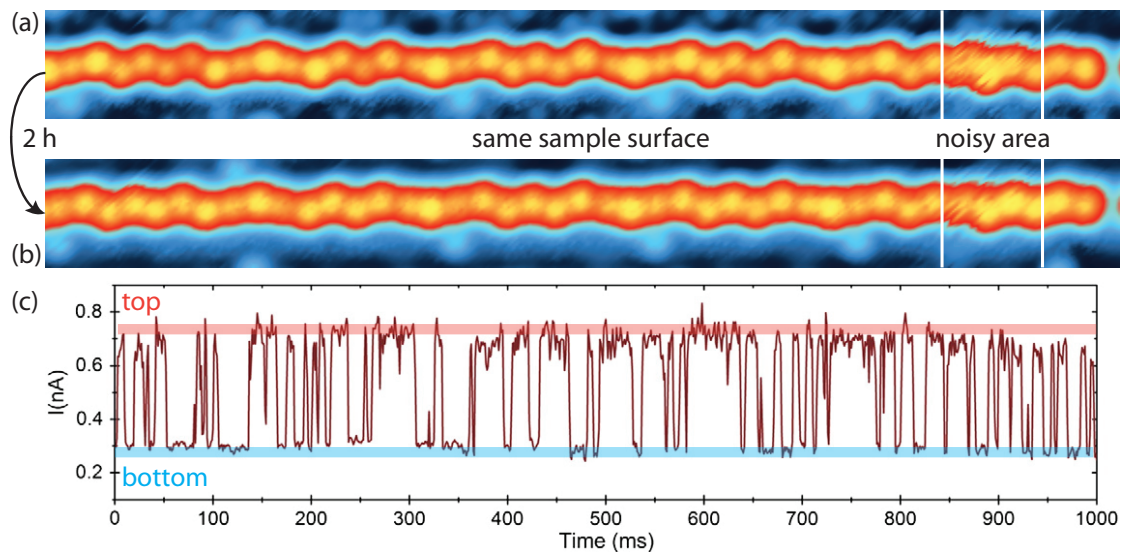


Figure 5.16: (a) (-1.6 V, 0.4 nA, 77 K) STM image of a single nanowire with chain end on the right. Close to the end the wire appears noisy, pointing at dynamics at the surface during the scan. (b) (-0.7 V, 0.4 nA, 77 K) exact same sample location 2 hours later. The noisy area is found at the identical distance from the chain end. (c) Tunneling current recorded over time on top of a noisy dimer (-1 V, RT) [137].

5.5 Fourier transformation

As laid out in the previous chapters the wire architecture seen by STM comprises a complex long range ordered structure with 32 Å periodicity and weak lateral order. A schematic of the surface unit cells is shown in fig. 5.17. Blue is the basic $c(8\times 2)$ unit cell, while red represents the superstructure. This may be denoted in a matrix as in eq. 5.1 or alternatively as a $p(4\times 1)$ supercell on top of the basic $c(8\times 2)$. As can be seen in the schematic, there are two possible configurations of the superstructure, *up* or *down*, depending on the arrangement of the supercell. STM images show, that such lateral alignment typically persists over five to seven wires [A.9]. This means, that large scale measurements will always detect both super cells simultaneously.

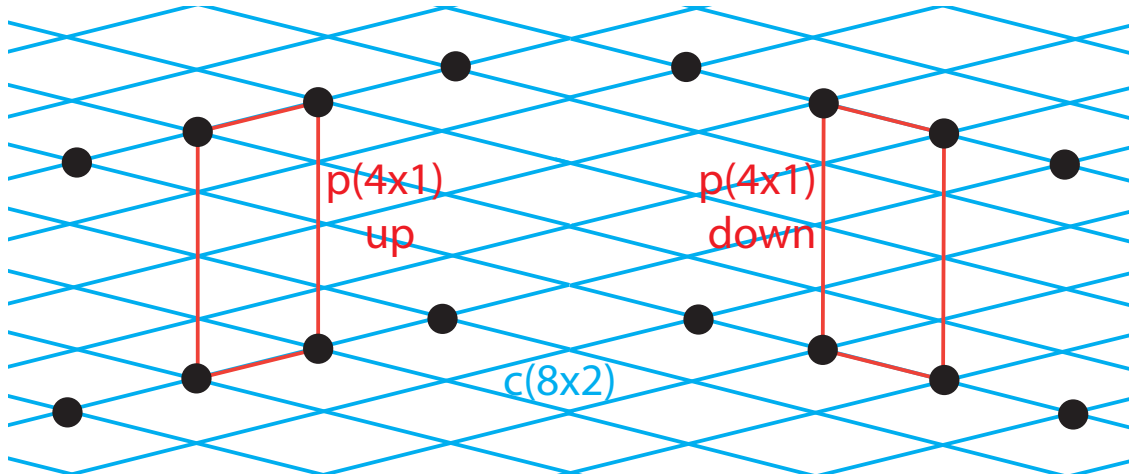


Figure 5.17: Schematic of the basic $c(8\times 2)$ unit cell in blue and $p(4\times 1)$ supercell in red. For the superstructure two lateral alignments exist, which are termed up and down.

A typical fast-Fourier transformation (FFT) STM image of a (50×50) nm² may be seen in fig. 5.18. The wire direction is vertical. In the center row there are strong peaks visible, which correspond to the wire distance of 16 Å. Next to this row the intensity maxima are more streaks than dots. This is the case for every second row. But upon closer inspection one identifies two maxima, that lie very close together. The complete pattern is readily explained by the superstructure model, left side of fig. 5.18. Here a simulated diffraction pattern is overlaid, shown as white dots. This simulation includes a basic $c(8\times 2)$ cell with a $p(4\times 1)$ superlattice with up and down domains. An almost perfect match with the FFT is made, while minor

deviations are due to some residual drift from the STM measurements. Note, that all reflexes are reproduced by the simulation, and also the streaks are explained with two closely neighboring dots.

The explanation of the FFT pattern is highly relevant for the complementary obtained diffraction pattern from LEED. However, since LEED averages over a sample area of about 1 mm^2 not only both superstructure domains will contribute to the signal, but also the two directions of the chains on the substrate. Therefore in total 4 different domains will be present in the diffraction pattern, leading to a very complex signal. The expected pattern is rendered in fig. 5.19.

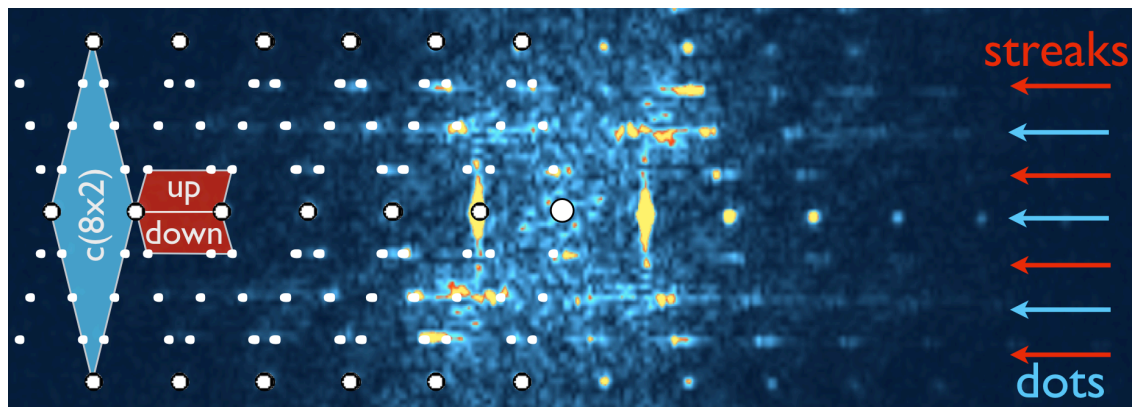


Figure 5.18: FFT of a $(50 \times 50) \text{ nm}^2$ STM image. Two types of intensities are seen: Streaks and dots. On the left hand side an overlay of a simulated diffraction pattern is shown. All reflexes are explained by the simulation. The $c(8 \times 2)$ unit cell is shown in blue and the two (up and down) $p(4 \times 1)$ supercells in red.

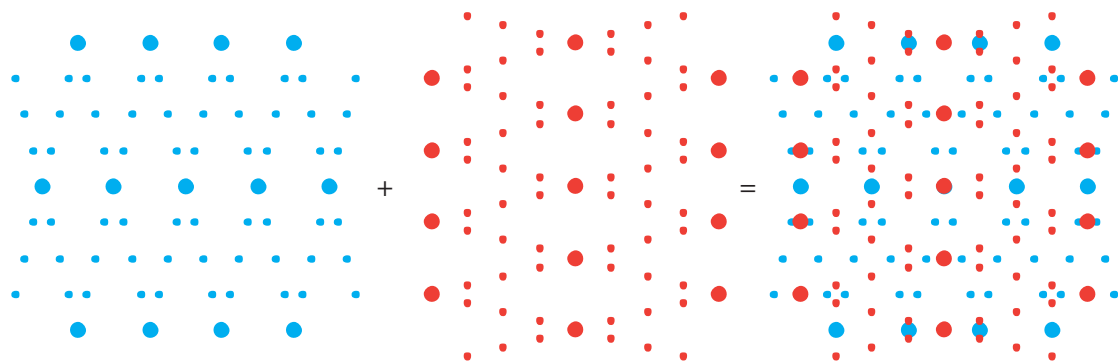


Figure 5.19: Addition of two domains from the chain directions leads to the expected LEED pattern.

5.6 Construction of the diffraction pattern

A typical LEED pattern at RT of the Au/Ge(001) surface is presented in fig. 5.20 (a). It shows very sharp reflexes and a low background, therefore demonstrating excellent sample quality and long range order. This pattern may be explained by the superstructure model with two substrate domains, fig. 5.19. The main reflexes of the basic $c(8 \times 2)$ are depicted as blue dots in fig. 5.20 (b). Since the stacking sequence of the substrate leads to two orthogonal wire domains and LEED detects both simultaneously, two unit cells contribute to this pattern. These are shown as blue diamonds. Yet on top of the basic symmetry many additional reflexes are detected. They originate from the $p(4 \times 1)$ superstructure with up and down domains. With this model all of the reflexes present in the pattern are readily explained. Note that some of the superstructure reflexes are very close together and therefore appear only as one single spot in the pattern. These are indicated as red dots in fig. 5.20 (b). Strong reflexes of the superstructure in LEED point at a highly long range ordered superstructure symmetry.

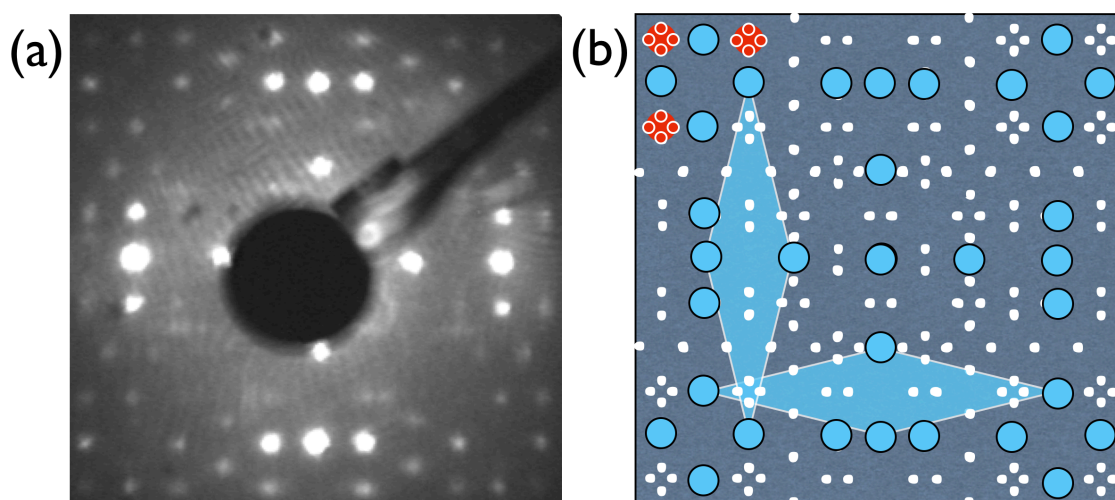


Figure 5.20: (a) Dual-domain LEED pattern (18 eV) at 300 K. (b) Geometric construction of the LEED pattern, accounting for the experimentally observed diffraction spots using a dual-domain pattern rotated by 90° . It originates from the two possible surface layer orientations of Au/Ge(001). Blue circles indicate reflections from the two basic $c(8 \times 2)$ domains. Small white circles originate from the additional superstructure, thereby proving the superstructure correlation matrix. Red circles represent closely neighboring reflexes, which appear as one spot in the diffraction pattern.

5.7 Phase transition

From the relating nanowires systems it is known, that phase transitions play an important role in the structure. Although in the In/Si(111), Au/Si(557) and Au/Si(553) chains the phase transitions have been interpreted as a Peierls instability, these claims were later challenged by alternative models, see chapter 4.1. The debates on the transitions in these systems have lead to a more general questioning of the relevance of Peierls physics in real world systems.

Consequently in the light of these previous debates also the Au/Ge(001) chains have been scrutinized over a wide temperature range for a possible phase transition. Specifically they were scrutinized for signatures of Peierls physics, such as energy gaps or periodicity changes as introduced in chapter 2.1.2. Most remarkably, it is found that a transition of the superstructure occurs *above* RT. This is confirmed in both diffraction and microscopy measurements, which are presented in the following chapters.

5.7.1 Transition observed in real space

Most previously presented STM data had been obtained at 77 K (LN₂). Under these stable tunneling conditions the delicate superstructure is best resolved. Towards lower temperatures, down to 4.7 K (LHe) no change in the structure is detected. Notably the superstructure also exists at RT, which is concluded from both the LEED pattern, fig. 5.20, as well as from tunneling images. Yet towards higher temperatures the superstructure vanishes completely. Fig. 5.21 shows equivalent sample surfaces of the Au/Ge(001) chains at 77 K and 600 K with (a) occupied and (b) unoccupied states respectively. A drastic change in the chain structure is detected in both states. At 77 K the characteristic triplet/V-W zig-zag is seen, while this 32 Å superstructure is completely absent at 600 K. A rather structureless chain is seen in both polarities with only a marginal zig-zag of 8 Å period. This corresponds very well with the basic $c(8 \times 2)$ symmetry of the chains. Furthermore no protrusions are detected in the grooves, but rather a ladder like structure, again with 8 Å period. Since these images were acquired at relatively high bias ± 0.8 V, this charge landscape will reflect the deeper bound states of the surface rather than

the conduction electrons. Note that this transition is completely reversible, with recovery of the superstructure upon cooling the sample from above T_C .

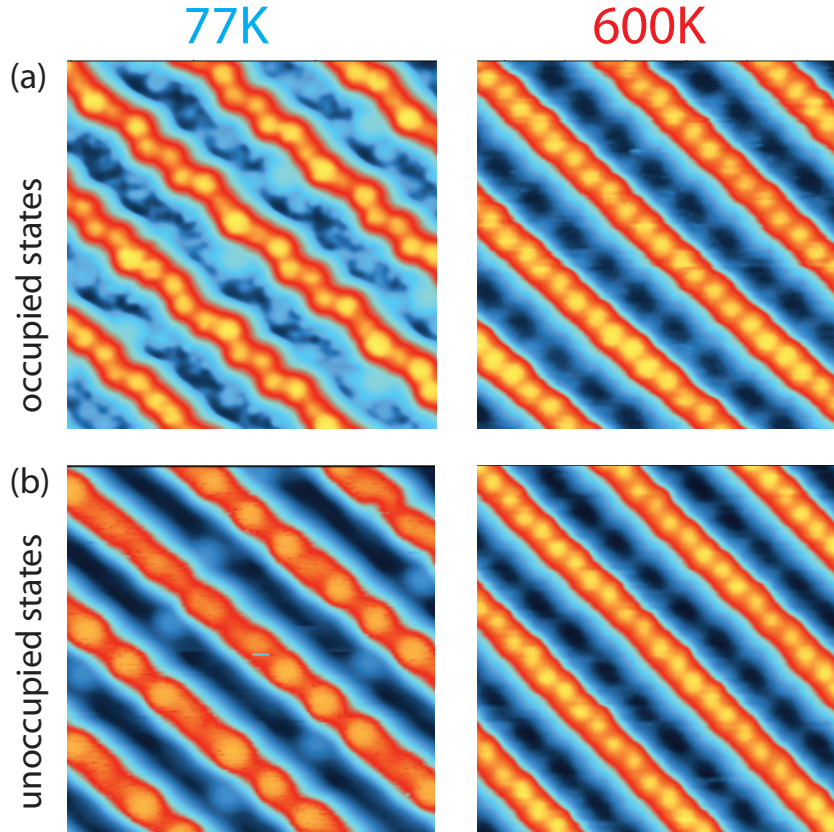


Figure 5.21: Comparison of STM images above and below the phase transition. (a) Occupied and (b) unoccupied states. Above T_C the fourfold superstructure vanishes completely but leaves the basic $c(8 \times 2)$ intact. At 600 K the chains show a marginal zig-zag of 8 \AA period on the chain top and a ladder like structure in the grooves with the same periodicity. The transition is fully reversible, with recovery of the superstructure upon cooling. From [A.9].

Further information on the transition may be gained by means of autocorrelated STM images. These show the periodicities present at the surface, fig. 5.22. Below the transition (a) clearly both symmetries are visible: $c(8 \times 2)$ as well as both superstructure domains. Yet the $p(4 \times 1)$ up domain appears much stronger. This is explained by the finite averaging window of the $50 \times 50 \text{ nm}^2$ STM image, where a domain imbalance may be present. Furthermore, intensity is seen halfway between the wire distance, indicated as white arrows in fig. 5.22 (a). Clearly this is due to

the observed protrusions in the grooves at low temperatures. In turning to the high temperature autocorrelation map (b), much less intensities are identified. In fact only the basic $c(8\times 2)$ cell is seen. Interestingly at the groove distance no intensity from the protrusions is detected, but rather two closely neighboring rows at a distance of 4 Å. In chapter 5.8 these observations will be important for the discussion of a possible structural model for the reconstruction.

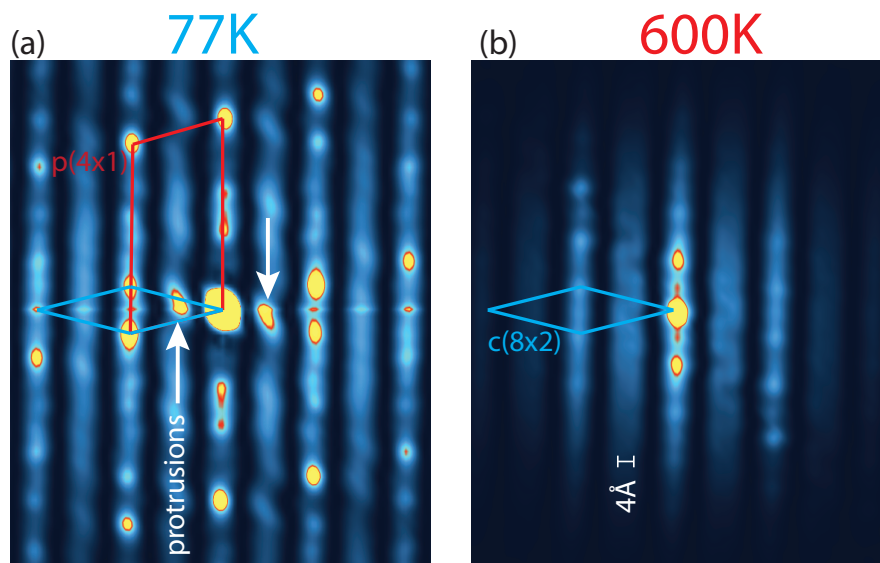


Figure 5.22: Autocorrelated STM images (a) below and (b) above T_C . At 77 K distances from the superstructure are clearly visible. In addition, at half the wire distance intensity appears (white arrows), which matches the protrusion distance in the groove in real space. At 600 K only the basic structure is seen and no strong intensity between the wires is resolved.

5.7.2 Transition observed in reciprocal space

The phase transition can be scrutinized in much more detail by using electron diffraction. Since LEED averages over a sample surface of about 1 mm^2 more quantitative information about the transition is gained. A quantitative examination of the LEED series, which was subsequently taken on the same sample surface, fig. 5.23, it is apparent that the superstructure reflexes (see fig. 5.20 (b)) undergo a dramatic intensity change. At the same time the $c(8\times 2)$ reflexes remain constant in intensity. By increasing the temperature from RT the superstructure reflexes

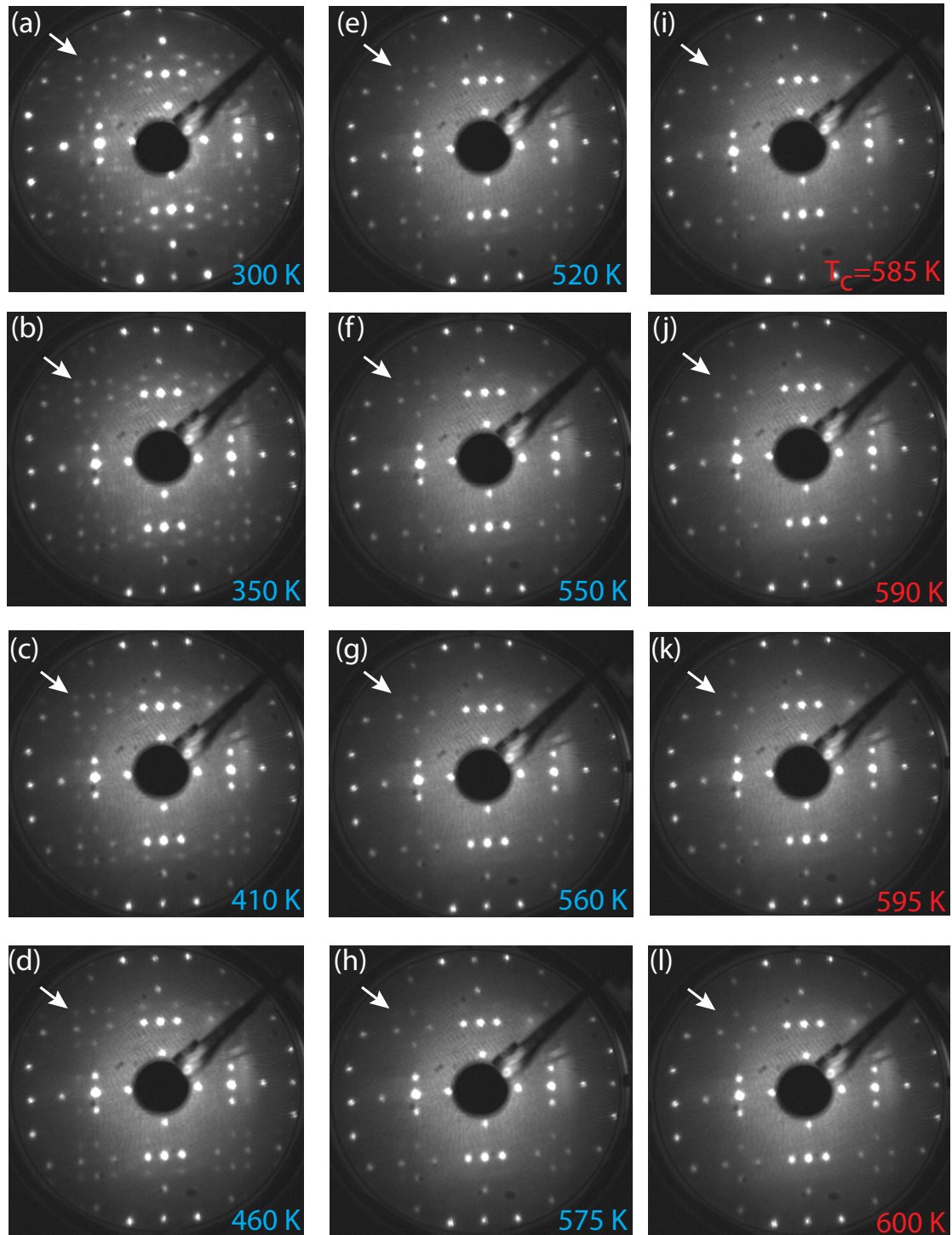


Figure 5.23: Series of LEED patterns over a wide temperature range 300 K to 600 K. (a-h) below T_C superstructure reflexes are visible. (i-l) above the transition only the $c(8 \times 2)$ pattern remains, with almost equal intensity. No effects of surface melting or charging are detected.

become increasingly darker and vanish completely at 585 K. Up to 600 K only the basic symmetry of the surface prevails.

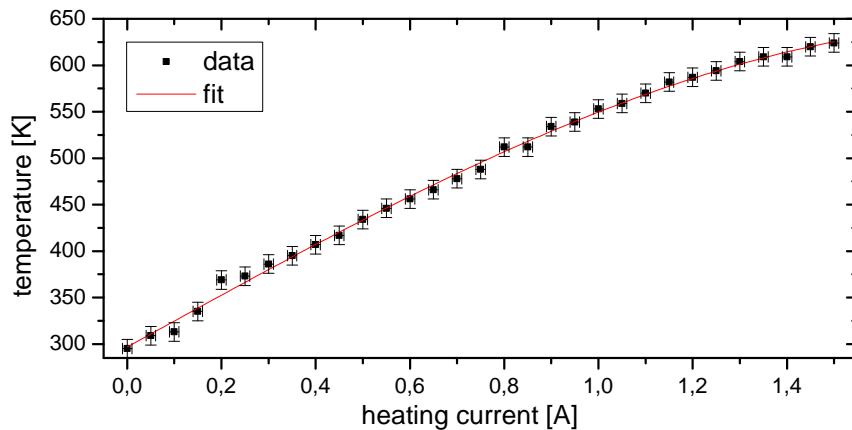


Figure 5.24: Temperature of the sample as a function of the direct heating current for calibration. The k-type thermocouple is directly attached to the sample surface at ambient pressure.

In order to accurately determine the surface temperature through the transition, a calibration curve was recorded. A K-type thermocouple was directly attached to the sample surface and the temperature was measured in air. In order to minimize the heat loss due to convection, the sample holder was covered with a glass beaker. The direct-heating current was subsequently increased, while the temperature of the sample was recorded. The obtained data are plotted in fig. 5.24. Error bars in temperature were estimated to ± 5 K from statistical deviation of different calibration measurements. With this curve a detailed examination of the transition temperature may be performed.

In looking at the phase transition in a quantitative way, the intensities of the Bragg reflections of the superstructure were monitored using LEED. For the analysis, the superstructure equivalent reflections indicated by green circles in the inset of fig. 5.25 have been chosen. In total 12, reflections were averaged to gain statistical confidence. Also only directly neighboring reflexes from the $c(8 \times 2)$ were chosen for reference. As already seen in the LEED pattern series, a dramatic decrease of the superstructure intensity with increasing temperature takes place, see fig. 5.25. Above 585 K the superstructure vanishes completely, while the $c(8 \times 2)$ reflections remain virtually unaffected by the temperature change, see also inset of

fig. 5.25. This is a reversible process with full recovery of the superstructure intensity upon cooling. Effects from sample charging or decomposition of the structure can thereby be excluded. The data can be interpreted as a continuous second-order phase transition. The measured superstructure intensity $I(T)$ may be fitted with a power-law upon temperature [138] using

$$I(T) \propto \rho^2(T) \propto \left(\frac{T_C - T}{T_C} \right)^{2\beta}, \quad (5.4)$$

with the order parameter $\rho(T)$ which serves to minimize the free energy. It is interpreted as the transversal displacement of the local charge density seen in STM. In diffraction experiments, the intensity $I(T)$ of the superstructure Bragg scattering is proportional to $\rho^2(T)$ [139]. A close fit to the data is achieved for a critical temperature $T_C = (585 \pm 10)$ K, and the exponent $\beta = 0.29 \pm 0.04$.

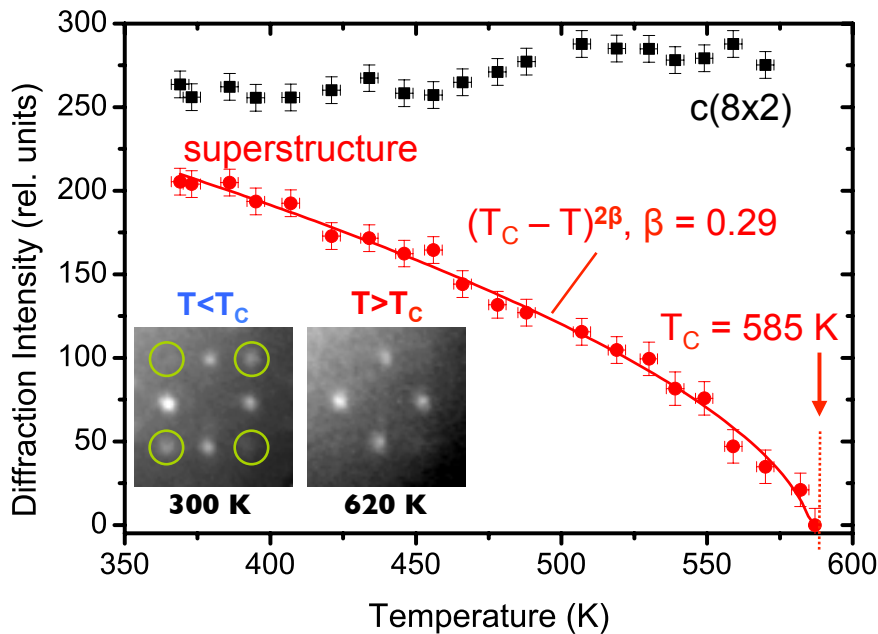


Figure 5.25: T -dependent LEED intensity analysis for basic $c(8 \times 2)$ (black) and superstructure (red) diffraction spots. The superstructure undergoes a 2nd-order phase transition with $T_C = 585$ K, while the underlying $c(8 \times 2)$ structure remains unaffected. Inset: Enlarged LEED images above and below T_C . Green circles indicate reflexes chosen for T -dependent analysis. From [A.9].

Role of Debye-Waller factor for scattering intensities

As laid out in chapter 3.3.4, temperature has an influence on the reflex intensity due to the movement of the atoms inside the unit cell. This effect is accounted for in the Debye-Waller factor [77]. In order to quantify the contribution of this effect several different scenarios have been computed. In using the expression derived in chapter 3.3.4, eq. 3.32

$$I(T) = I_0 \exp\left(-\frac{12h^2}{mk_B} \left(\frac{\cos(\phi)}{\lambda}\right)^2 \frac{T}{\Theta_D^2}\right), \quad (5.5)$$

with m the mass of the scattering atom, ϕ the scattering angle of the scrutinized reflexes, λ the electron wavelength, and Θ_D the Debye temperature. For the temperature dependent LEED study, one may calculate the intensity ratio for the highest and lowest temperature, 300 K and 600 K:

$$\frac{I(600K)}{I(300K)} = \exp\left(-\frac{12h^2}{mk_B} \left(\frac{\cos(\phi)}{\lambda}\right)^2 \frac{300K}{\Theta_D^2}\right). \quad (5.6)$$

The scattering angle of the scrutinized reflexes is about $\phi = 72^\circ$ and therefore is a dominant contribution in the expression, since the intensity follows $I \propto \exp(\cos(\phi)^2)$. Thus, the overall change in intensity will be rather small, compared to reflexes at lower scattering angles. For bulk Ge ($m = 73$ u, $\Theta_D = 374$ K, $\lambda(25$ eV)) one obtains 1.1 % intensity change over the whole 300 K window. Another possibility would be the use of values for Au ($m = 197$ u, $\Theta_D = 165$ K, $\lambda(25$ eV)), leading to a 2.0 % change in intensity. By using the calculated surface Debye Temperature of Au [140], $\Theta_{D,surface} = 110$ K the change would result in 4.5 % over 300 K. In any of these scenarios, the small magnitude of these relative changes exclude a noticeable Debye-Waller contribution.

5.7.3 Origin of the transition

As seen in the related chain systems, refer to chapter 4.1, also in the Au/Ge(001) nanowires a structural transition occurs. Yet in the present case the transition temperature is above RT rather than below. One might speculate if this transition is due to a Peierls instability. The high transition temperature would lead to a large energy gap at low temperatures. Since the ARPES experiments documented, that

the band structure of the nanowires consists only of a single band at the surface [A.1, A.6], see fig. 5.13, a Peierls transition would render the surface insulating [22]. The expected size of the energy gap may be estimated within the mean-field approach by using eq. 2.12. A transition temperature of $T_C = 585\text{K}$ would result in a zero temperature energy gap of

$$2\Delta = 3.52k_B T_{CDW}^{MF} = 177 \text{ meV}, \quad (5.7)$$

which is of the order of the filled bandwidth of the 1D electron band, see fig. 5.13. Although the mean-field gap is always overestimated, a reduction by a typical factor of four [43] would still result in a gap of approximately 45 meV, which is easily detected in STS and ARPES. Yet as will be shown in the study on the electronic properties of the chains, see chapter 6, no energy gap exists around the Fermi energy as seen by STS. This proves persistent metallicity in the ordered phase. Consequently an electronic Peierls component to the transition may be excluded. This conclusion is further corroborated by an analysis of the Fermi surface nesting situation [A.6]. Possible nesting vectors may be determined from the band situation in fig. 5.13. Corresponding real space periodicities would result in $\lambda_1 = 66 \text{ \AA}$, $\lambda_2 = 28 \text{ \AA}$, and $\lambda_3 = 15 \text{ \AA}$ CDW repeat lengths. All of these do not match the observed 32 \AA repeat length in chain direction. As a result the origin of the transition is clearly not driven by a Peierls mechanism.

A further possibility for the transition may be the buckling of dimers perpendicular to the chain direction. As shown in fig. 5.16 there are isolated wire segments at 77 K, that perform a flip flop motion over time. This flipping might be enhanced at higher temperatures, thus leading to a reduced buckling seen by STM. As already extracted from line profile analysis, the W-shape of the LT phase has a transversal undulation amplitude of only $1.28 \pm 0.03 \text{ \AA}$ at 77 K, see fig. 5.15. Upon heating this undulation is reduced to almost zero, fig. 5.21. However the width of a e.g. Ge-Ge dimer of clean Ge(001) amounts to 2.45 \AA [101], which is twice as wide as the low temperature undulation. Therefore a flip-flop motion of dimers can not explain the transition. Consequently the transition has to be of displacive character.

Considering the dimensionality of the transition one may compare the obtained critical exponent $\beta = 0.29$ with that of known transitions from the literature. The closest match within error bars is the 3D Ising model with $\beta = 0.33$ [138]. Interest-

ingly this would imply that the transition of the 1D chains is of higher dimensional character. A diffraction study on the Ag/Si(111) reconstruction found a similar value of $\beta \sim 0.27$ [141, 142]. This 2D reconstruction was found to undergo an order-disorder transition upon cooling. There the substrate is thought to interact with the 2D reconstruction in the transition, thus leading to a 3D interaction of the whole structure.

Information about the dimensionality of the transition may also be gained from the behavior around the critical temperature. In the ideal 1D chain proposed by Peierls, the long range order of a CDW will be suppressed due to fluctuations until $T = 0K$. Coupling of the electronic states to higher dimensions is need to stabilize the long range order [22]. Yet fluctuations will still be present around T_C , thus leading to a smeared out transition region for the order parameter. This is in stark contrast to the findings from the LEED study, where a sharp transition is observed at 585 K. Therefore the transition has to be of higher dimensional character.

How can the dichotomy between a 3D structural phase transition in a highly confined 1D nanostructure be explained? It will be shown that the scrutinized Au/Ge(001) chains show an unprecedented degree of one-dimensionality in the electronic structure as seen by ARPES, see chapter 6.1. Therefore these chains seem to be the ideal test system for a real world Peierls scenario. However in the considerations about the phase transition the total energy of the system and consequently all electronic states have to be taken into account. These include not only the 1D conduction electrons, but also the substrate back-bonds as well as substrate-mediated bonding between the chains. The finding of a 3D type transition leads to the conclusion, that the 1D electron system in the Au wires is completely decoupled from the underlying structural elements, participating in the phase transition. Such finding questions the relevance of the Peierls picture for real-world systems. In the Peierls model only one band exists, while in all experimentally accessible nanowires many electrons from different orbitals contribute to the ground state.

This finding is highly relevant for the related chain systems and their observed transitions, see chapter 4.1. The initial interpretation of an electronically driven transition was later challenged by structural models, e.g., the hexagon model of In/Si(111) [87, 88] and likewise the step edge buckling for the Au/Si(557) chains [92, 143]. The present studies may not exclude, that in these systems an electronic contribution to the transition is possible. Yet the current findings indicate that a

Peierls instability as a driving force for a transition in real-world systems seems highly unlikely and that the model is too simplistic to describe an experimental system. This was recently also predicted by a theoretical study by Johannes *et al.*, which concluded, that a Peierls instability cannot be the driving force for a phase transition, since the state is too fragile against the influence of finite temperature, imperfect nesting or scattering [44]. Consequently non-Peierls-type transitions need to be considered more closely in all related nanowire systems at semiconductor surfaces.

5.8 Structural model from first principles

The determination of the atomic arrangement that builds the highly confined Au/Ge(001) nanowires is very challenging. The initial model proposed by Wang *et al.* [37, 38] with alternating rows of Au-Ge and Au-Au dimers, see fig. 5.2 (b) could not be confirmed by our STM studies. The observation of two kinds of rows could not be reproduced. Based on their own STM images van Houselt *et al.* proposed a giant missing row reconstruction with large faceting of the surface in order to account for the high corrugation as seen by STM [136]. This model consists of two Au incorporated (111) facets and a Ge dimer on top. Yet later studies identified this model as being energetically unfavorable [A.5].

In order to solve the problem a collaboration with the group of Prof. Bechstedt was initiated. He is an expert in the field of DFT and has already resolved the structure of the related Pt/Ge(001) chains [124, 125]. However due to the very complex long-range order of the Au/Ge(001) surface, involving the fourfold superstructure, determination of the bonding geometry by means of DFT is a rather challenging task. Large unit cells lead to long computation times. Therefore a first DFT study dealt with the basic $c(8\times 2)$ symmetry of the surface only, neglecting the superstructure [A.5]. As much as 150 different models have been inspected for their energetic stability. Yet unfortunately none of them is able to accurately describe the observed tunneling images or the band structure from the ARPES data. Consequently further work is needed in this direction. The closest match is the AD/HD model, which involves alternating rows of Au-Au homodimer (AD) and Au-Ge-heterodimer (HD), see fig. 5.26. This model will be discussed here.

The proposed structure follows the basic $c(8\times 2)$ symmetry. It also has a gold coverage of $3/4$ ML, which is in good agreement with the calibrated LEED study [126]. Using the generalized gradient approximation (GGA) the surface energy is -0.7 eV per unit cell compared to the free surface. Thus a stable reconstruction is achieved. As apparent from the model the wires are built from Au-Ge heterodimers, while the trough consists of Au homodimers. From the perspective view, fig. 5.26 (b), a slight buckling of the heterodimers is visible. Note that the AD and HD rows lie at the same height on the substrate and thus the surface shows no strong structural corrugation.

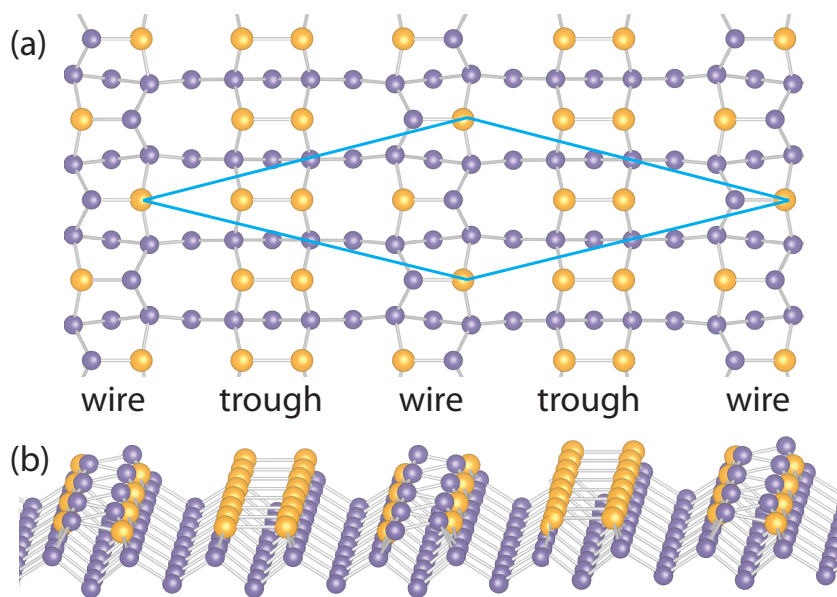


Figure 5.26: AD/HD model for Au/Ge(001) surface. (a) Top view, unit cell blue. The troughs are built from Au-dimers (golden), while the wires consist of Au-Ge-heterodimers (Ge grey) (b) Perspective view, showing slight buckling of the heterodimers. From [A.5]

In order to test the results obtained from DFT, STM images have been simulated, see fig. 5.27. For comparison with experiment, STM images above the phase transition temperature have been chosen, which only include the basic $c(8\times 2)$ symmetry. The simulation for (a) occupied and (b) unoccupied states show a pronounced zig-zag chain with a period of 8 \AA . Although a weak zig-zag is also seen in experiment, the model clearly does not arrive at matching the STM data. The troughs appear rather structureless in DFT, but show an 8 \AA ladder like structure in the unoccupied states. This is confirmed by STM, although this structure is visible in both

states. From the model it can be associated with the Au-dimer structure, building the trough. The HD row seems to have a much more pronounced density of states, since the AD chains are at the same structural height. Therefore a 1D electron path is identified in the HD chain. Also no side bonds are seen from DFT, which hints at a strong confinement of the electrons in the wire. Note that the earlier findings of a conduction path with atomic width and the exclusion of a buckled homodimer, chapter 5.3.4, are not contradictory to the current model. In the simulated STM images it becomes apparent, that the DOS is strongly confined to the Ge atoms, see fig. 5.27. Consequently a narrow conduction path with slight buckling may be realized.

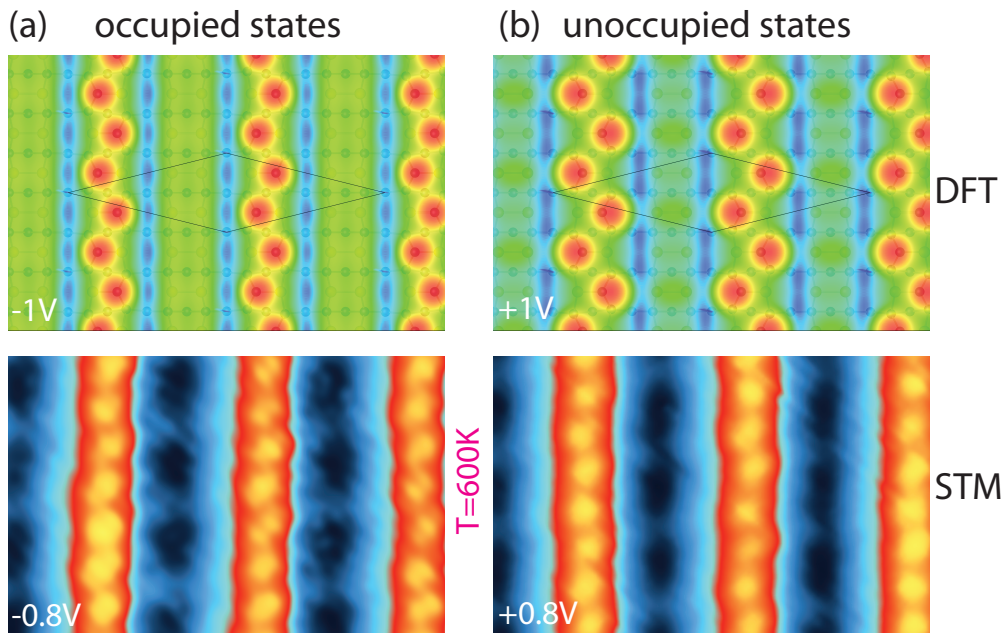


Figure 5.27: Comparison of simulated STM images by DFT with experimental tunneling images above the phase transition temperature. (a) Occupied states, a weak zig-zag is seen in simulation and experiment. (b) Unoccupied states, the strong zig-zag from DFT is not reproduced by STM. A ladder like structure is seen in the troughs, which is also present for both tunneling polarities in experiment. DFT from [A.5].

It should be emphasized, that the model does not describe the complete structure as seen by STM. Nor does it reproduce the correct band structure. Moreover it cannot explain the complex ground state of the system with the delicate long range ordered superstructure. Yet, some elements from the basic symmetry can be matched with the high temperature phase. Therefore some elements will also be

present in the low temperature phase and it may serve as a starting point for more detailed studies. Furthermore some elements of this model could be confirmed by our most recent surface X-ray diffraction (SXRD) studies which were performed in the low temperature phase [A.13].

Consequently the quest for the correct model is still ongoing. In all previous DFT simulations only the topmost layer has been rearranged. It is likely that the surface has to be reconstructed several layers in order to result in the correct structure. Further efforts may use the results obtained in this chapter as input and test in order to verify their models.

Summary

The studies on the structure of the Au/Ge(001) nanowires show an unprecedented degree of structural anisotropy at a surface. The main findings on the structure of Au/Ge(001) are:

- (i) The nanowires grow on large terraces with lengths up to 100 nm.
- (ii) Profile analysis shows confinement of the electrons to atomic dimension in width.
- (iii) The wire spacing is 16 Å, far beyond orbital overlap.
- (iv) No crossbonds are detected over a wide energy range in STM.
- (v) A weak lateral superstructure exists on top of the basic chain symmetry.

Consequently questions on the dimensionality of the electron system and the conduction properties come to mind. Therefore, detailed studies by means of ARPES and STS have been performed over a wide temperature and energy range, which will be shown in chapter 6.

6 Electronic properties of Au/Ge(001) nanowires

The studies on the structure of the Au/Ge(001) nanowires show an unprecedented degree of structural anisotropy at a surface, see chapter 5. Consequently questions on the dimensionality of the electron system and the conduction properties come to mind. It will be interesting to see if these chains fall into the quasi-1D regime as the In chains on Si(111) or the Au chains on Si(553) and Si(557), see chapter 4.1. This may possibly result in energy gaps in the spectra and insulating properties due to a Peierls ground state. On the other hand the extreme confinement of the Au/Ge(001) chains may lead to a new class of strictly 1D chains at surfaces. Thus the desired TLL state may finally be realized.

In order to scrutinize the electronic properties, detailed studies by means of ARPES and STS have been performed over a wide temperature and energy range. While ARPES is paramount to determine the band dispersion and dimensionality of the electron system, STS is an excellent tool to study the DOS locally with atomic resolution.

6.1 Electronic band structure from ARPES

As already laid out in chapter 5.2, two orthogonal wire domains exist at the surface with equal share. Therefore ARPES measurements will always probe both domains simultaneously. Fig. 6.1 (a) shows the Fermi surface of the Au/Ge(001) chains measured at a photon energy of $h\nu = 100$ eV. A two dimensional square is identified around the surface Brillouin zone (SBZ) center $\bar{\Gamma}$. It is a result of the contributions of the two domains. For clarity the two SBZs are sketched in blue and orange, respectively. Consequently only 2 parallel sheets of the Fermi surface belong to

one domain, thus rendering the electron system highly 1D. Note that contrast in higher SBZs is suppressed. This is due to optical matrix element effects at this energy [79]. A band map through the center of the SBZ (white line in fig. 6.1 (a)) is shown in fig. 6.1 (b). Two electron pockets are revealed with the band minimum at $\pm 0.2 \text{ \AA}^{-1}$. The band width is about 150 meV. No dispersion in k_{\perp} is seen, when the incident photon energy is varied. Therefore this band clearly shows surface character. Since such a band is not known from the pristine Ge(001) surface [144] it must clearly originate from the Au chain reconstruction. A detailed analysis of the bandstructure has been performed in [A.6] and revealed no dispersion perpendicular to the wire direction within the resolution of the experimental setup.

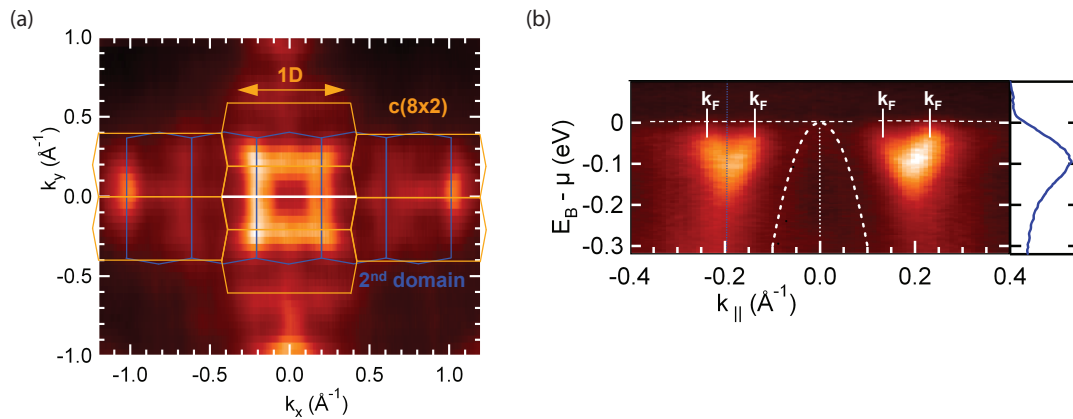


Figure 6.1: (a) ARPES Fermi surface overview at $h\nu = 100 \text{ eV}$, $T = 15 \text{ K}$ from dual-domain sample. The two sheets within the SBZ are rather straight, perpendicular to the corresponding 1D direction. Higher SBZs appear suppressed, which is ascribed to matrix element effects. (b) ARPES band map at $h\nu = 100 \text{ eV}$ and $T = 15 \text{ K}$ along chain direction through $\bar{\Gamma}$. Two shallow electron pockets are seen (EDC taken at blue dotted line). From [A.6].

Consequently, a band situation as sketched in fig. 6.2 (a) is identified. The electron pocket has no dispersion perpendicular to the wire direction and therefore will result in two parallel troughs (shown in orange) [A.6]. The SBZ is overlaid in blue. Fig. 6.2 (b) shows a sample with slight domain imbalance, where two perfectly straight Fermi surface sheets are seen.

Such dramatic display of one-dimensionality for chain systems at surfaces is unprecedented in the literature. Tight binding fits of the band structure of Au/Si(557) resulted in the ratio for the parallel and transverse hopping integral of $t_{\parallel}/t_{\perp} > 60$ [89], which may be regarded as a good measure of the dimensionality. The well

known Bechgaard salts, which show quasi-1D properties have a ratio of $t_{\parallel}/t_{\perp} \sim 10$ [41]. For the In/Si(111) chains one surface band exhibits an anisotropy of about 72 [85], see also chapter 4.1. Those fits could be achieved by the clearly observable perpendicular dispersion. In the case of Au/Ge(001) a value for the hopping integral ratio may not be given, due to the lack of detectable dispersion perpendicular to the chains. Yet as an upper boundary the dispersion is perfectly straight perpendicular to the chain direction within the momentum resolution of $\delta k = 0.004 \text{ \AA}^{-1}$ [A.6]. In fact, this is almost a factor of 10 smaller, than the clearly detectable undulation e.g. in the Au/Si(553) chains [98], with $\delta k = 0.03 \text{ \AA}^{-1}$.

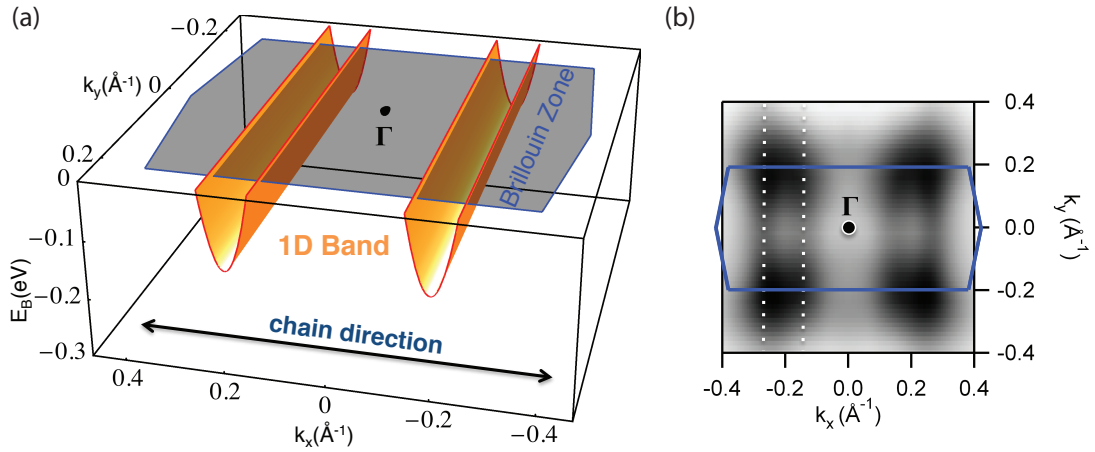


Figure 6.2: (a) Schematic of the band situation in the Au/Ge(001) chains. The 1D band forms two electron pockets (orange). These show parallel sheets in the Fermi surface, and are dispersion-less perpendicular to the chain direction within error margins. The Brillouin zone is overlaid in blue. (b) ARPES Fermi surface data measured at $h\nu = 100$ eV and $T = 15$ K, after [A.6]. As guide to the eye, white dotted lines show the straight dispersion perpendicular to the 1D direction.

Note that there is a competing view about the dimensionality of the electron system of the Au/Ge(001) chains. Nakatsuji *et al.* have also performed ARPES studies on these chains [145]. They end up with a 2D dispersing state for the surface. However they only present second derivative data, due to contrast problems with the raw data files. These results can not be reconciled with the data presented in fig. 6.1.

Furthermore Nakatsuji *et al.* performed ARPES studies on mono-domain samples, where a domain imbalance results in the formation of mostly parallel wires [146]. Yet the surface quality suffers from many disordered steps and again only low

statistics data are presented in second derivative. In these experiments also a clear 1D Fermi surface is identified, thereby matching our results. Only towards higher binding energies their surface state becomes increasingly 2D. Most interestingly, they claim the strong dispersion direction of the surface state to be *perpendicular* to the wire direction. This implies, that the conduction path at the surface would also be oriented perpendicular to the wires. In order to scrutinize this unintuitive finding we have acquired DOS maps of the Au/Ge(001) surface. There the conduction direction may be identified in real space with atomic resolution.

6.2 Density of states maps

STM was used to identify the DOS distribution at the surface with atomic resolution by acquiring the topography and dI/dV simultaneously with a lock-in amplifier (see chapter 3.2.2). Such measurements may be utilized to probe the dispersion relation of the surface states on metal crystals [147] and even to determine the Fermi surface of complex superconductors [148]. For the Au/Ge(001) chains we have used this technique to determine the strong dispersion direction at the surface and thereby contribute to the discussion on the dimensional character of the surface electron pocket.

A bias series of the topography and dI/dV is shown in fig. 6.3. The energy window extends over ± 100 meV, which lies within the band depth of the 1D electron pocket. Note that the images at -100 mV, -50 mV and -40 mV suffer from slight tip broadening, which is also apparent in the topography images. Moreover in the DOS images bright and dark regions may be identified, that are not visible in the topography images. These are most likely attributed to the Coulomb field of dopants from the substrate, which reside right below the surface. This is a well studied effect known from n-doped Si(100), where the subsurface dopants lead to an altered charge landscape of several nm [149]. This local change of the DOS will also influence the tunneling spectra, taken at different locations. Yet by averaging over a sufficiently large sample areas these effects will be averaged out and only the unaltered DOS signal from the nanowires may be obtained, as will be shown in chapter 6.3.1.

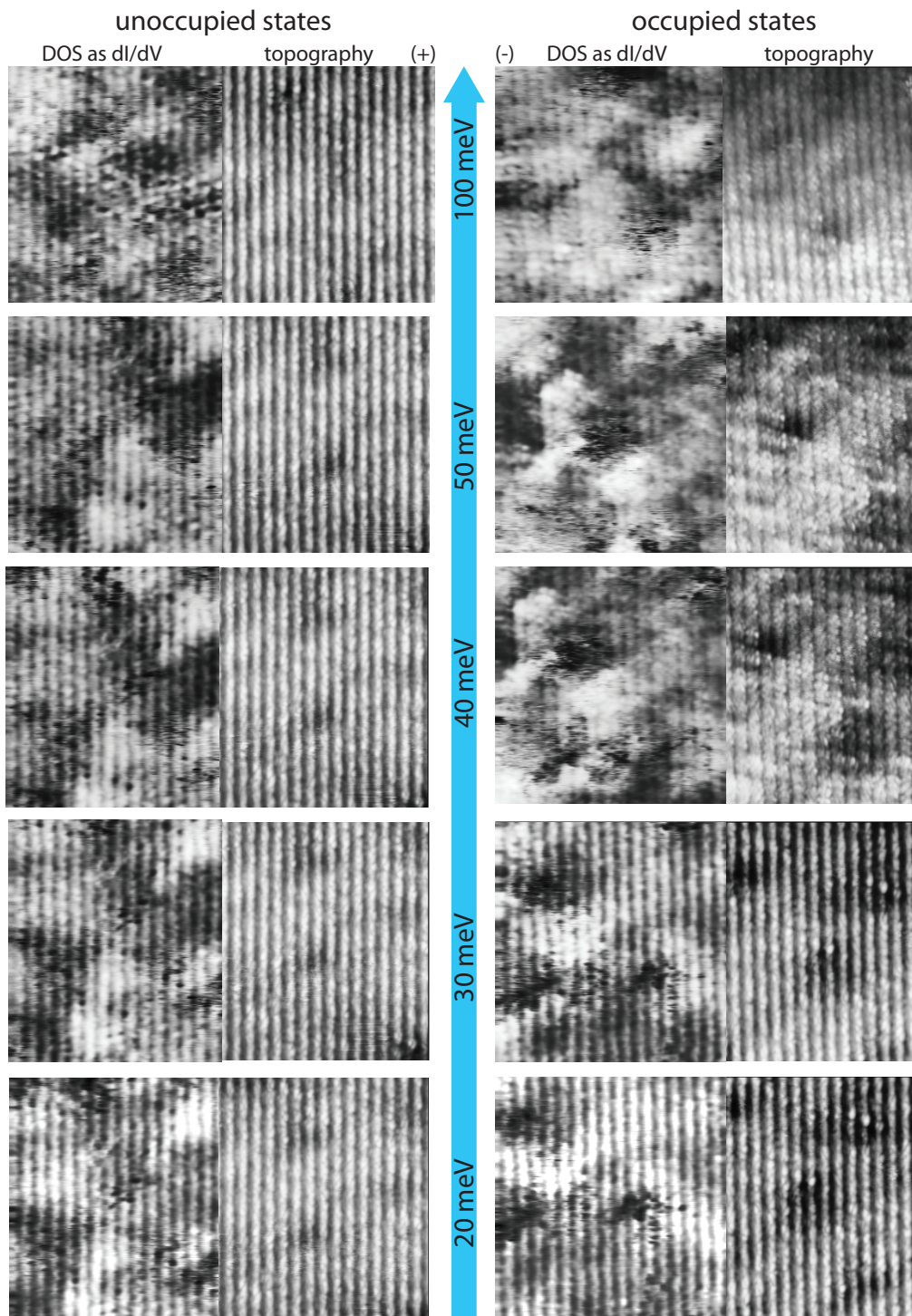


Figure 6.3: Simultaneous DOS and topography measurement of the Au/Ge(001) chains ($I = 0.4$ nA, $U_{eff} = 7$ mV). A clear 1D direction is identified in both DOS and topography along the chains.

In all of the 10 probed states a clear 1D direction of the DOS is identified along the chain direction as seen in the topography image, fig 6.3. The DOS is spread out along the chain direction and nicely separated between the chains. Clearly no conduction paths perpendicular to the chains are found in the scrutinized energy regime. Therefore claims from Nakatsuji *et al.* for a strongly dispersing state in ARPES perpendicular to the chain direction [146] cannot be corroborated with the present STM results. Consequently an interpretation of the 1D band as deduced from photoemission in fig. 6.2 is strongly supported by the DOS measurements. A possible explanation for this dispute may be given by analysis of the DOS at higher binding energies.

In going further away from the Fermi energy with the study of the DOS maps, the preferential direction of the conduction filaments is rotated by 90° . In fig. 6.4 (a) the Au/Ge(001) nanowires are seen as a topographic image. On the right lower terrace the wire orientation is horizontal, as indicated by the white arrow. In the DOS of the same area at an energy of -230 mV, one observes filaments, that are oriented vertically, see fig. 6.4 (b). These are spaced at 32 \AA and therefore have an eightfold periodicity compared to the 4 \AA Ge lattice constant. On the left terrace one observes the same rotation by 90° . Note that the 1D band is not existent at this binding energy and therefore cannot contribute to the DOS signal, see fig. 6.4 (c). As a result these filaments have to originate from deeper bound states, possibly the back bonds of the wires to the substrate. In using a different photon energy $h\nu = 35 \text{ eV}$ to probe the bandstructure a split-off band of the 2D hole band becomes visible [A.16]. Notably, this band and its backfolded counterpart have a crossing right below the 1D band. At a binding energy of 230 meV only these states may be detected in STS. Consequently this might lead to the rotated filaments observed in the DOS.

One may speculate, if Nakatsuji *et al.* have studied the dispersion of these states [146] instead of 1D band and therefore assumed a 90° rotated scenario compared to our interpretation. This could be explained by a different doping level of their substrates, resulting in a different chemical potential. Eventually high-resolution mono-domain ARPES measurements on high quality samples are needed to find a final answer on this debate.

Since all our ARPES and STS experiments point at a highly confined electron system with unprecedented character of one-dimensionality, we will now focus on the low energy excitations of the nanowires in order to look for 1D physics.

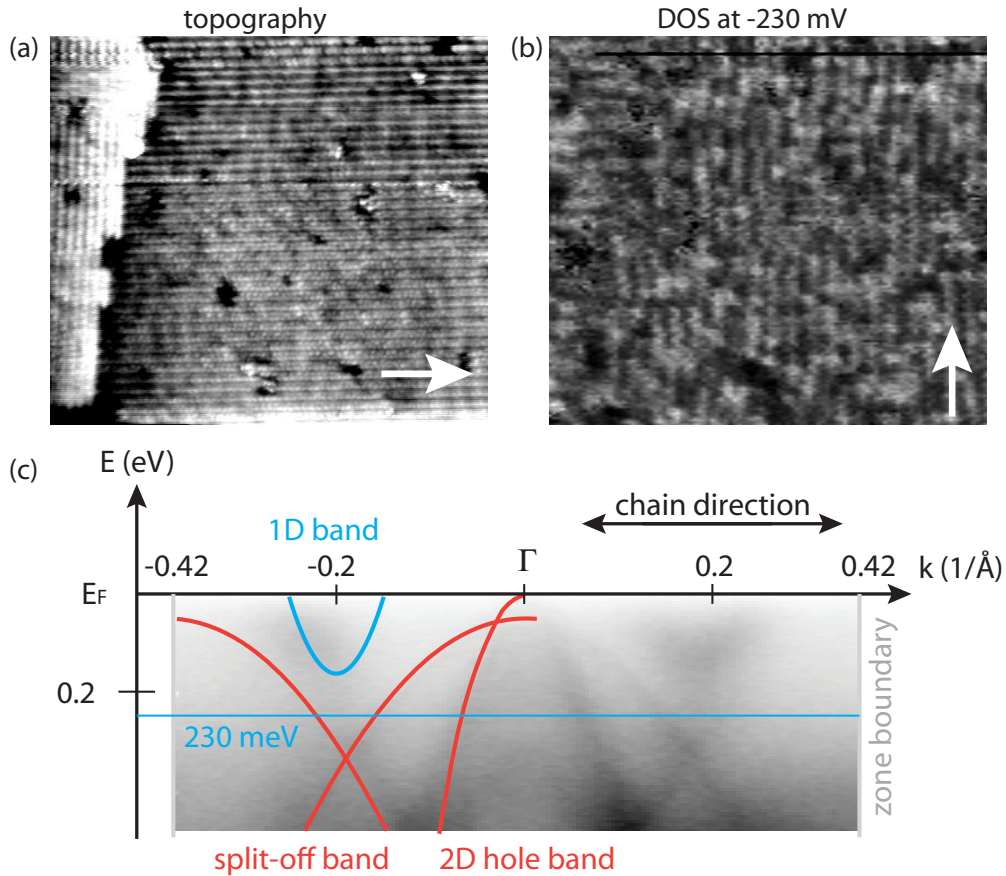


Figure 6.4: (a) STM image ($69 \times 61 \text{ nm}^2$, $U = 0.3 \text{ V}$, $I = 0.6 \text{ nA}$, $T = 4.7 \text{ K}$), showing two terraces. On the lower terrace the wires are oriented horizontally (white arrow). (b) Same area, showing the DOS at -230 mV occupied states. Filaments become visible, that lie vertical (white arrow) that are 32 \AA spaced. (c) Bandmap measured at $h\nu = 35 \text{ eV}$, where an additional split of band is detected. This band and its backfolded counter part show a crossing below the 1D band. STS at -230 meV will only detect these states. Thus the 90° rotated filaments in the DOS maps are attributed to these states. From [A.16]

6.3 Tomonaga-Luttinger liquid behavior

6.3.1 Power-law suppression of the density of states

The low-energy excitations of this highly confined nanowire system have been probed using STS. By recording the differential conductivity as dI/dV one obtains a good measure of the DOS for a small energy window around the chemical potential μ . Variations of the tunneling matrix element may then be neglected, see chapter 3.2.1. Local effects from different orbitals or the influence of buried defects (see previous chapter) are averaged out by integrating over typically 10^3 spectra taken over several unit cells. The tunneling spectrum at 4.7 K is shown in fig. 6.5 (a). In the scrutinized energy window from -50 meV to +50 meV, one finds a pronounced depression of the signal with a minimum at the chemical potential μ . Notably no energy gap is detected, as was reported for the related chain systems [84]. The observed spectral behavior appears to comply with a power-law dependence upon energy. This is the prediction for a TLL, with its $DOS \propto E^\alpha$ (at $T = 0$ K), see chapter 2.2.4. More specifically the DOS was predicted to follow eq. 2.61 for finite temperatures

$$\rho(E, T) \propto T^\alpha \cosh\left(\frac{E}{2k_B T}\right) \left| \Gamma\left(\frac{1+\alpha}{2} + i\frac{E}{2\pi k_B T}\right) \right|^2, \quad (6.1)$$

with k_B as Boltzmann's constant. In using this equation convoluted with the broadening of the Fermi distribution of the tunneling tip and the finite resolution of the STM electronics (5 meV) [25, 27] a perfect fit to the data is achieved with $\alpha = 0.53$, see fig. 6.5 (a).

The DOS at the chemical potential ($E = 0$ eV) at temperatures from 4.7 K to 102 K is shown in fig. 6.5 (b). The data is overlaid with a T^α with $\alpha = 0.53$ curve (grey) and a resolution broadened curve (orange). The resolution broadening is only relevant in the low temperature limit and its contribution towards higher temperatures decreases. Again a very close match with the data is achieved. The identical power-law dependence in both energy and temperature is a key feature of TLL theory. It results from the fact that the electronic low-energy excitation spectrum has no intrinsic energy scale other than the temperature [47, 55]. Note, that the data points on the temperature curve have been measured with different

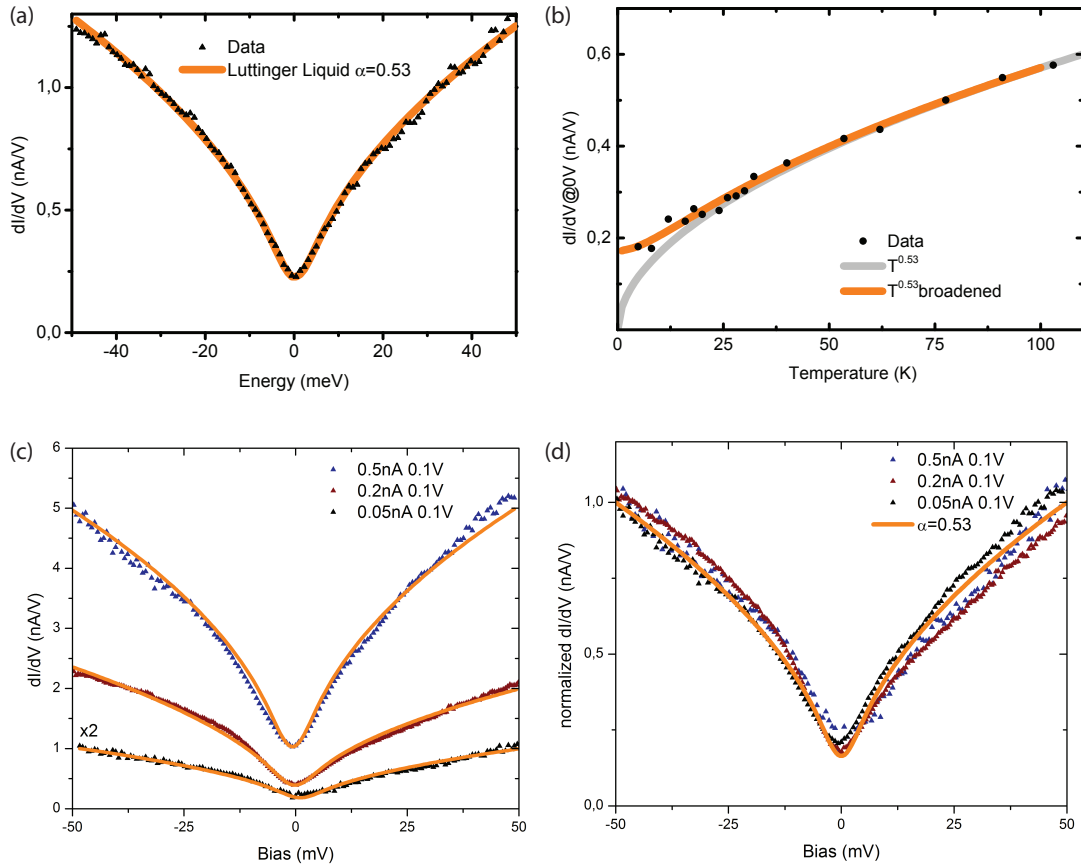


Figure 6.5: (a) Differential conductivity from tunneling spectroscopy. STS data at 4.7 K (averaged over ~ 103 spectra in a $30 \text{ nm} \times 30 \text{ nm}$ area), showing a recess around zero bias. Orange curve, TLL model, a power law with exponent $\alpha = 0.53$ (b) T-dependent DOS at zero bias plotted up to 102 K. The data are described by a power law with the same exponent (grey); the orange curve includes experimental broadening. (c) Spectra taken at different tunneling setpoints, as-measured. All may be fitted with exponents by $\alpha = 0.53 \pm 0.05$. Only the absolute signal varies according to the tunneling setpoint. (d) After scaling all curves coincide. Therefore, different setpoints for the data acquisition do not affect the observed power-law behaviour. From [A.8]

types of tunneling tip materials (Au, W, PtIr). This clearly shows, that there is no influence of the tip on the observed DOS.

Importantly, the observed power-law is independent of the tunneling setpoint, which may be seen in fig. 6.5 (c). A series of spectra have been recorded for several tunneling setpoints. All curves can be fitted with the same power-law exponent $\alpha = 0.53 \pm 0.05$. This becomes even more apparent when scaling the tunneling spectra to unity at -50 meV to account for the different setpoints, see fig. 6.5 (d). All curves coincide, leading to the conclusion, that the tunneling setpoint does not affect the obtained spectra.

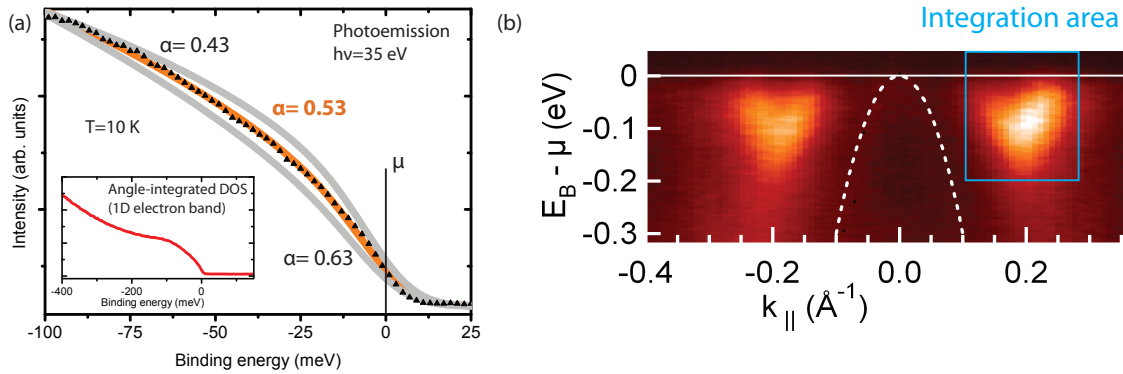


Figure 6.6: (a) Angle-integrated line shape of 1D band from ARPES reveals the same power law depression with the same exponent $\alpha = 0.53$ as in STS. Inset: Wider energy range spectrum. [A.8] (b) Corresponding band map with integration area in blue, from [A.6].

Yet, since STS measurements probe the sample in a tunneling circuit geometry, it is not always clear, if the signal reflects the intrinsic spectral function or extrinsic effects from the circuit. Such extrinsic effects are identified as zero-bias anomalies (ZBA) and will be discussed in detail in chapter 6.6. However several open questions regarding the microscopic conduction path remain due to the lack of theoretical modeling for this tunneling setup:

- How long resides an electron, tunneling from the tip to the sample, in the chains before propagating to the back contact?
- Where does the electron leave the wire? (At terrace steps, through the substrate or at the top contacts)

- What is the tunneling resistance between wire and substrate?

The answers to these questions are highly important, when it comes to analyze the obtained signal from STS. Consequently the contact situations need to be investigated more closely. The obtained results presented in this thesis may serve as input for for future theoretical models.

For now independent information, obtained from the ARPES measurements is available. Here it is widely accepted, that the signal reflects the spectral function of the sample [34, 52, 79, 150] and is not influenced by extrinsic effects. For better comparison with the STS measurements, the ARPES signal is integrated over the right electron pocket, as seen in fig. 6.6 (b). Here one also finds a collapse of the spectral weight, fig. 6.6 (a), which can be fitted independently by a power-law with $\alpha = 0.53 \pm 0.05$. This complies perfectly with the STS results, so that the latter must be interpreted as the intrinsic spectral function of the electron liquid.

6.3.2 Universal scaling

Further support for a TLL interpretation of the tunneling spectra comes from their temperature-dependence. Several spectra between 4.7 and 102 K are plotted in fig. 6.7 (a). From TLL theory it is predicted for the DOS to follow the same power-law over energy and temperature, chapter 2.2.4 [47, 55]. This was already shown in two separate plots in fig. 6.5 (a) and (b). When examining the predicted power-law behavior, eq. 6.1, it should be possible to reduce the data onto a single curve. This scaling behavior can be directly tested for the tunneling spectra. In fig. 6.7 (b) the experimental dI/dV curves of fig. 6.7 (a) are normalized to $T^{0.53}$ and plotted versus $eV/k_B T$. Most notably, all experimental spectra collapse onto a single curve within the error bars $\alpha = 0.53 \pm 0.05$. This is seen in even more detail in the logarithmic data of fig. 6.7 (c) and (d). Here, the low energy part of the spectra suffers from the finite resolution of the STM (5 meV). Yet, towards higher energies all curves coincide on a straight line with a slope of $\alpha = 0.53$. In both cases they strictly follow the theoretical behavior. These observations thus provide proof for the TLL nature of the conduction electron system in these Au atom chains.

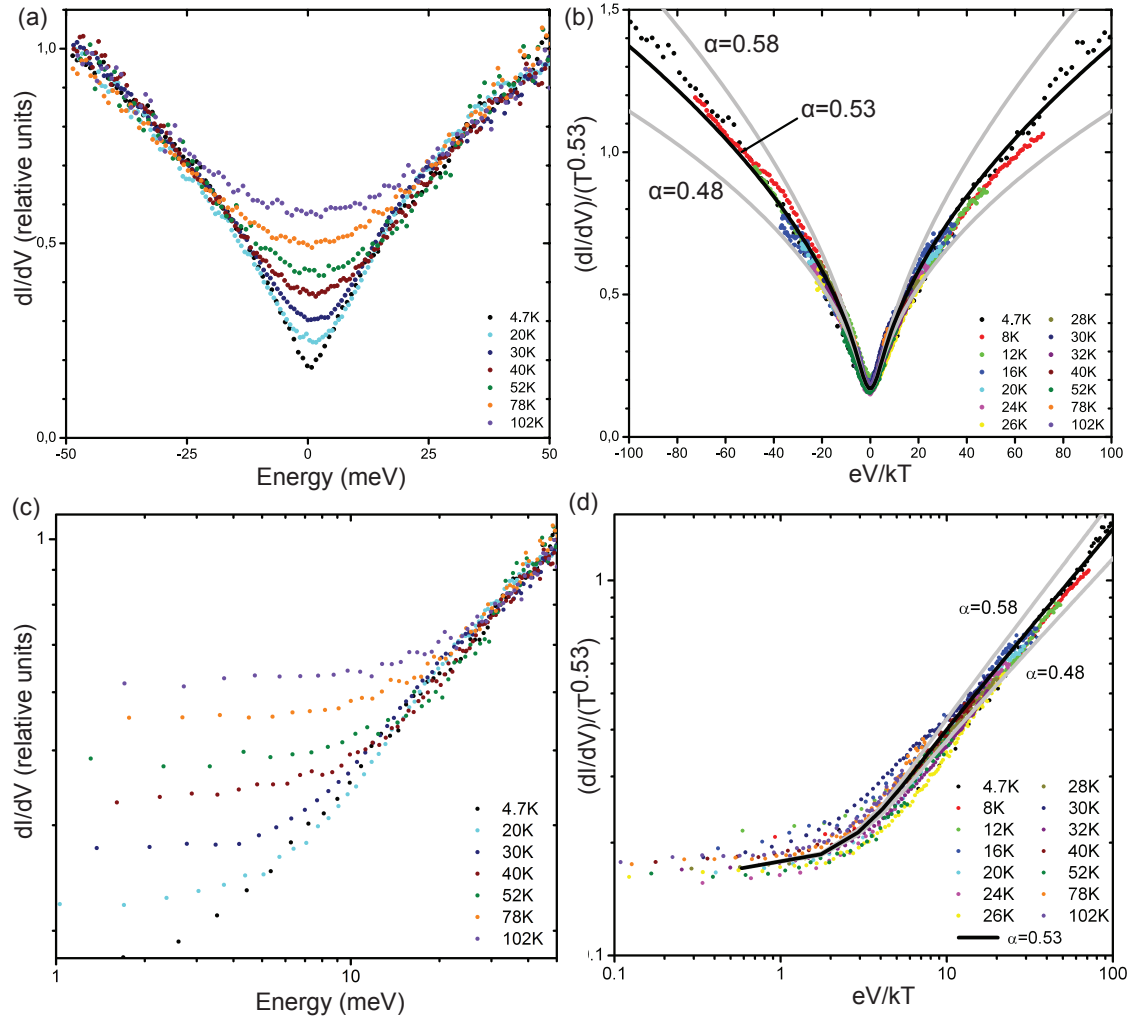


Figure 6.7: (a) Differential conductivity for a series of temperatures as indicated. The DOS at zero bias increases with T . (b) Universal scaling plot of the tunneling data, using the renormalized energy scale eV/kT . All curves coincide, showing universal scaling behavior as predicted by TLL theory. The fit curve accounts for thermal broadening of the TLL, the T dependence of the Fermi distribution for the tip, and is convoluted with the experimental resolution. Black curve: TLL power law with $\alpha = 0.53$. Grey: $\alpha \pm 0.05$ variation. (c) and (d) positive bias side of spectra of (a) and (b) in log-log scale. From [A.8]

The power-law exponent can be fixed with high accuracy to $\alpha = 0.53$. It is directly related to the charge stiffness constant K_ρ , chapter 2.2.4:

$$\alpha_{bulk} = (K_\rho + K_\rho^{-1} - 2)/4, \quad (6.2)$$

assuming repulsive and spin-rotation-invariant interaction, ($K_\sigma=1$) [47, 55]. The parameter K_ρ depends on the interaction strength in the system and lies in the range between 0 and 1, with $K_\rho = 1$ ($\alpha = 0$) for the non-interacting scenario. In the present case one may obtain a value $K_\rho = 0.26$ for the Au/Ge(001) nanowires. This corresponds to the strong interaction regime [55] and compares well to related studies on TLL systems, see chapter 6.5.

Note however, that this consideration is strictly only valid in the TL model, which is based on a single band situation. The electronic band structure of Au/Ge(001) on the other hand comprises two electron pockets on either side of the Γ -point, see fig. 6.1. There are recent theoretical treatments towards a better description of such case of a two band (four branch) system [151]. These will be discussed in detail, when examining chain-end spectra in chapter 2.2.5, where a different edge exponent may be calculated from the new band situation.

6.4 Spin-charge separation

In a TLL the separation of spin and charge degrees of freedom is an important property. This effect may be studied with photoemission or tunneling experiments. After the removal of an electron, spin and charge decouple and propagate with different velocities along the wire, see chapter 2.2.3. In using ARPES, a k-resolved technique, it should be possible to observe two dispersing features. These two apparent dispersion branches, are known as spinon and holon. The latter produces a shadow band at higher binding energies. Yet, in the study on the 1D band only a single dispersing feature is detected, fig. 6.1. Since there is strong evidence for a TLL in the observed tunneling spectra, the question arises why spin-charge separation has not been detected in ARPES?

The individual spectral weight of the spinon and holon branch depends strongly on the charge stiffness parameter K_ρ and therefore on the exponent α [52, 55, 57]. While the two branches have equal spectral weight for a half filled band in the

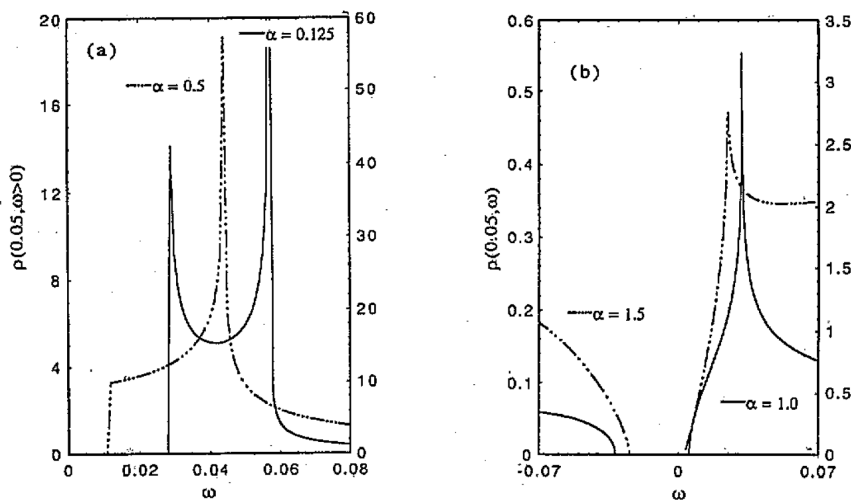


Figure 6.8: Weight of spinon (low energy peak) and holon (high energy peak) in the spectral function plotted over the binding energy ω . Depending on the correlation strength of the system α changes. (a) for weak correlation and (b) For strong correlation. Above $\alpha = 0.5$ the spectral weight of the spinon vanishes. Therefore it will not be detectable in the ARPES measurements of the Au/Ge(001) chains. From [54].

TL model ($\alpha = 1/8$), an increasing value of α leads to a shift of the spectral weight away from the spinon branch. The intensity of the spinon peak decreases out rapidly. Especially, for exponents greater than $\alpha = 1/2$, all weight is removed from the spinon peak, leaving only a faint intensity roll-off at the remaining single holon peak, see fig. 6.8. This means that in the correlation regime this transfer of spectral weight completely suppresses the occurrence of doublet peak. Therefore indications of indicate spin-charge separation are absent in the spectral function.

For the specific case of the present Au chains with $\alpha = 0.53$ this implies that the spinon singularity has vanished, leaving only a single holon peak in the spectrum [54, 55, 57]. Therefore, the observation of only one dispersing branch (holon) in the ARPES spectra may be readily explained within the TL model. Note however, that these considerations have to be refined by theoretical modeling, which does not exists to date, to accommodate the two band case of the Au/Ge(001) bandstructure.

6.5 Related Tomonga-Luttinger liquid systems

Examples for the experimental observations of TLL behavior are very rare. Also none of these systems is surface defined. Some examples with the determined charge

stiffness coefficients and the respective experimental method for analysis are listed below:

- The organic Bechgaard Salts were the first system to show TLL signatures. In TTF-TCNQ some indications from ARPES point towards the observation of spin-charge separation. [24]. The other system is (TMTSF)₂X, which has been scrutinized with optical conductivity measurements. Here is determined to $K_\rho = 0.23$ [152].
- A further class of systems are the chalcogenides, forming layered crystallites. Due to their high aspect ratio they are considered to be electronically 1D. Prominent examples include NbSe₃ [153] and MoSe [154], where TLL scaling behavior could be shown in transport measurements.
- In transport measurements on carbon nanotubes universal scaling behavior could be shown [27] and could later be confirmed by photoemission experiments [28]. $K_\rho = 0.28 - 0.36$
- Recently the study of gated semiconductor channels also found the low energy excitations to be compatible with a TLL scenario. $K_\rho = 0.26 - 0.28$ [30].

The K_ρ determined range from 0.23 to 0.36, which is a rather close range. For the Au/Ge(001) chains a $K_\rho = 0.26$ was found, according to the TL model, fits very well to these previous experimental results.

The surface of purple bronze Li_{0.9}Mo₆O₁₇ has been thoroughly studied by the same techniques as used in this thesis, namely STS and ARPES. Consequently the results on the lithium bronze will be presented here in more detail and a comparison to the Au/Ge(001) chains will be given.

Purple bronze Li_{0.9}Mo₆O₁₇

The purple bronze Li_{0.9}Mo₆O₁₇ is a bulk crystal with a high anisotropic conductivity and thereby may be described as a quasi-1D, regarding the electron system. A very detailed STS study has been performed by Hager *et al.* Their approach was similar to the experiments performed in this thesis. Several thousand spectra have been averaged for a single dataset in order to eliminate the influence of local disturbances

and to gain high statistical confidence. A tunneling spectra at 4.9 K is shown in fig. 6.9 (a). A clear depression towards the Fermi energy is seen. It may be fitted with the same expression as used in eq. 6.1 (including the finite resolution of the STM 5 meV). The fit (red curve) results in a critical exponent $\alpha = 0.60$. Such spectra have been acquired for a temperature range of 4.9 to 55 K. In fig. 6.9 (b) the DOS at the Fermi energy is plotted over temperature. The dotted line follows a power law with $\alpha = 0.46$, which is the best fit to the data. Accounting for the resolution broadening, the solid curve fits the data much better towards lower temperatures. The study could determine the critical exponent to $\alpha = 0.62 \pm 0.17$.

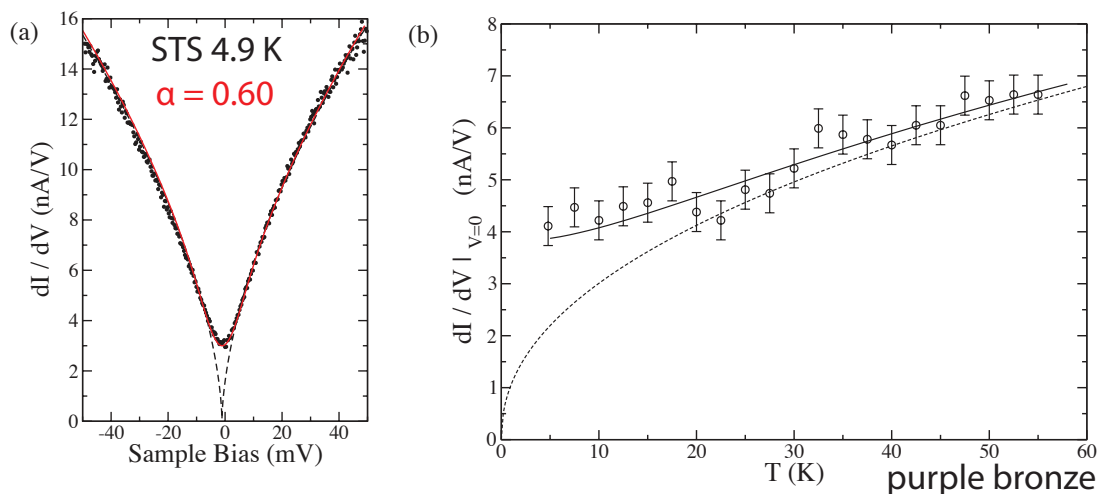


Figure 6.9: (a) High-resolution tunneling spectrum of the purple bronze surface. A clear suppression towards the fermi energy is seen in the scrutinized energy range. The data may be fitted very closely with a power-law with the exponent $\alpha = 0.60$. (b) Temperature dependent study of the DOS at the Fermi energy shows a power law with the same exponent (dotted line). When accounting for resolution broadening (solid line) also a close match can be made over the whole temperature range. From [25].

When comparing the results to the Au/Ge(001) chains one finds a slightly enhanced critical exponent in the purple bronze, yet with a much higher uncertainty. It results in a charge stiffness coefficient of $K_\rho = 0.24$, which is close to the value of $K_\rho = 0.26$ for the Au chains. Note that also ARPES studies have been performed for the purple bronze, in which also no spin-charge separation could be detected. This is consistent with the argumentation of the previous chapter and the effect is confirmed by systematic modeling of the corresponding TLL spectra [155]. It is also important to note, that the critical exponent from ARPES was determined to

$\alpha = 0.9$, which is far away from the STS result [26]. However this discrepancy is presumably due to the band situation. $\text{Li}_{0.9}\text{Mo}_6\text{O}_{17}$ is also a multi-band system, and as stated earlier, the TL model does not account for such scenario. As a result similar observations by means of photoemission and STS have been made. Yet the data on the present Au chains are much more consistent and the critical exponent could be detected with much higher certainty over both energy and temperature.

6.6 Zero-bias anomalies

Beside the TLL behavior there are certain other alternative mechanisms in reduced dimensions and in specific circuiting geometries which can result in a suppression of the DOS at the Fermi energy. So a careful discussion of the tunneling data from the Au/Ge(001) chains has to be made in the light of these ZBA. The main idea behind all of these effects is that the tunneling experiment consists of a current flow from the tip, through the nanowires and eventually into the substrate. The experiment is not a mere probing of the DOS but also influences the properties of the scrutinized system. Since it is unknown how long the tunneled electron resides on the wire before propagating into the substrate, a charging of the wire in terms of a Coulomb blockade or hopping conductance between wire segments have to be kept in mind and considered critically.

Coulomb pseudogap by disorder

An alternative explanation for a suppression of spectral weight in low-dimensional metals would be a Coulomb pseudogap, which occurs in the presence of disorder. The model for this effect consists of metallic 1D wires of randomly distributed size closely neighboring each other, i.e. electron tunneling is possible. The problem is, that the propagation of an injected electron along a single wire is affected by electron-electron scattering due to the strong lateral confinement. Yet, also the exchange of electrons between the disordered wires/channels is possible. In the Au/Ge(001) system this could be due to coupling of the wires mediated by the supporting substrate. By averaging over the complete DOS of such model system one finds that the functional form of this zero-bias anomaly for low energies is described by an *exponential* decrease. An advanced treatment of the tunnel-

ing spectrum based on the Green's function formalism, with explicit inclusion of electron-electron scattering processes is performed in [156, 157]. Note that the exponential decrease is unlike the power-law suppression of the DOS described by the TLL theory.

To test the disorder model a fit of the tunneling data is performed. Using the interaction strength of the electrons Ω as free fit parameter the result is shown in fig. 6.10. While at higher energies a coarse approximation to the data can be achieved, the match is increasingly poor at lower energies around the Fermi energy. Hence, the obtained tunneling spectra may not be explained with a Coulomb pseudogap.

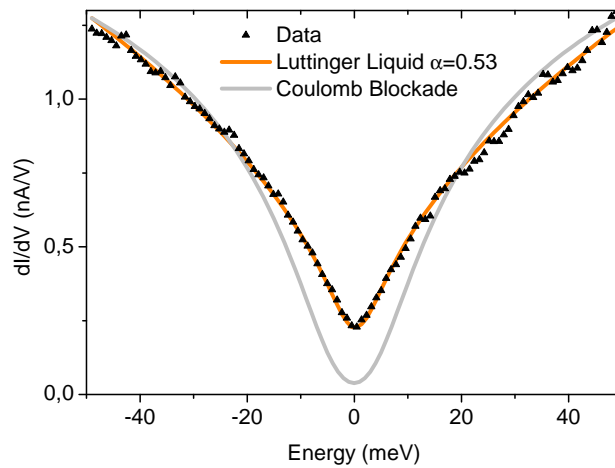


Figure 6.10: Comparison of STS signal at 4.7 K with two fits. The orange curve shows a perfect fit with power-law behavior. Grey is the model for the Coulomb blockade with an interaction strength of $\Omega = 10$ meV, where only a reasonable fit may be achieved at higher energies. Towards the Fermi energy the fit becomes increasingly poor. Thus a Coulomb blockade may be excluded for the observed spectra. From [A.8]

6.6.1 Charging of islands

A different model reported by Giaever and Zeller [158] assumes small metallic Sn clusters incorporated into an insulating matrix, see fig. 6.11. This would be the case if the Au/Ge(001) chains were metallic and placed on an insulating substrate. In order to add or remove an electron to an individual cluster an energy price has to be paid in terms of the Coulomb blockade.

The charging energy of a nanowire may be calculated using the expression from Jackson for the capacity of a cylindrical quantum wire [159]:

$$C = 4\pi\epsilon \frac{l}{2\ln(l/R)} \left(1 + \frac{0.6137056}{2\ln(l/R)} + \frac{1.086766}{(2\ln(l/R))^2} + O\left(\frac{1}{(2\ln(l/R))^3}\right) \right) \quad (6.3)$$

and

$$E = \frac{e}{C}, \quad (6.4)$$

where ϵ is the permittivity of the wire, l the wire length and R its radius. With a dielectric constant of 10 and a wire diameter of 0.5 nm and 100 nm length the resulting charging energy is 15 meV. Consequently one expects to see an energy gap of this size in the tunneling spectrum. By averaging over different cluster sizes (chain lengths) one ultimately arrives at a tunneling spectrum that has a *linear* suppression around zero bias [160]. This contradicts the experimental evidence. Here the data unmistakably shows power-law behavior and, in addition, exhibits universal scaling over energy and temperature. This is the canonical behavior of a TLL.

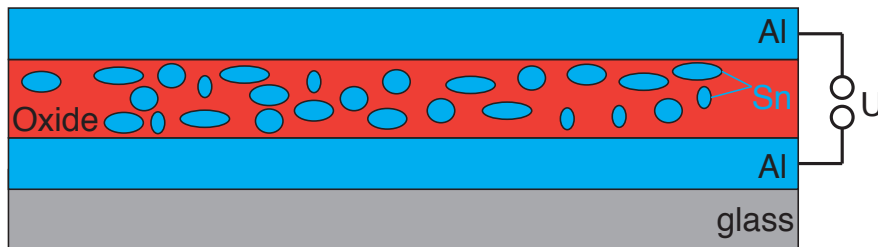


Figure 6.11: Schematic of the experimental setup of Giaever and Zeller for the charging of islands with Sn clusters in an insulating oxide layer. Tunneling occurs between the top and bottom electrode through the islands. After [158].

Also the Au/Ge(001) data do not show a variation of the tunneling spectrum for different wires (i.e., when performing measurements on different locations on the sample). This would be the case when averaging over different chain lengths, resulting in differently sized energy gaps. In conclusion, the objective finding is that the tunneling spectra are not described by such charging scenario.

Furthermore, from subsequent quantum-mechanical treatments it becomes evident that such charging scenario is overly simplistic, and not applicable to the present situation. The island picture of Giaever and Zeller does not include external resistances that have to be accounted for in the tunneling circuit. Alternatively the advanced many-body quantum theory as proposed by M. H. Devoret et al. [161] may be used, which describes the so-called *dynamical Coulomb blockade*.

6.6.2 Dynamical Coulomb blockade

The main idea behind the dynamical Coulomb blockade (DCB) is that a low dimensional system cannot be treated separately, but is always in contact with bulk electrodes for performing the measurement. In the current case the tunneling tip of the STM acting as the top contact and the Ge substrate as the back contact, see schematic fig. 6.12. A theory with inclusion of the electromagnetic environment (the contacts) was first developed by Devoret et al. [161]. The main conclusion was, that a coulomb blockade may only be detected in a high impedance environment. This means that the impedance of the contacts has to be comparable to the resistance quantum

$$R_Q = \frac{h}{2e^2} = 25.8\text{k}\Omega, \quad (6.5)$$

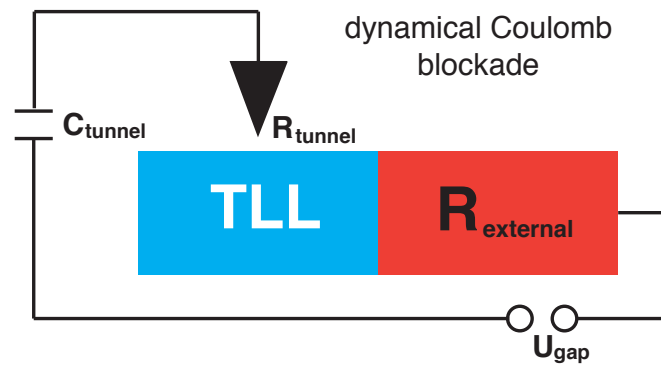


Figure 6.12: Schematic representation of the dynamical Coulomb blockade. The tunneling setup into the TLL is coupled to an external impedance. This might influence the obtained spectra, if the external impedance is of the order of the resistance quantum. Yet this regime has been carefully avoided in the studies on the Au/Ge(001) chains. Note, that the tunneling resistance and capacity have been treated separately in the DCB formalism. After [161].

with Planck's constant h . Otherwise the Coulomb gap will be suppressed, since it would require excitation of quantum-mechanical modes of the electromagnetic environment.

Later it was discovered by Safi and Saleur [162], that this situation may result in a power-law of the tunneling signal over the applied bias. Their model includes an extrinsic impedance in the tunneling circuit. The resulting power-law exponent depends on the ratio of the external impedance and the resistance quantum

$$\alpha_{DCB} = \frac{2R}{R_Q}. \quad (6.6)$$

Yet, there are a number of reasons why such external perturbation can be ruled out for the present tunneling experiment:

- (i) Only a very high external resistance R can result in a conductance which follows the form of a power-law upon energy. As for the leads in the STM setup, very low resistance copper or gold cables are used. The highest resistance contribution in the tunneling experiment will be the semiconducting substrate. However only highly conducting n-doped Ge substrates were used, so that the total resistance of the semiconductor stripe can be determined to about 50Ω . Consequently the impedance of the complete setup will be nearly three orders of magnitude lower than R_Q , thus the DCB requirement is not met.
- (ii) The power-law exponent in the DCB model is dependent on the local resistance as eq. 6.6. Consequently one should observe a trend when tunneling far away from the edge contacts (in the center of the sample) or close to the edge. Such trend is not observed and one only finds one single exponent of $\alpha = 0.53$. Moreover one may estimate the expected exponent in the DCB model by assuming an external impedance of $R \sim 50 \Omega$ as upper boundary, one obtains

$$\alpha_{DCB} = 2R/R_Q = 0.004. \quad (6.7)$$

This is clearly not reconcilable with the observed value of $\alpha = 0.53$. Therefore, a connection of the spectral shape to the environmental resistance can be clearly excluded.

- (iii) Since ARPES measures the identical power-law depression as STS there is independent evidence from a technique, that does not correspond to a circuiting geometry, see figs. 6.5 and 6.6. There the electrons are removed by photoemission and it is widely accepted, that the resulting spectra reflect the intrinsic spectral function of the sample. Importantly the ARPES experiments are performed on grounded samples and in a bias free environment. Since both methods result in the same power-law exponent, one has to conclude, that the tunneling experiments indeed also reflect the intrinsic spectral properties of the Au/Ge(001) nanowires.

6.6.3 Variable range hopping

Lastly, there is a model by Rodin and Fogler, which includes hopping conduction of electrons between chains of variable length [163, 164]. Such scenario would require a coupling of the Au/Ge(001) nanowires through the substrate. This so-called variable range hopping (VRH) may also yield a power-law of the conductance as a function of the applied bias and temperature. However, there are two different exponents for V and T . Notably, the exponents in this model range from 2 to 4 and therefore are not compatible with the determined exponent of the Au/Ge(001) chains of $\alpha = 0.53$. In addition, the model proposes that when both exponents coincide, the Tomonaga-Luttinger liquid case is recovered. This is exactly what is observed for the current experimental data and shown in the scaling plot of fig. 6.7. Consequently a VRH mechanism can therefore be excluded.

6.7 Atomic-scale manipulation

The surface character of the TLL in the Au/Ge(001) nanowire system allows to study local variations of the electronic properties by using STM, see fig 6.13. Interesting scenarios include:

- (i) **Chain Ends:** The original TLL theory was proposed for an infinite chain [23, 55]. In recent years there have been a number of theoretical publications dealing with a finite system and the effects that occur at the end of a 1D chain. Here, these predictions may be tested by examining spectra at the edge of a substrate terrace or close to vacancies.
- (ii) **Doping:** Additional alkaline atoms may act not only as scattering sites on the chains but also locally modify the band filling of the 1D band. A gradual increase of the filling may change the coupling strength of the electrons and thereby change the properties of the TLL state. This is then detectable as a different power-law exponent in the DOS.
- (iii) **Bridging Atoms:** By deposition of excess gold it becomes possible to build bridges between the chains and thereby tune the dimensionality of the electron system. Coverage dependent spectra may give evidence for the stability of the TLL state towards coupling to higher dimensions. Furthermore one may speculate if a charge density wave at low coupling is feasible.

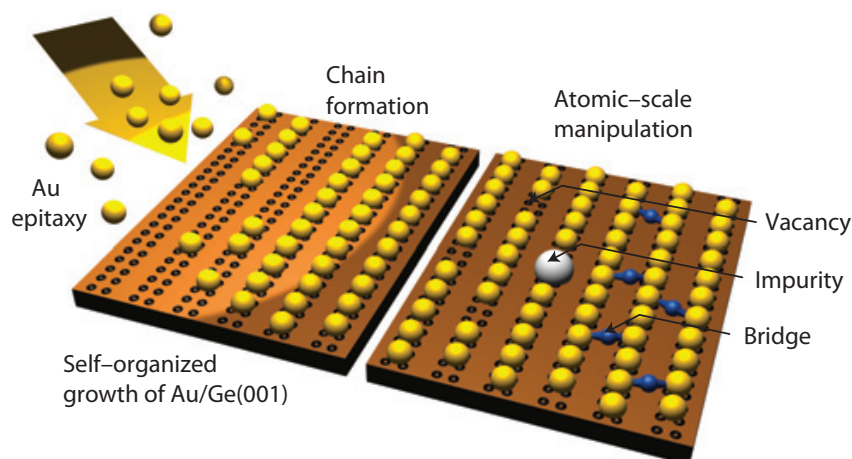


Figure 6.13: Schematic representation of chain formation and possible atomic modifications. For the first time it is possible to study this surface defined TLL system regarding (i) chain-ends at terrace steps or vacancy defects (ii) doping with alkaline atoms and (iii) dimensional crossover by additional bridging atoms between the chains. From [A.8]

6.7.1 Chain ends

Terrace edges on this surface defined system are the ideal locations to test the theory for a bounded TLL. As laid out in chapter 2.2.5 the power law exponent α is predicted to increase towards the chain end [36]:

$$\alpha_{end} = (K_\rho^{-1} - 1)/2, \quad (6.8)$$

for $K_\sigma = 1$, in the TL model. When using the $K_\rho = 0.26$ derived from the bulk, a theoretical $\alpha_{end} = 1.43$ is calculated, notably increased over the chain bulk. The tunneling spectroscopy data close to a terrace edge are shown in fig. 6.14. As seen from the STM topography, the left terrace is terminated towards the center of the image. By averaging the DOS of two chains to improve statistics, the fit with the T-corrected expression yields an exponent of $\alpha = 1.20$, which is significantly enhanced over the bulk value in long chains. Yet, the determined end exponent is still smaller compared to the calculated $\alpha_{end} = 1.43$ predicted by theory. However, this is due to the finite averaging window of the STS measurement. This will lead to an averaging of different DOS curves. As presented in chapter 2.2.5 the end spectrum of a TLL is characterized by a power-law exponent α_{end} , which exists up to a crossover energy ω_C . This state collapses with increasing distance x from the edge as $\omega_C(x) \propto 1/x$. At energies above ω_C , the spectral shape is characterized by α_{bulk} . In the experiment close to the edge this implies that the finite area used to improve statistics will average over slightly different spectral shapes. It yields an *apparent* exponent that is slightly less than the underlying TLL exponent α_{end} .

This effect may be modeled using some simple assumptions on the spectral shape of the DOS in dependence of the distance from the edge. When the TLL spectrum $\rho(\omega, x)$ is plotted over the universal abscissa $\omega \cdot x$, one finds from a graphical estimate (fig. 2.8) that the crossover kink occurs roughly at $\omega_C \cdot x / v_C \approx 0.5$ where v_C is the charge velocity. In order to produce numerical simulations, one may approximate v_C by v_F , which can be derived from ARPES data in [A.6] as $v_F \sim 2 \text{ eV\AA}$. This leads to a crossover energy of

$$\omega_C(x) = \frac{0.5 \cdot v_F}{x}. \quad (6.9)$$

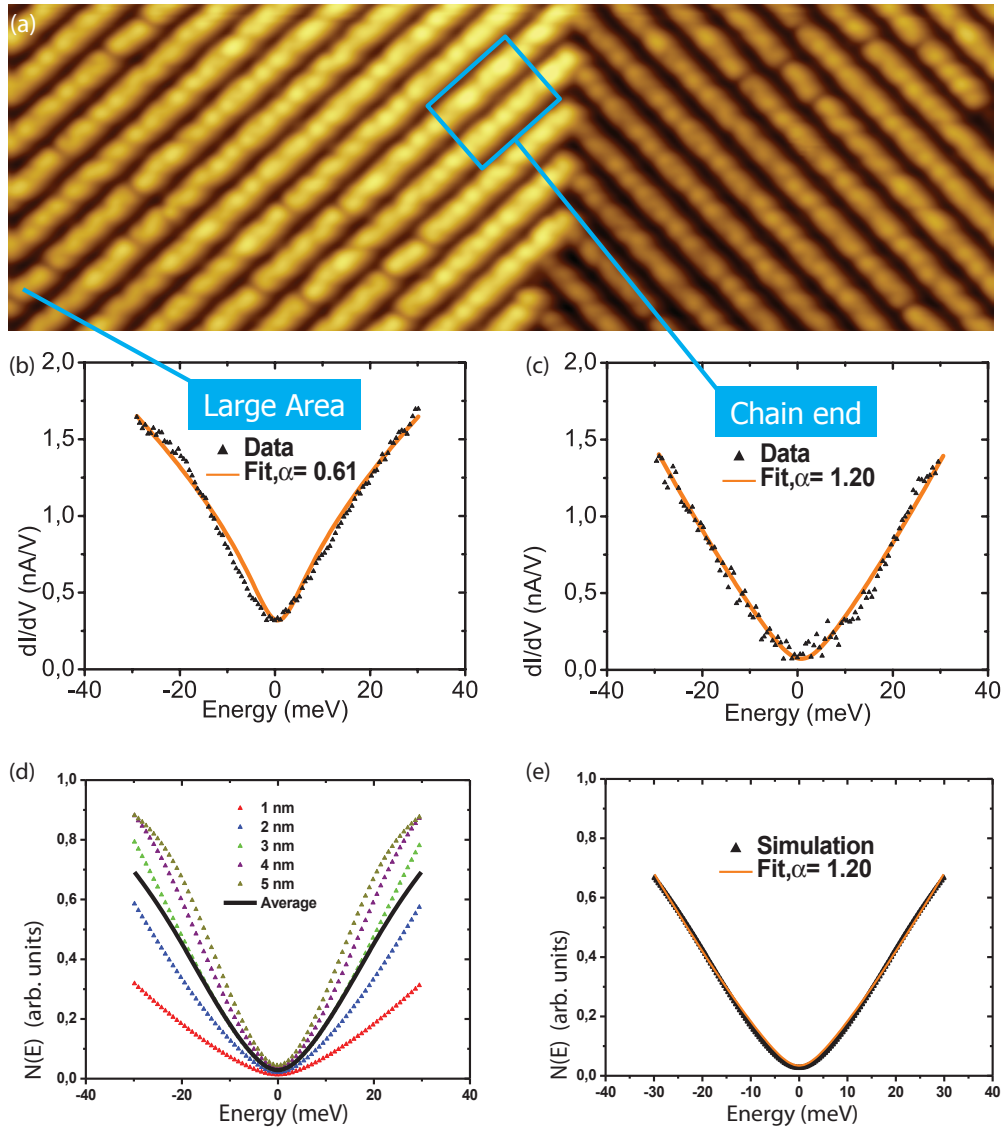


Figure 6.14: (a) STM image of a terrace edge ($U = 1.5$ V, $I = 0.3$ nA $T = 4.7$ K). (b) STS data at 4.7 K. Further away from the edge, the spectrum shows an apparent exponent $\alpha = 0.61$, which is clearly dominated by the bulk value $\alpha_{bulk} = 0.53$ (c) Close to the edge in the indicated area (averaged over two chains for statistics). The exponent is increased to an apparent value of $\alpha = 1.20$, from [A.8] (d) Simulated spectra of a TLL at different locations from chain end, characterized by two exponents $\alpha_{end} = 1.43$ (at low energies) and $\alpha_{bulk} = 0.53$ (at high energies), with a crossover energy that increases towards the end. The experimental length window is simulated by averaging 101 spectra in this range of $x = 1 - 5$ nm with corresponding crossover energies $\omega_C = 100 - 20$ meV. The curves include temperature- and resolution-broadening (4.7 K, 5 meV). (e) The modeled TLL spectrum after spatial averaging can closely be fitted with a single power-law, yielding an apparent exponent $\alpha = 1.20$, as seen in the experiment, that is slightly reduced over the theoretical chain end exponent $\alpha_{end} = 1.43$.

With this expression, it is possible to calculate the crossover energy ω_C for every distance from the chain end. The DOS $N(\omega, x)$ in the crossover region between the two exponents α_{end} and α_{bulk} may thus be smoothly interpolated using a weighting function $f(\omega, \omega_C)$:

$$N(\omega, x) = x^{-\alpha_{bulk}} \left(f(\omega, \omega_C) \frac{\omega^{\alpha_{end}}}{\omega_C^{\alpha_{end}}} + [1 - f(\omega, \omega_C)] \frac{\omega^{\alpha_{end}}}{\omega_C^{\alpha_{bulk}}} \right). \quad (6.10)$$

For the weighting function a simple Fermi distribution function has been chosen:

$$f(\omega, \omega_C(x)) = \left(1 + e^{\frac{\omega - \omega_C}{\Delta\omega/4}} \right)^{-1}. \quad (6.11)$$

Temperature effects are included by replacing the power-laws in eq. 6.10 with the DOS (ω, T) for a single exponent α from eq. 6.1. In addition, finite tip temperature and resolution broadening are included with subsequent convolution.

Regarding the obtained edge exponent of $\alpha = 1.20$, the averaging window may be determined to $x = 1-5$ nm. The corresponding numerical spectra are shown in fig. 6.14 (d) in 1 nm steps. Since r is small, they vary noticeably over this range. In order to perform a more continuous averaging, 101 spectra have been calculated in the range of 1-5 nm. The mean curve is shown in fig. 6.14 (e). In using the temperature corrected fitting function eq. 6.1 [25], the simulated curve is fitted by a single exponent power-law with $\alpha = 1.20$. The agreement with the model, despite its simplicity and numerical approximations, is striking. It follows, that the spatial average of nearby crossover spectra with two exponents α_{end} and α_{bulk} is a valid explanation for the observed apparent exponent.

All considerations above are based on the TL-model with a single metallic band and two crossings at the Fermi energy. However, most recently a refined treatment by the Meden group [151] has been performed for a band structure with four Fermi-crossings. This is the case in the Au/Ge(001) nanowires, see the band schematic in fig. 6.2. Then the calculation for the exponents α and α_{end} changes to [151]

$$\alpha = \frac{1}{8} (K_\rho + K_\rho^{-1} - 2) \quad (6.12)$$

$$\alpha_{end} = \frac{1}{4} (K_\rho^{-1} - 1). \quad (6.13)$$

From the bulk exponent of $\alpha = 0.53$ the end exponent may then be computed to $\alpha_{end} = 1.27$. This is much closer to the experimental observation than the 1.43 predicted by the two-crossing TLL theory. Therefore a four-crossing treatment may be more appropriate for the current system. Both models are capable of explaining the dramatically increased the chain end exponent over the bulk value. As stated in chapter 2.2.5 both theoretical models are based on certain assumptions and the reality in experiment is always more complex. Moreover it has to be highlighted that both models, with two- and four-crossings, predict an edge exponent, that comes close to the measured value observed in the STS experiments.

In going further away from the chain end, the bulk exponent begins to dominate the spectrum, while the end spectrum energy scale almost vanishes. This is seen in fig. 6.14 (b), where the apparent exponent is fitted to $\alpha = 0.61$. It is already close to (but still slightly higher than) $\alpha_{bulk} = 0.53$, which may be explained by the vicinity to the chain end.

6.7.2 Crossover region

The proposed kink in the DOS due to the crossover of different exponents from bulk and edge, see chapter 2.2.5, may be studied in more detail when examining at intermediate distances between edge and bulk. The kink position will lie in the energy region of 1-50 meV. Nonetheless the finite averaging window will broaden the peak. An STS dataset measured at a distance $x = 7-11$ nm from the chain end is shown in fig. 6.15. The logarithmic axes of the plot ensure that the power laws of end and bulk exponent will be easily seen by different slopes. A kink occurs at roughly 10-15 meV and clearly separates the $\alpha_{end} = 1.43$ and $\alpha_{bulk} = 0.53$ regime. The resolution and temperature broadened curves for end and bulk are shown in red and blue. They nicely match the data in the respective regions. In order to model the complete dataset, the same crossover function with a Fermi weighting has been used as in eq. 6.10. In averaging 101 equidistant spectra in the range of $x = 7-11$ nm distance from the edge, an excellent fit to the data may be achieved, see orange curve in fig. 6.15 (b). Again the simple model is capable of describing the crossover region quite well. Importantly, this location-dependent analysis serves as additional proof that one is dealing with a TLL. Hence, the current findings are fully consistent with the expectations from TLL theory, including the strong effect

of the edge exponent. In the future it will be interesting to study the crossover region in more detail and preferably with a smaller averaging window to track the position of $\omega_C(x)$. Also theory predicts small oscillations starting at ω_C towards higher binding energies [36]. So a better energy and spatial resolution might also reveal such proposed fine structure on top of the spectra.

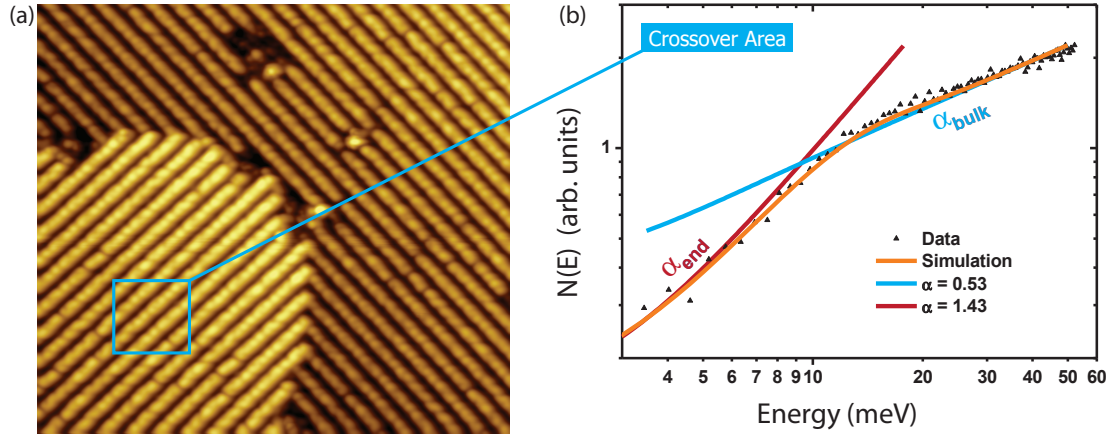


Figure 6.15: Crossover TLL spectra near a chain end from experiment and theory. (a) The experimental spectrum is taken in a window 7-11 nm away from the end. (b) Data is shown as triangles. The overlaid TLL curves (red, blue) use the exponents $\alpha_{end} = 1.43$ at low energies and $\alpha_{bulk} = 0.53$ at high energies, respectively, and are temperature- and resolution-broadened ($T = 4.7$ K, 5 meV). The crossover model applied for $x = 7-11$ nm yields locally varying crossover energies ω_C of 14 to 9 meV. A total of 101 equidistant spectra has been averaged. The resulting simulated spectrum (orange line) describes the data including the kink very closely.

6.7.3 Doping a Tomonga-Luttinger liquid

Since the Au/Ge(001) nanowires are the first surface defined realization of a TLL it becomes very simple to dope the system by evaporation of sub monolayer amounts of alkaline metals. There are three possible effects on the TLL state:

- (i) **Increased band-filling:** In a rigid band model, the filling of the two 1D electron pockets will increase and therefore shift them downwards. As such the Fermi velocity v_F will change and therefore alter the interaction parameter of the TLL.

- (ii) **Additional scattering sites at impurity potentials:** The ions with their positive charge will certainly influence the movement of electrons along the chains.
- (iii) **Enhanced coupling between the chains:** The dopant atoms are randomly distributed on the surface. Some will reside in the groove between the nanowires and therefore potentially lead to an enhanced lateral coupling.

First ARPES studies showed that alkaline atoms in fact act as active dopants. The band filling of the 1D pocket could be increased by a factor of three to about 500 meV. Yet, the background of the spectroscopy signal was dramatically increased for the high doping regime.

Therefore, in the STM investigations very small amounts of dopants have been chosen, in order to study their distribution. A typical surface with a sub monolayer amount of K is shown in the STM topography of fig. 6.16 (a). The nanowires run from the bottom left to the top right and are seen as blue filaments. On top yellow/red protrusions are visible, which are not found on the pristine nanowire reconstruction. As such they may be identified as the additional K atoms. Note that a size distribution exists, ranging from single nanowire width to several nanometer in width. The wider species is attributed to clustering of the alkaline atoms. Interestingly, the single atom dopants preferably occupy sites *on top* of the wires, whereas only a few are situated in the groove. Although the distance between the dopants along the chains is random, there is an increased number of doublets, as indicated by the white ellipse in fig. 6.16 (a). The distance matches the outer charge clouds of the triplet structure in the unoccupied states or the V shape in the occupied states, respectively. In changing the probed bias window from 1.5 V to 0.6 V in the unoccupied states, the dopant atoms are no longer detectable in STM, see fig. 6.16 (b). Note, that both images were taken at the identical sample surface. This implies, that the valence electron of the K atoms is indeed transferred in the surface structure and that only deeper bound states exist in the dopant ions. This finding further corroborates the doping effect seen in ARPES. It also proves that the surface 1D band may indeed be influenced.

Considering the K atoms in the groove, a closeup STM image is shown in fig. 6.16 (a). Two dopants are seen between the chains. Their charge clouds extend

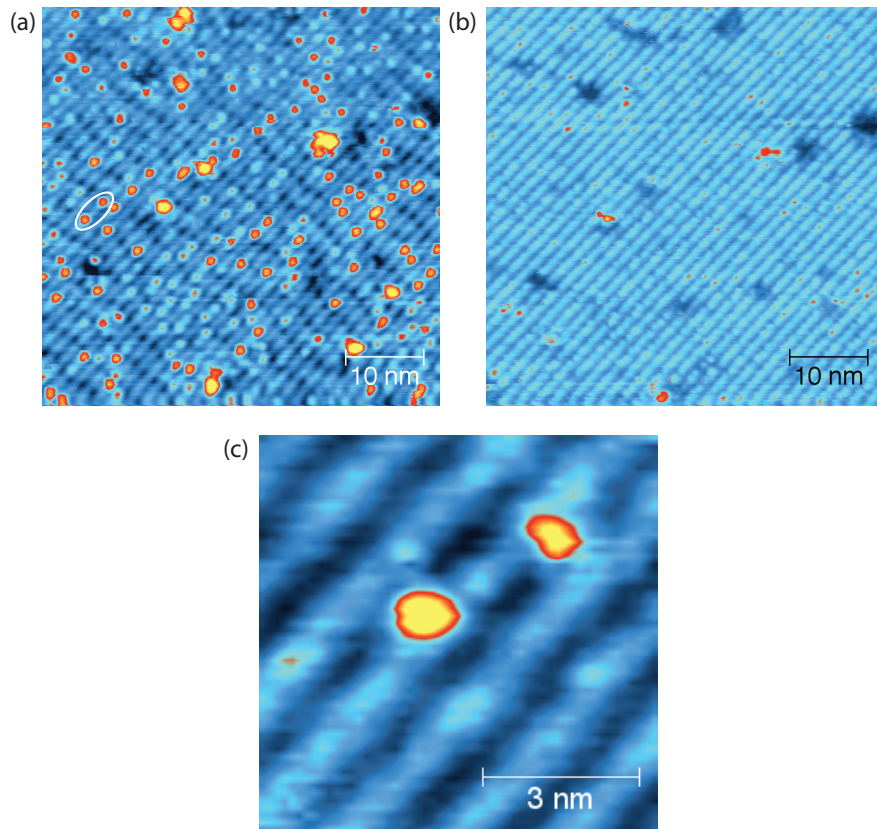


Figure 6.16: (a) STM image of the K dosed surface (+1.5 V 0.1 nA, 300 K). The doing atoms are clearly visible as red/yellow dots on the blue nanowires. Interestingly most of the dopants occupy a position *on top* of the wires, while only a few lie in the groove. (b) Same sample surface probed at a lower binding energy (+ 0.6 V, 0.1 nA, 300 K). The K atoms are not detectable anymore. This points at a successful doping due to electron removal, and only deeper bound electrons exist at the dopants. (c) Closeup of a bridging situation. The K atoms in yellow connect neighboring wires. The charge around the dopants is spread so that a seamless connection is seen in STM

considerably, leading to a seamless connection between two chains. Therefore a possible enhanced coupling between the chains is generated.

In order to test the effect of the dopants on the electronic properties, first spectroscopic data have been collected, see fig. 6.17. The topography shows the chains in blue with K atoms on top. Spectroscopy data on the same sample surface of fig. 6.17 (a) is shown in fig. 6.17 (b). The characteristic depression of the DOS towards the chemical potential is clearly seen. However, a fit with eq. 6.1 results in a dramatically increased power law exponent $\alpha = 0.92$ compared to the undoped case of 0.53. This clearly shows, that the properties of the electron system are altered by the dopants. Yet, it is not known if the change is due to the scattering potential of the ions (chain-ends) or due to enhanced band filling. This situation holds the potential for future studies on coverage dependent spectroscopy measurements. Also in the extremely low coverage regime the DOS around an isolated dopant will be interesting to study. Moreover different species of n-dopants (like K, Na or Cs) may be used in order to test the influence of different ion radii. Also p-doping, which might potentially depopulate the 1D band may lead to interesting effects. Then studies with low electron density might give input for TLL theory, which is strictly only valid in the high density limit.

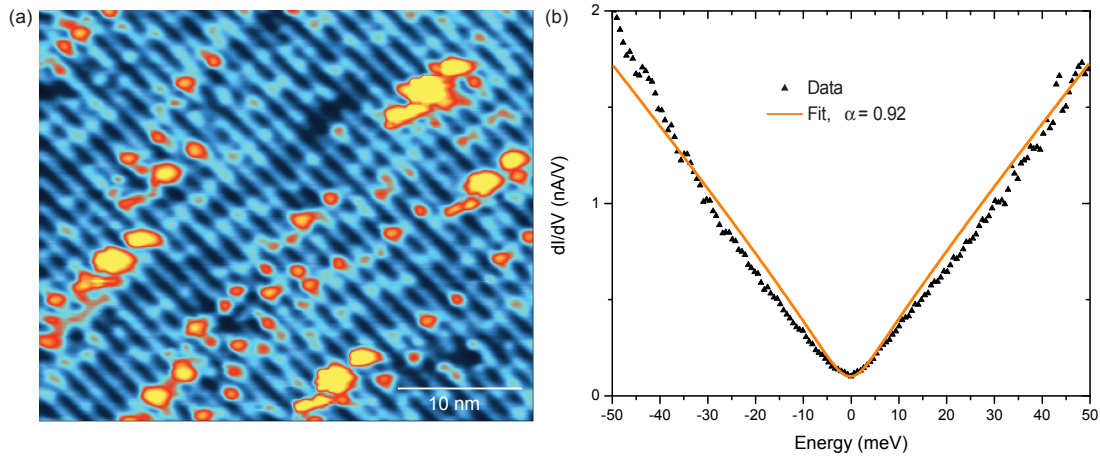


Figure 6.17: (a) STM image (40×35 nm, 1.5 V 0.3 nA, 4.7 K) of a K-doped surface. The dopant atoms are clearly visible on top of the chains and do not seem to modify the wire structure. A size distribution of the dopants suggests slight clustering. (b) STS of the same sample surface as in (a) shows a dramatically increased TLL exponent $\alpha = 0.92$. This may be either induced by dopants acting as additional scattering sites or by the increased band filling.

7 Summary and Outlook

The motivation for the present thesis was to look for candidate surface-defined systems with a high degree of electronic correlation. The focus was on the Au nanowires on the Ge(001) surface, which had been scarcely studied in the past. Therefore an optimized preparation technique was developed in order to ensure a long-range ordered surface. Subsequently the structure of the nanowires was studied using STM and LEED. The electronic properties were scrutinized by ARPES and STS, in order to look for effects of electronic correlations.

A novel cleaning technique was specifically developed for the preparation of the Ge substrate, since the preparation of the Au wires requires excellent substrate cleanliness. The method included a wet chemical etching procedure in a piranha solution to remove the oxide and other contaminants. Dry oxidation in synthesized air lead to a homogeneous and thin protective oxide. Its quality was verified by angle-dependent XPS studies as well as AFM. Flash annealing in-situ was used to remove the protection layer and a low defect long-range ordered substrate surface was prepared. The method yields a much better surface quality over other chemical procedures and it is significantly faster than a sputter and annealing treatment. Thus this recipe ensured optimal conditions for the growth of the nanowires.

Growth parameters for the Au/Ge(001) nanowire reconstruction were investigated over a wide Au coverage and substrate temperature regime. Beside the nanowire reconstruction two additional phases were found. Upon low coverage vacancies in the Ge dimer rows were observed, pointing at diffusion of Au into the topmost surface layers. Towards higher coverages Au clusters form on top of the wires. These exhibit metallic behavior in the tunneling spectroscopy and therefore may act as reference for a good contact situation even at lowest temperatures of 4.7 K.

For the nanowire growth it was found that Au evaporation onto a heated substrate at 500 °C dramatically improves the long-range order of the chains as well

as the coverage and terrace size, compared to cold deposition and subsequent annealing. With this evaporation technique terraces of several hundreds of nanometers in diameter could be produced, which render the ultimate length limit of the nanowires.

Moreover a complete description of the nanowire structure as detected by the two methods STM and LEED was given for the first time. The lateral charge confinement found in STM is of the order of an atomic width and unprecedented for comparable low-dimensional chain systems. No cross bonds between the 16 Å separated chains were found over a wide bias regime. The basic reconstruction of the chains is $c(8 \times 2)$, which was easily seen in STM and LEED. Yet only after refinement of the preparation an additional weak long-range superstructure was detected on top of the basic symmetry. In highly resolved STM topographies at 77 K, this structure was revealed for the first time as triplets in the unoccupied states and a VW-zigzag pattern in the occupied states. A bias series over a wide energy range showed the observed structures to be highly dependent on the energy. This led to the conclusion of a complex electronic contribution from different orbitals to the tunneling signal. The long range order of the supercell could be identified as a $p(4 \times 1)$, which also nicely explains the observed LEED pattern. Also a discussion of the origin of the observed structure was given based on the detached band-structure seen by ARPES measurements.

This superstructure was found not to be due to electronic instabilities like in the Peierls picture, which often occur in chain systems at surfaces, as there was no effect on the electronic properties of the chains. Moreover a reversible second-order phase transition for this superstructure was revealed with a critical temperature of $T_C = 585$ K. In STM the triplets and the VW-zigzag disappeared above the transition and only a chain with a marginal buckling of 8 Å period was visible. This matched the underlying $c(8 \times 2)$ unit cell, and turned out to be unaffected by the transition. The transition was quantitatively scrutinized with LEED spot analysis for a temperature range between 300 and 600 K. The analysis of the critical exponent, determined from the peak height of the diffraction reflexes, pointed towards a 3D Ising type transition. Interestingly the Au/Ge(001) chain system with unprecedented structural anisotropy undergoes a 3D phase transition. This led to the conclusion that substrate is involved in the transition as well. A fact that has

been underestimated in related chain systems at surfaces and has to be considered in the future.

In cooperation with the Bechstedt group from Jena, various structural models were developed on the basis of the observations from STM. A promising candidate turned out to be the AD/HD (Au-dimer/heterodimer) model, which is energetically favorably. It consisted of Au-Au dimers for the troughs and alternating Au-Ge dimers for the wire architecture. Since the model neglected the superstructure, the simulated STM images could be qualitatively compared to the experimental data taken above the transition temperature. The quest for a structural model is thus still ongoing, and will take advantage from the results presented in this thesis.

The electronic properties of the exceptionally structural 1D chains were probed using ARPES and STS. From photoemission a highly 1D surface state was found with no detectable dispersion perpendicular to the chain direction. DOS maps on the nanowires in the energy range of the 1D band showed seamless conducting filaments in chain direction. However, towards higher binding energies the filaments are rotated by 90° and run perpendicular to the chain direction. These were presumably due to the back-bonding of the nanowires to the substrate and therefore decoupled from the 1D electron band.

No gap opening around the Fermi energy was found over a wide temperature regime of 4.7 to 102 K for the measured DOS spectra. Interestingly, a power-law suppression of the DOS towards the Fermi energy with an exponent $\alpha = 0.53$ was found, both over energy and temperature. No effect of the exponent on this tunneling setpoint or the tip material could be found. The power-law behavior was confirmed by analysis of the angle-integrated DOS of the 1D band from ARPES. A temperature dependent STS study revealed universal scaling behaviour over energy and temperature with the same critical exponent, which is a hallmark property of a TLL. A critical discussion of the data with respect to experimental side effects on the TLL was given. Eventually the first realization of a TLL at a surface, based on the broad data basis, could be proven.

Atomic manipulation and local studies of a TLL now become possible. First results could be achieved on the analysis of chain end effects. An increased exponent was determined, which can be readily explained by theoretical predictions for both a one and two band model. Also the predicted crossover region was observed and matched the semi-infinite chain predictions from theory. In addition, first doping

experiments were performed to alter the band filling of the electron system and to add additional scattering sites to the system. Here an increased exponent was found. Future studies may now focus on the atomic playground offered by this system.

- **Chain ends:** Since it is the first TLL system at a surface, specifically chain ends may be studied in more detail. With higher spatial resolution the dependence of the crossover region may be quantitatively analyzed. Furthermore with higher energy resolution it should become possible to detect the predicted oscillations near the crossover region.
- **Dimensional crossover:** Moreover the chains may be modified by doping atoms, which potentially lead to an increased band filling. Also dimensional crossover may be studied by additional bridging atoms or molecules between the wires. This will potentially lead to a modified TLL physics and even a Peierls instability due to the enhanced coupling between the chains.
- **Spin-orbit interaction:** The spin-orbit interaction of Au is clearly non negligible as it has been shown to lead to a spin splitting in the related Au/Ge(111) system. Therefore it will be interesting to see, if this has an influence on the TLL properties, where also no theoretical modeling exists up to now.
- **Input for theory:** Also the presented data may serve as impetus for theory in the growing field of non-linear TLL. Then also higher energy investigations of this system will be a test for the theoretical concepts. A more detailed modeling of a realistic multi-band situation is highly desirable.

To conclude a novel atomic playground for TLL physics has been opened up by the work presented in this thesis. It will serve as a test as well as input for theoretical modeling. This will be highly relevant for understanding the conduction properties of ever shrinking circuits in integrated electronic devices. The single atom conduction path of the Au/Ge(001) chains represents the ultimate lower size limit for any lead. Consequently the presented findings will greatly improve the understanding of real world TLL-systems and will help to advance the field of correlated electrons in low-dimensional systems.

Bibliography

List of own publications

- [A.1] J. Schäfer, C. Blumenstein, S. Meyer, M. Wisniewski and R. Claessen, *New Model System for a One-Dimensional Electron Liquid: Self-Organized Atomic Gold Chains on Ge(001)*, Physical Review Letters **101**, 236802 (2008).
- [A.2] A. Hofmann, X.Y. Cui, J. Schäfer, S. Meyer, P. Höpfner, C. Blumenstein, M. Paul, L. Patthey, E. Rotenberg, J. Bünnemann, F. Gebhard, T. Ohm, W. Weber, and R. Claessen, *Renormalization of bulk magnetic electron states at high binding energies*, Physical Review Letters **102**, 187204 (2009).
- [A.3] J. Schäfer, S. Meyer, C. Blumenstein, K. Roensch, R. Claessen, S. Mietke, M. Klinke, T. Podlich, R. Matzdorf, A. A. Stekolnikov, S. Sauer and F. Bechstedt, *Self-organized atomic nanowires of noble metals on Ge(001): atomic structure and electronic properties*, New Journal Of Physics **11**, 125011 (2009).
- [A.4] J. Schäfer, C. Blumenstein, S. Meyer, M. Wisniewski and R. Claessen, *Comment on "New Model System for a One-Dimensional Electron Liquid: Self-Organized Atomic Gold Chains on Ge(001)" Reply*, Physical Review Letters **103**, 209702 (2009).
- [A.5] S. Sauer, F. Fuchs, F. Bechstedt, C. Blumenstein and J. Schäfer, *First-principles studies of Au-induced nanowires on Ge(001)*, Physical Review B **81**, 075412 (2010).
- [A.6] S. Meyer, J. Schäfer, C. Blumenstein, P. Höpfner, A. Bostwick, J. McChesney, E. Rotenberg and R. Claessen, *Strictly one-dimensional electron system in Au chains on Ge(001) revealed by photoelectron k -space mapping*, Physical Review B **83**, 121411 (2011).

- [A.7] P. Höpfner, J. Schäfer, A. Fleszar, S. Meyer, C. Blumenstein, T. Schramm, M. Heßmann, X. Cui, L. Patthey, W. Hanke, and R. Claessen, *Electronic band structure of the two-dimensional metallic electron system Au/Ge(111)*, Physical Review B **83**, 235435 (2011).
- [A.8] C. Blumenstein, J. Schäfer, S. Mietke, S. Meyer, A. Dollinger, M. Lochner, X. Y. Cui, L. Patthey, R. Matzdorf and R. Claessen, *Atomically controlled quantum chains hosting a Tomonaga-Luttinger liquid*, Nature Physics **7**, 776 (2011).
Tomonaga-Luttinger strikes gold, Nature Physics **7**, front cover (2011).
- [A.9] C. Blumenstein, S. Meyer, A. Ruff, B. Schmid, J. Schäfer and R. Claessen, *High purity chemical etching and thermal passivation process for Ge(001) as nanostructure template*, The Journal of Chemical Physics **135**, 064201 (2011).
- [A.10] C. Blumenstein, J. Schäfer, M. Morresi, S. Mietke, R. Matzdorf and R. Claessen, *Symmetry-Breaking Phase Transition without a Peierls Instability in Conducting Monoatomic Chains*, Physical Review Letters **107**, 165702 (2011).
- [A.11] C. Blumenstein, J. Schäfer, S. Mietke, S. Meyer, A. Dollinger, M. Lochner, X. Y. Cui, L. Patthey, R. Matzdorf and R. Claessen, *Reply to “Debate over dispersion direction in a Tomonaga-Luttinger-liquid system”*, Nature Physics **7**, 776 (2011).
- [A.12] P. Höpfner, J. Schäfer, A. Fleszar, J. H. Dil, B. Slomski, F. Meier, C. Loho, C. Blumenstein, L. Patthey, W. Hanke, and R. Claessen, *Three-dimensional spin rotations at the Fermi surface of a strongly spin-orbit coupled surface system*, Physical Review Letters **108**, 186801 (2012).
- [A.13] S. Meyer, T.E. Umbach, C. Blumenstein, J. Schäfer, R. Claessen, S. Sauer, S.J. Leake, P.R. Willmott, M. Fiedler, and F. Bechstedt, *Structural Examination of Au/Ge(001) by Surface X-Ray Diffraction and Scanning Tunneling Microscopy*, Physical Review B, **85**, 235439 (2012).

- [A.14] G. Li, P. Höpfner, J. Schäfer, C. Blumenstein, S. Meyer, A. Bostwick, E. Rotenberg, R. Claessen and W. Hanke, *Collinear Magnetic Order in an Isotropic Triangular Antiferromagnet: The Sn/Si(111) Surface System* submitted, arXiv:1112.5062v1 (2012).
- [A.15] C. Blumenstein, S. Meyer, S. Mietke, J. Schäfer, A. Bostwick, E. Rothenberg R. Matzdorf, and R. Claessen, *From structural confinement to Tomonaga-Luttinger liquid in Au-induced quantum chains*, submitted (2012).
- [A.16] S. Meyer, C. Blumenstein, L. Dudy, P. Höpfner, T. Umbach, J. Schäfer, R. Claessen, X.Y. Cui, and L. Patthey, *Photon energy and temperature dependent analysis of the Tomonaga-Luttinger system Au/Ge(001) by high-resolution angle-resolved photoemission*, manuscript (2012).
- [A.17] C. Blumenstein, S. Meyer, S. Mietke, J. Schäfer, R. Matzdorf, and R. Claessen, *Growth and Structural Elements of Au/Ge(001) Chains*, manuscript (2012).

General Literature

- [18] E. Plummer, Ismail, R. Matzdorf, A. Melechko and J. Zhang, *The next 25 years of surface physics*, in *Prog Surf Sci*, pages 17–44, (2001).
- [19] M. Imada, A. Fujimori and Y. Tokura, *Metal-insulator transitions*, *Rev Mod Phys* **70**, 1039 (1998).
- [20] T. Zhang, P. Cheng, W.-J. Li, Y.-J. Sun, G. Wang, X.-G. Zhu, K. He, L. Wang, X. Ma, X. Chen, Y. Wang, Y. Liu, H.-Q. Lin, J.-F. Jia and Q.-K. Xue, *Superconductivity in one-atomic-layer metal films grown on Si(111)*, *Nat Phys* **6**, 104 (2010).
- [21] E. Rashba, *Properties of Semiconductors with an Extremum Loop .1. Cyclotron and Combinational Resonance in a Magnetic Field Perpendicular to the Plane of the Loop*, *Sov Phys-Sol State* **2**, 1109 (1960).
- [22] R. Peierls, *Quantum Theory of Solids*, The International Series of Monographs on Physics, Oxford University Press, USA (1996).
- [23] F. Haldane, *Luttinger Liquid Theory of One-Dimensional Quantum Fluids .1. Properties of the Luttinger Model and Their Extension to the General 1d Interacting Spinless Fermi Gas*, *J Phys C Solid State* **14**, 2585 (1981).
- [24] R. Claessen, M. Sing, U. Schwingenschlogl, P. Blaha, M. Dressel and C. Jacobsen, *Spectroscopic signatures of spin-charge separation in the quasi-one-dimensional organic conductor TTF-TCNQ*, *Phys. Rev. Lett.* **88**, 096402 (2002).
- [25] J. Hager, R. Matzdorf, J. He, R. Jin, D. Mandrus, M. Casalilla and E. Plummer, *Non-Fermi-Liquid Behavior in Quasi-One-Dimensional $Li_{0.9}Mo_6O_{17}$* , *Phys. Rev. Lett.* **95**, 186402 (2005).
- [26] F. Wang, J. Alvarez, S. Mo, J. Allen, G. Gweon, J. He, R. Jin, D. Mandrus and H. Hochst, *New Luttinger-liquid physics from photoemission on $Li_{0.9}Mo_6O_{17}$* , *Phys. Rev. Lett.* **96**, 196403 (2006).
- [27] M. Bockrath, D. Cobden, J. Lu, A. Rinzler, R. Smalley, T. Balents and P. McEuen, *Luttinger-liquid behaviour in carbon nanotubes*, *Nature* **397**, 598 (1999).
- [28] H. Ishii, H. Kataura, H. Shiozawa, H. Yoshioka, H. Otsubo, Y. Takayama, T. Miyahara, S. Suzuki, Y. Achiba, M. Nakatake, T. Narimura, M. Higashiguchi, K. Shimada, H. Namatame and M. Taniguchi, *Direct observation of Tomonaga-Luttinger-liquid state in carbon nanotubes at low temperatures*, *Nature* **426**, 540 (2003).

-
- [29] O. Auslaender, H. Steinberg, A. Yacoby, Y. Tserkovnyak, B. Halperin, K. Baldwin, L. Pfeiffer and K. West, *Spin-charge separation and localization in one dimension*, Science **308**, 88 (2005).
- [30] Y. Jompol, C. J. B. Ford, J. P. Griffiths, I. Farrer, G. A. C. Jones, D. Anderson, D. A. Ritchie, T. W. Silk and A. J. Schofield, *Probing Spin-Charge Separation in a Tomonaga-Luttinger Liquid*, Science **325**, 597 (2009).
- [31] H. Yeom, S. Takeda, E. Rotenberg, I. Matsuda, K. Horikoshi, J. Schaefer, C. Lee, S. Kevan, T. Ohta, T. Nagao and S. Hasegawa, *Instability and charge density wave of metallic quantum chains on a silicon surface*, Phys. Rev. Lett. **82**, 4898 (1999).
- [32] P. Segovia, D. Purdie, M. Hengsberger and Y. Baer, *Observation of spin and charge collective modes in one-dimensional metallic chains*, Nature **402**, 504 (1999).
- [33] J. Ahn, P. Kang, K. Ryang and H. Yeom, *Coexistence of two different peierls distortions within an atomic scale wire: Si(553)-Au*, Phys. Rev. Lett. **95**, 196402 (2005).
- [34] K. Schönhammer and V. Meden, *Correlation-Effects in Photoemission From Low-Dimensional Metals*, J Electron Spectrosc **62**, 225 (1993).
- [35] C. Kane and M. Fisher, *Transport in a One-Channel Luttinger Liquid*, Phys. Rev. Lett. **68**, 1220 (1992).
- [36] S. Eggert, H. Johannesson and A. Mattsson, *Boundary effects on spectral properties of interacting electrons in one dimension*, Phys. Rev. Lett. **76**, 1505 (1996).
- [37] J. Wang, M. Li and E. Altman, *Scanning tunneling microscopy study of self-organized Au atomic chain growth on Ge(001)*, Phys. Rev. B **70**, 233312 (2004).
- [38] J. Wang, M. Li and E. Altman, *Scanning tunneling microscopy study of Au growth on Ge(001): Bulk migration, self-organization, and clustering*, Surf Sci **596**, 126 (2005).
- [39] A. L. Mackay, *The Harvest of a quiet eye: a selection of scientific quotations*, Institute of Physics (1977).
- [40] C. Kittel, *Quantum theory of solids*, Wiley (1963).
- [41] G. Grüner, *Density Waves in Solids*, Westview Press (2000).

- [42] N. D. Mermin and H. Wagner, *Absence of Ferromagnetism or Antiferromagnetism in One- or Two-Dimensional Isotropic Heisenberg Models*, Phys. Rev. Lett. **17**, 1133 (1966).
- [43] H. He and D. Zhang, *Charge density wave gap formation of NbSe₃ detected by electron tunneling*, Phys. Rev. Lett. **82**, 811 (1999).
- [44] M. D. Johannes and I. I. Mazin, *Fermi surface nesting and the origin of charge density waves in metals*, Phys. Rev. B **77**, 165135 (2008).
- [45] S. Tomonaga, *Remarks on Blochs Method of Sound Waves Applied to Many-Fermion Problems*, Prog Theor Phys **5**, 544 (1950).
- [46] J. Luttinger, *An Exactly Soluble Model of a Many-Fermion System*, J Math Phys **4**, 1154 (1963).
- [47] T. Giamarchi, *Quantum physics in one dimension*, International series of monographs on physics, Clarendon (2004).
- [48] K. Schönhammer, *Interacting fermions in one dimension: The Tomonaga-Luttinger model*, arXiv:cond-mat/9710330v3 (1997).
- [49] K. Schönhammer, *Luttinger Liquids: The Basic Concepts*, arXiv:cond-mat/0305035v2 (2003).
- [50] J. Solyom, *Fermi Gas-Model of One-Dimensional Conductors*, Adv Phys **28**, 201 (1979).
- [51] R. Kronig, *Zur neutrinotheorie des lichtetes III*, Physica **2**, 968 (1935).
- [52] V. Meden and K. Schönhammer, *Spectral Functions for the Tomonaga-Luttinger Model*, Phys. Rev. B **46**, 15753 (1992).
- [53] K. Schönhammer and V. Meden, *Nonuniversal Spectral Properties of the Luttinger Model*, Phys. Rev. B **48**, 11521 (1993).
- [54] J. Voit, *Charge-Spin Separation and the Spectral Properties of Luttinger Liquids*, Journal of Physics Condensed Matter **5**, 8305 (1993).
- [55] J. Voit, *One-Dimensional Fermi Liquids*, Rep Prog Phys **58**, 977 (1995).
- [56] D. Orgad, *Spectral functions for the Tomonaga-Luttinger and Luther-Emery liquids*, Philos Mag B **81**, 377 (2001).
- [57] J. Voit, *Spectral properties of nearly free and strongly correlated one-dimensional electrons*, J Electron Spectrosc **117**, 469 (2001).

-
- [58] M. Fisher and A. Dorsey, *Dissipative Quantum Tunneling in a Biased Double-Well System at Finite Temperatures*, Phys. Rev. Lett. **54**, 1609 (1985).
- [59] H. Grabert and U. Weiss, *Quantum Tunneling Rates for Asymmetric Double-Well Systems with Ohmic Dissipation*, Phys. Rev. Lett. **54**, 1605 (1985).
- [60] A. Imambekov and L. I. Glazman, *Universal Theory of Nonlinear Luttinger Liquids*, Science **323**, 228 (2009).
- [61] M. Khodas, M. Pustilnik, A. Kamenev and L. I. Glazman, *Fermi-Luttinger liquid: Spectral function of interacting one-dimensional fermions*, Phys. Rev. B **76**, 155402 (2007).
- [62] R. G. Pereira, S. R. White and I. Affleck, *Spectral function of spinless fermions on a one-dimensional lattice*, Phys. Rev. B **79**, 165113 (2009).
- [63] R. G. Pereira and E. Sela, *Spin-charge coupling in quantum wires at zero magnetic field*, arXiv:0911.1391v3 (2009).
- [64] T. L. Schmidt, A. Imambekov and L. I. Glazman, *The fate of 1D spin-charge separation away from Fermi points*, arXiv:0912.0326v2 (2009).
- [65] G. Binnig, H. Rohrer, C. Gerber and E. Weibel, *Tunneling Through a Controllable Vacuum Gap*, Applied Physics Letters **40**, 178 (1982).
- [66] G. Binnig, H. Rohrer, C. Gerber and E. Weibel, *Surface Studies by Scanning Tunneling Microscopy*, Phys. Rev. Lett. **49**, 57 (1982).
- [67] J. Kubby and J. Boland, *Scanning tunneling microscopy of semiconductor surfaces*, Surf Sci Rep **26**, 61 (1996).
- [68] O. Fischer, M. Kugler, I. Maggio-Aprile, C. Berthod and C. Renner, *Scanning tunneling spectroscopy of high-temperature superconductors*, Rev Mod Phys **79**, 353 (2007).
- [69] R. Wiesendanger, *Scanning Probe Microscopy and Spectroscopy: Methods and Applications*, Cambridge University Press (1994).
- [70] J. Tersoff and D. Hamann, *Theory and Application for the Scanning Tunneling Microscope*, Phys. Rev. Lett. **50**, 1998 (1983).
- [71] J. Tersoff and D. Hamann, *Theory of the Scanning Tunneling Microscope*, Phys. Rev. B **31**, 805 (1985).
- [72] J. Bardeen, *Tunnelling From a Many-Particle Point of View*, Phys. Rev. Lett. **6**, 57 (1961).

- [73] R. Hamers, *Atomic-Resolution Surface Spectroscopy with the Scanning Tunneling Microscope*, *Annu Rev Phys Chem* **40**, 531 (1989).
- [74] R. Becker, J. Golovchenko, D. Hamann and B. Swartzentruber, *Real-Space Observation of Surface-States on Si(111)7×7 with the Tunneling Microscope*, *Phys. Rev. Lett.* **55**, 2032 (1985).
- [75] A. Baratoff, G. Binnig, H. Fuchs, F. Salvan and E. Stoll, *Tunneling Microscopy and Spectroscopy of Semiconductor Surfaces and Interfaces*, *Surf Sci* **168**, 734 (1986).
- [76] C. Davisson, *Diffraction of Electrons by a Crystal of Nickel*, *Phys Rev* **30**, 705740 (1927).
- [77] G. Ertl and J. Küppers, *Low energy electrons and surface chemistry*, VCH (1985).
- [78] M. P. Seah and W. A. Dench, *Quantitative electron spectroscopy of surfaces: A standard data base for electron inelastic mean free paths in solids*, *Surf Interface Anal* **1**, 2 (1979).
- [79] S. Hüfner, *Photoelectron Spectroscopy: Principles and Applications*, Springer (2003).
- [80] F. Bechstedt, *Principles of Surface Physics*, Springer (2003).
- [81] F. Jona, J. Strozier and W. Yang, *Low-Energy Electron-Diffraction for Surface-Structure Analysis*, *Rep Prog Phys* **45**, 527 (1982).
- [82] *Omicron NanoTechnology GmbH*.
- [83] P. Willmott and I. Willmott, *An Introduction to Synchrotron Radiation: Techniques and Applications*, John Wiley & Sons (2011).
- [84] P. C. Snijders and H. H. Weitering, *Colloquium: Electronic instabilities in self-assembled atom wires*, *Rev Mod Phys* **82**, 307 (2010).
- [85] J. Ahn, J. Byun, H. Koh, E. Rotenberg, S. Kevan and H. Yeom, *Mechanism of gap opening in a triple-band peierls system: In atomic wires on Si*, *Phys. Rev. Lett.* **93**, 106401 (2004).
- [86] J. Cho, J. Lee and L. Kleinman, *Electronic structure of one-dimensional indium chains on Si(111)*, *Phys. Rev. B* **71**, 081310(R) (2005).
- [87] C. Gonzalez, F. Flores and J. Ortega, *Soft phonon, dynamical fluctuations, and a reversible phase transition: Indium chains on silicon*, *Phys. Rev. Lett.* **96**, 136101 (2006).

-
- [88] A. A. Stekolnikov, K. Seino, F. Bechstedt, S. Wippermann, W. G. Schmidt, A. Calzolari and M. Buongiorno Nardelli, *Hexagon versus trimer formation in in nanowires on Si(111): Energetics and quantum conductance*, Phys. Rev. Lett. **98**, 026105 (2007).
- [89] J. Crain, J. McChesney, F. Zheng, M. Gallagher, P. Snijders, M. Bissen, C. Gundelach, S. Erwin and F. Himpsel, *Chains of gold atoms with tailored electronic states*, Phys. Rev. B **69**, 125401 (2004).
- [90] I. Robinson, P. Bennett and F. Himpsel, *Structure of quantum wires in Au/Si(557)*, Phys. Rev. Lett. **88**, 096104 (2002).
- [91] J. Ahn, H. Yeom, H. Yoon and I. Lyo, *Metal-insulator transition in Au atomic chains on Si with two proximal bands*, Phys. Rev. Lett. **91**, 196403 (2003).
- [92] S. Riikonen and D. Sanchez-Portal, *Interplay between electronic and atomic structures in the Si(557)-Au reconstruction from first principles*, Phys. Rev. B **76**, 035410 (2007).
- [93] D. Sanchez-Portal, S. Riikonen and R. Martin, *Role of spin-orbit splitting and dynamical fluctuations in the Si(557)-Au surface*, Phys. Rev. Lett. **93**, 146803 (2004).
- [94] H. Yeom, J. Ahn, H. Yoon, I. Lyo, H. Jeong and S. Jeong, *Real-space investigation of the metal-insulator transition of Si(557)-Au*, Phys. Rev. B **72**, 035323 (2005).
- [95] T. Okuda, K. Miyamaoto, Y. Takeichi, H. Miyahara, M. Ogawa, A. Harasawa, A. Kimura, I. Matsuda, A. Kakizaki, T. Shishidou and T. Oguchi, *Large out-of-plane spin polarization in a spin-splitting one-dimensional metallic surface state on Si(557)-Au*, Phys. Rev. B **82**, 161410(R) (2010).
- [96] W. Voegeli, T. Takayama, T. Shirasawa, M. Abe, K. Kubo, T. Takahashi, K. Akimoto and H. Sugiyama, *Structure of the quasi-one-dimensional Si(553)-Au surface: Gold dimer row and silicon honeycomb chain*, Phys. Rev. B **82**, 075426 (2010).
- [97] M. Krawiec, *Structural model of the Au-induced Si(553) surface: Double Au rows*, Phys. Rev. B **81**, 115436 (2010).
- [98] J. Crain, A. Kirakosian, K. Altmann, C. Bromberger, S. Erwin, J. McChesney, J. Lin and F. Himpsel, *Fractional band filling in an atomic chain structure*, Phys. Rev. Lett. **90**, 176805 (2003).

- [99] I. Barke, F. Zheng, T. K. Rugheimer and F. J. Himpsel, *Experimental evidence for spin-split bands in a one-dimensional chain structure*, Phys. Rev. Lett. **97**, 226405 (2006).
- [100] S. C. Erwin and F. J. Himpsel, *Intrinsic magnetism at silicon surfaces*, Nat Comms **1**, 1 (2010).
- [101] H. Zandvliet, *The Ge(001) surface*, Phys Rep **388**, 1 (2003).
- [102] J. Griffith and G. Kochanski, *The Atomic-Structure of Vicinal Si(001) and Ge(001)*, Crit Rev Solid State **16**, 255 (1990).
- [103] S. Saito, T. Hosoi, H. Watanabe and T. Ono, *First-principles study to obtain evidence of low interface defect density at Ge/GeO₂ interfaces*, Applied Physics Letters **95**, 011908 (2009).
- [104] M. Houssa, G. Pourtois, M. Caymax, M. Meuris, M. M. Heyns, V. V. Afanas'ev and A. Stesmans, *Ge dangling bonds at the (100)Ge/GeO₂ interface and the viscoelastic properties of GeO₂*, Applied Physics Letters **93**, 161909 (2008).
- [105] A. Delabie, F. Bellenger, M. Houssa, T. Conard, S. Van Elshocht, M. Caymax, M. Heyns and M. Meuris, *Effective electrical passivation of Ge(100) for high-*k* gate dielectric layers using germanium oxide*, Applied Physics Letters **91**, 082904 (2007).
- [106] D. Lide, *CRC Handbook of chemistry and physics: a ready-reference book of chemical and physical data 1999-2000*, CRC Press (1999).
- [107] Y. Kamata, *High-*k*/Ge MOSFETs for future nanoelectronics*, Materials Today **11**, 30 (2008).
- [108] Z. Liu, Y. Sun, F. Machuca, P. Pianetta, W. SPICER and R. Pease, *Preparation of clean GaAs(100) studied by synchrotron radiation photoemission*, J Vac Sci Technol A **21**, 212 (2003).
- [109] T. Deegan and G. Hughes, *An X-ray photoelectron spectroscopy study of the HF etching of native oxides on Ge(111) and Ge(100) surfaces*, Appl Surf Sci **123**, 66 (1998).
- [110] S. Tanuma, C. Powell and D. Penn, *Calculations of Electron Inelastic Mean Free Paths .5. Data for 14 Organic-Compounds Over the 50-2000 Ev Range*, Surf Interface Anal **21**, 165 (1994).

-
- [111] A. Molle, M. N. K. Bhuiyan, G. Tallarida and M. Fanciulli, *In situ chemical and structural investigations of the oxidation of Ge(001) substrates by atomic oxygen*, Applied Physics Letters **89**, 083504 (2006).
- [112] J. Moulder and J. Chastain, *Handbook of X-ray Photoelectron Spectroscopy: A Reference Book of Standard Spectra for Identification and Interpretation of XPS Data*, Physical Electronics (1995).
- [113] L. Chan, E. Altman and Y. Liang, *Development of procedures for obtaining clean, low-defect-density Ge(100) surfaces*, J Vac Sci Technol A **19**, 976 (2001).
- [114] S. Gan, L. Li, T. Nguyen, H. Qi, R. Hicks and M. Yang, *Scanning tunneling microscopy of chemically cleaned germanium (100) surfaces*, Surf Sci **395**, 69 (1998).
- [115] J. Hovis, R. Hamers and C. Greenlief, *Preparation of clean and atomically flat germanium(001) surfaces*, Surf Sci **440**, L815 (1999).
- [116] H. Okumura, T. Akane and S. Matsumoto, *Carbon contamination free Ge(100) surface cleaning for MBE*, Appl Surf Sci **125**, 125 (1998).
- [117] K. Prabhakaran, T. Ogino, R. Hull, J. Bean and L. Peticolas, *An Efficient Method for Cleaning Ge(100) Surface*, Surf Sci **316**, L1031 (1994).
- [118] K. Prabhakaran, *Oxidation of Ge (100) and Ge (111) surfaces: an UPS and XPS study*, Surf Sci **325**, 263271 (1995).
- [119] L. Chan and E. Altman, *Formation of metastable two-dimensional structures during Ag growth on Ge(100)*, Phys. Rev. B **66**, 155339 (2002).
- [120] J. Wang, M. Li and E. I. Altman, *Scanning tunneling microscopy study of Pd growth on Ge(001)*, J Appl Phys **100**, 113501 (2006).
- [121] O. Gurlu, O. Adam, H. Zandvliet and B. Poelsema, *Self-organized, one-dimensional Pt nanowires on Ge(001)*, Applied Physics Letters **83**, 4610 (2003).
- [122] M. Fischer, A. Van Houselt, D. Kockmann, B. Poelsema and H. J. W. Zandvliet, *Formation of atomic Pt chains on Ge(001) studied by scanning tunneling microscopy*, Phys. Rev. B **76**, 245429 (2007).
- [123] J. Schaefer, D. Schrupp, M. Preisinger and R. Claessen, *Conduction states with vanishing dimerization in Pt nanowires on Ge(001) observed with scanning tunneling microscopy*, Phys. Rev. B **74**, 041404 (2006).

- [124] A. A. Stekolnikov, J. Furthmueller and F. Bechstedt, *Pt-induced nanowires on Ge(001): Ab initio study*, Phys. Rev. B **78**, 155434 (2008).
- [125] A. A. Stekolnikov, F. Bechstedt, M. Wisniewski, J. Schaefer and R. Claessen, *Atomic nanowires on the Pt/Ge(001) surface: Buried Pt-Ge versus top Pt-Pt chains*, Phys. Rev. Lett. **100**, 196101 (2008).
- [126] M. C. Gallagher, S. Melnik and D. Mahler, *Temperature- and exposure-dependent study of the Ge(001)c(8 × 2)-Au surface*, Phys. Rev. B **83**, 033302 (2011).
- [127] D. Kockmann, T. F. Mocking, A. Van Houselt, B. Poelsema and H. J. W. Zandvliet, *Structural and Electronic Properties of Au Induced Nanowires on Ge(001)*, J Phys Chem C **113**, 17156 (2009).
- [128] T. B. Massalski and H. Okamoto, *Binary alloy phase diagrams*, ASM International (1990).
- [129] M. Copel, M. Reuter, E. Kaxiras and R. Tromp, *Surfactants in Epitaxial-Growth*, Phys. Rev. Lett. **63**, 632 (1989).
- [130] M. Copel, M. Reuter, M. Vonhoegen and R. Tromp, *Influence of Surfactants in Ge and Si Epitaxy on Si(001)*, Phys. Rev. B **42**, 11682 (1990).
- [131] R. Berndt, J. Gimzewski and R. Schlitter, *Tunneling Characteristics at Atomic Resolution on Close-Packed Metal-Surfaces*, Ultramicroscopy **42**, 528 (1992).
- [132] J. Gimzewski, R. Berndt and R. Schlitter, *Observation of the Temporal Evolution of the (1 × 2) Reconstructed Au(110) Surface Using Scanning Tunneling Microscopy*, J Vac Sci Technol B **9**, 897 (1991).
- [133] N. Nilius, T. Wallis and W. Ho, *Development of one-dimensional band structure in artificial gold chains*, Science **297**, 1853 (2002).
- [134] N. Lang, *Theory of Single-Atom Imaging in the Scanning Tunneling Microscope*, Phys. Rev. Lett. **56**, 1164 (1986).
- [135] M. Kulawik, N. Nilius and H. J. Freund, *Influence of the Metal Substrate on the Adsorption Properties of Thin Oxide Layers: Au Atoms on a Thin Alumina Film on NiAl(110)*, Phys. Rev. Lett. **96**, 036103 (2006).
- [136] A. Van Houselt, M. Fischer, B. Poelsema and H. J. W. Zandvliet, *Giant missing row reconstruction of Au on Ge(001)*, Phys. Rev. B **78**, 233410 (2008).

-
- [137] T. F. Mocking, D. Stam, B. Poelsema and H. J. W. Zandvliet, *Dynamics of Au-induced nanowires on Ge(001)*, Surf Sci **604**, 2021 (2010).
- [138] J. Yeomans, *Statistical mechanics of phase transitions*, Oxford science publications, Clarendon Press (1992).
- [139] F. Nizzoli, K. Rieder and R. Willis, *Dynamical phenomena at surfaces, interfaces, and superlattices: proceedings of an international summer school at the Ettore Majorana Centre, Erice, Italy, July 1-13, 1984*, Springer-Verlag (1985).
- [140] D. Jackson, *Approximate Calculation of Surface Debye Temperatures*, Surf Sci **43**, 431 (1974).
- [141] H. Tajiri, K. Sumitani, S. Nakatani, A. Nojima, T. Takahashi, K. Akimoto, H. Sugiyama, X. Zhang and H. Kawata, *X-ray diffraction study of the Si(111)-3×3-Ag surface structure*, Phys. Rev. B **68**, 035330 (2003).
- [142] Y. Fukaya, A. Kawasuso and A. Ichimiya, *Reflection high-energy positron diffraction study on Si(111)-3×3-Ag surface*, Phys. Rev. B **75**, 115424 (2007).
- [143] J.-H. Han, H. S. Kim, H. N. Hwang, B. Kim, S. Chung, J. W. Chung and C. C. Hwang, *Direct evidence of the step-edge buckling at the Au/Si(557)-1×2 surface*, Phys. Rev. B **80**, 241401 (2009).
- [144] K. Nakatsuji, Y. Takagi, F. Komori, H. Kusunohara and A. Ishii, *Electronic states of the clean Ge(001) surface near Fermi energy*, Phys. Rev. B **72**, 241308 (2005).
- [145] K. Nakatsuji, R. Niikura, Y. Shibata, M. Yamada, T. Iimori and F. Komori, *Anisotropic two-dimensional metallic state of Ge(001)c(8×2)-Au surfaces: An angle-resolved photoelectron spectroscopy*, Phys. Rev. B **80**, 081406 (2009).
- [146] K. Nakatsuji, Y. Motomura, R. Niikura and F. Komori, *Shape of metallic band at single-domain Au-adsorbed Ge(001) surface studied by angle-resolved photoemission spectroscopy*, Phys. Rev. B **84**, 115411 (2011).
- [147] Y. Hasegawa and P. Avouris, *Direct Observation of Standing-Wave Formation at Surface Steps Using Scanning Tunneling Spectroscopy*, Phys. Rev. Lett. **71**, 1071 (1993).
- [148] K. McElroy, R. Simmonds, J. Hoffman, D. Lee, J. Orenstein, H. Eisaki, S. Uchida and J. Davis, *Relating atomic-scale electronic phenomena to wave-like quasiparticle states in superconducting Bi₂Sr₂CaCu₂O_{8+Δ}*, Nature **422**, 592 (2003).

- [149] G. Brown, H. Grube and M. Hawley, *Observation of buried phosphorus dopants near clean Si(100)-(2×1) surfaces with scanning tunneling microscopy*, Phys. Rev. B **70**, 121301(R) (2004).
- [150] A. Damascelli, *Probing the electronic structure of complex systems by ARPES*, Physica Scripta **T109**, 61-74 (2004).
- [151] D. Schuricht, S. Andergassen and V. Meden, *Local spectral properties of Luttinger liquids: scaling versus nonuniversal energy scales*, arXiv:1111.7174v1 (2011).
- [152] A. Schwartz, M. Dressel, G. Gruner, V. Vescoli, L. Degiorgi and T. Giamarchi, *On-chain electrodynamic of metallic (TMTSF)₂X salts: Observation of Tomonaga-Luttinger liquid response*, Phys. Rev. B **58**, 1261 (1998).
- [153] E. Slot, M. Holst, H. van der Zant and S. Zaitsev-Zotov, *One-Dimensional Conduction in Charge-Density-Wave Nanowires*, Phys. Rev. Lett. **93**, 176602 (2004).
- [154] L. Venkataraman, Y. Hong and P. Kim, *Electron Transport in a Multichannel One-Dimensional Conductor: Molybdenum Selenide Nanowires*, Phys. Rev. Lett. **96**, 076601 (2006).
- [155] G. Gweon, J. Allen and J. Denlinger, *Generalized spectral signatures of electron fractionalization in quasi-one- and two-dimensional molybdenum bronzes and superconducting cuprates*, Phys. Rev. B **68**, 195117 (2003).
- [156] E. Mishchenko, A. Andreev and L. Glazman, *Zero-bias anomaly in disordered wires*, Phys. Rev. Lett. **87**, 246801 (2001).
- [157] L. Bartosch and P. Kopietz, *Zero bias anomaly in the density of states of low-dimensional metals*, Eur Phys J B **28**, 29 (2002).
- [158] H. Zeller and I. Giaever, *Tunneling, Zero-Bias Anomalies, and Small Superconductors*, Phys Rev **181**, 789 (1969).
- [159] J. Jackson, *Charge density on thin straight wire, revisited*, Am. J. Phys. **68**, 789 (2000).
- [160] I. Giaever and H. Zeller, *Superconductivity of Small Tin Particles Measured by Tunneling*, Phys. Rev. Lett. **20**, 1504 (1968).
- [161] M. Devoret, D. Esteve, H. Grabert, G. Ingold, H. Pothier and C. Urbina, *Effect of the Electromagnetic Environment on the Coulomb Blockade in Ultrasmall Tunnel-Junctions*, Phys. Rev. Lett. **64**, 1824 (1990).

- [162] I. Safi and H. Saleur, *One-channel conductor in an ohmic environment: Mapping to a Tomonaga-Luttinger liquid and full counting statistics*, Phys. Rev. Lett. **93**, 126602 (2004).
- [163] A. S. Rodin and M. M. Fogler, *Numerical studies of variable-range hopping in one-dimensional systems*, Phys. Rev. B **80**, 155435 (2009).
- [164] A. Rodin and M. Fogler, *Apparent Power-Law Behavior of Conductance in Disordered Quasi-One-Dimensional Systems*, Phys. Rev. Lett. **105**, 106801 (2010).

Acknowledgment

A thesis in the field of physics is never the work of one single individual. Thus I am very grateful for the possibility to work in this vibrant field together with many bright minds.

- First and foremost I would like to thank Prof. Ralph Claessen for the opportunity to perform my work at his great chair, the EP4.
- Special thanks go to my advisor, Jörg Schäfer, for his ongoing interest and eagerness towards new results. He was the driving force with constant motivation and this behavior made me the scientist I am today. Also he and Prof. Claessen made it possible for me to travel around the globe and learn from some of the best scientist in the field of surface science at many synchrotron experiments.
- Prof. René Matzdorf offered me the possibility to perform experiments at his setup and together with his group, where I found a second scientific home.
- I would like to thank Sebastian Meyer for the hilarious times we enjoyed together and frustrating times we stood through.
- Also I am grateful for the collaboration with Sebastian Mietke, who did nearly all measurements on the STM with me and was strongly involved in the interpretation of the data. He also dramatically shortened the late hours in the lab and long weekends.
- To the Häcker-PhDs thanks for the constant support and motivation!
- Christoph Loho and Julian Aulbach for the many hours of proof-reading.
- Thanks also to all members of the EP4 chair for the enjoyable atmosphere.
- Moni, thanks for everything!

Not only was I very lucky with my scientific support, but also with my friends and family, who were always there for me, when I needed them.

- Thanks to my parents (the four of them) for the constant support during my whole education and for teaming up for my defense.

- Special thanks to my brother Tobias for Buffi and other diversions.
- My friends outside the Lab, thank you for reminding me, that there is something else out there.
- And last but not least, my wonderful girlfriend Karin, for the constant support, for understanding late hours and long weekends in the lab, and for making it work. Thank you!

Curriculum vitae

Personal data

Name	Christian Blumenstein
Birthdate and -place	04.01.1983 in Bad Wildungen
Nationality	German

Education

04.2008 until today	PhD studies in physics, Universität Würzburg
03.2008	Diploma in Nanostrukturtechnik
08.2005 until 06.2006	Visiting scholar, University of California, Berkeley, USA
04.2003 until 03.2008	Diploma studies in Nanostrukturtechnik, Universität Würzburg
1999 until 2002	Abitur, Herderschule Kassel
1993 until 1999	Mittlere Reife, Söhreschule Lohfelden
1989 until 1993	Grundschule, Wellerode

Work experience

05.2005 until 04.2011	Founder and CEO of BBK Lifestyle GbR
02.2005 until 04.2005	Internship at OSRAM Opto Semiconductors, Regensburg
07.2003 until 09.2003	Internship at Orthopädische Klinik, Kassel
08.2002 until 04.2003	Community Service at Orthopädische Klinik, Kassel

Erklärung

Hiermit erkläre ich an Eides statt, dass ich die Dissertation eigenhändig, d.h. insbesondere selbstständig und ohne Hilfe einer kommerziellen Promotionsberatung angefertigt und keine anderen als die angegebenen Quellen und Hilfsmittel benutzt habe.

Würzburg den 13.9.2012

Christian Blumenstein

Hiermit erkläre ich an Eides statt, dass ich die Gelegenheit zum Promotionsvorhaben nicht kommerziell vermittelt bekommen habe und insbesondere nicht eine Person oder Organisation eingeschaltet habe, die gegen Entgelt Betreuer bzw. Betreuerinnen für die Anfertigung von Dissertationen sucht.

Würzburg den 13.9.2012

Christian Blumenstein

Hiermit erkläre ich, dass ich die Regeln der Universität Würzburg über gute wissenschaftliche Praxis eingehalten habe.

Würzburg den 13.9.2012

Christian Blumenstein

Hiermit erkläre ich, dass die vorliegende Dissertation nicht in gleicher oder anderer Form bereits in einem anderen Prüfungsfach vorgelegt wurde.

Würzburg den 13.9.2012

Christian Blumenstein